Nonlinear Behavior of Unstable Black Holes in Anti-de Sitter Spacetimes

by

Pablo Bosch Gómez

A thesis
presented to the University of Waterloo
in fulfillment of the
thesis requirement for the degree of
Doctor of Philosophy
in
Physics

Waterloo, Ontario, Canada, 2020

Examining Committee Membership

The following served on the Examining Committee for this thesis. The decision of the Examining Committee is by majority vote.

External Examiner:	Dr. Emanuele Berti Professor Johns Hopkins University
Supervisors:	Dr. Luis Lehner Faculty Perimeter Institute for Theoretical Physics
	Dr. Brian McNamara Professor University of Waterloo
Internal Member:	Dr. Niayesh Afshordi Associate Professor University of Waterloo
Internal-External Member:	Dr. Eduardo Martin-Martinez Associate Professor University of Waterloo
Other Member(s):	Dr. Huan Yang Assistant Professor University of Guelph

Author's Declaration

The thesis consists of material all of which I authored or co-authored: see *Statement of Contributions* included in the thesis. This is a true copy of the thesis, including any required final revisions, as accepted by my examiners.

I understand that my thesis may be made electronically available to the public.

Statement of Contributions

The chapters of this thesis contain material produced in different collaborations.

Chap. 2 of this thesis consists of material from the papers [1, 2], co-authored with Stephen R. Green, Hugo Roussille, and Luis Lehner.

Chap. 3 of this thesis consists of material from the paper [1], co-authored with Stephen R. Green, and Luis Lehner.

Chap. 4 of this thesis consist of material from the paper [2], co-authored with Stephen R. Green, Hugo Roussille, and Luis Lehner.

Chap. 5 of this thesis consist of material from the paper [3], co-authored with Alex Buchel, and Luis Lehner.

In paper [1], I developed the apparent horizon and event horizon finder modules for the nonlinear code, performed extensive tests to confirm the validity of the implementation, and analyzed the output of the nonlinear simulations in the time and frequency domain. All authors discussed the work extensively and edited the draft.

In paper [2], I provided *special initial data* for the excited black hole evolution, performed extensive consistency checks between the linear and nonlinear calculations, tracked the migration of modes in the linear regime with particular set of parameters, and analyzed the output of the nonlinear simulations in the time and frequency domain. All authors discussed the work extensively and edited the draft.

In paper [3], I developed an event horizon finder, performed extensive tests to confirm the validity of the nonlinear implementation as well as the event horizon finder, and analyzed the output of the nonlinear simulations. All authors discussed the work extensively and edited the draft.

Abstract

The nonlinear dynamics of black holes is an increasingly relevant topic of which little is known. In this thesis, we study the full nonlinear dynamics of black holes, as well as their linear behavior, and combine them to find a comprehensive picture of the processes involved. In particular, we study the dynamics of unstable black holes in asymptotically anti-de Sitter spacetimes. We study their general behavior and approach to the final equilibrium state. In the first part of this work, we present linear studies of charged scalar field perturbations of Reissner-Nordström anti-de Sitter (RN-AdS) black holes in the small and large black hole regimes. We present their quasinormal mode spectra, identify the known mode families—superradiant modes, zero-damped modes, AdS modes, and the near-horizon mode— and track their migration under variation of the black hole and field parameters. We present results of the full nonlinear studies of perturbed small and large RN-AdS, showing the nonlinear development of the unstable superradiant modes. For generic initial conditions, charge and mass are transferred from the black hole to the scalar field, until an equilibrium solution with a scalar condensate is reached. Additionally, we use the results from the linear analysis to construct special initial data corresponding to an unstable overtone mode. We find that these special data evolve to produce a new equilibrium state, an *excited hairy black hole* with the scalar condensate in an overtone configuration. This state is, however, unstable, and the system eventually decays to the generic end state. This demonstrates the potential relevance of overtone modes as transients in black hole dynamics. In the second part of this work, we present linear and nonlinear studies of a planar Schwarzschild-AdS black hole and two massive scalar fields. Above the critical energy density the system reaches an equilibrium state where one of the scalars forms a condensate and the other vanishes. Below the critical energy density, however, the system displays an instability at the linear regime. We present results of the full nonlinear development of this instability where a suitable equilibrium condensate does not exist. Indeed, we present compelling evidence that during the dynamics arbitrarily large curvatures are uncovered in the vicinity of the horizon, which turn such region singular in finite time with respect to the boundary observer.

Acknowledgements

I am grateful to my advisor, Luis Lehner, for his patient guidance and invaluable advice. Throughout the years, not only he shared his knowledge and passion with me, but he also supported me in my personal endeavours. I am truly thankful for his mentorship, friendship, and welcoming us into his family.

I would like to thank the members of the examination committee Emanuele Berti, Niayesh Afshordi, Eduardo Martin-Martinez, Huan Yang, Brian McNamara and Luis Lehner for their remarks, questions, and sparking an interesting discussion. It made for a very pleasant experience.

I would like to thank members of my PhD committee: Asimina Arvanitaki, Alex Buchel, Avery Broderick, and Brian McNamara for their support throughout the PhD. I learn a great deal from you, and I quite grateful for it.

I am very lucky to have amazing collaborators: Stephen Green, Alex Buchel, Will East, Laura Sberna, Hugo Roussille. Working side by side with them has not only been a pleasure, but also the source of new knowledge.

I wish to thank the Strong Gravity Comunity at PI for amazing discussions, and sharing their scientific passion with me. The weekly meetings and coffee chats taught me a great deal about strong gravity and astrophysics alike. It has always been a welcoming group.

I am forever in debt with Stephen Green for his support in all fronts. He has been a source of knowledge and encouragement, but above all a great friend.

My time at Perimeter Institute was filled with the joy and support of my friends and colleagues. I am particularly grateful to Rodrigo Gutierrez, Didier Zuñiga, Naty Altamirano, Gabriel Magill, Néstor Ortiz, Clément Delcamp, Lauren Greenspan, Peter Lunts, Andrés Schlief, Damián Galante, Seth Asante, Lucía Córdova, Julian y Carito, Stephen Green, Laura Sberna, Will and Annie East, Alice Bernamonti, Federico Galli, Aldo Riello, Sylvain and Tamara Carrozza, Antonia and Martin Ganahl, Juan Carrasquilla, Béatrice Bonga, Anna Heffernan, Max Corman, Tim Whittaker, Nils Siemonsen, and Daniel Siegel.

My life at Perimeter would not have been the same without the Monday hockeys, the amazing Black Hole Bistro staff, the great coffee chats with Dan, Carleigh, Hayley, Krista, and Jamie. A special thanks to Debbie Gunther that helped me in many administrative tasks throughout the years.

I am very lucky to have a kind and supportive family, who have passed on their entusiasm for research. They have always encouraged me in whatever I decide to do, and have always had my back even when things get rough. Muchas gracias por su apoyo Alfonso, Sofía, Carlos y Claudia.

Finally, I want to express my gratitude to Nayeli for her unconditional support and encouragement. Without her none of this would have developed the way it did. I am forever grateful to be by her side growing a little tomato. Te quiero mucho amourcito.

Financial support

This research has been supported by a CONACyT scholarship for international graduate studies.

To my wife, Nayeli,

and my parents, Carlos y Claudia.

Table of Contents

List of Tables

List of Figures

Chapter 1

Introduction

1.1 General Motivation

This thesis is devoted to the study of black hole dynamics. We do so by examining the interaction of scalar fields and black holes in asymptotically anti-de Sitter (AdS) space-times. In particular, we study the interaction of a charged (complex) scalar field and an electrically charged Reissner-Nordström black hole in asymptotically AdS, as well as the dynamics of two scalar fields in the presence of a planar Schwarschild-AdS black holes. We use linear analysis tools to establish mode stability, or lack thereof, followed by a full nonlinear development of the dynamics. Not only we present a detailed analysis of the dynamics, but we also elucidate the end state of the superradiant and the near-horizon instabilities, within the context of the aforementioned models.

A strong motivation to understand the nonlinear dynamics of black holes comes since the '90s, where developments in gravitational waves pointed out their potential to shed light on dark matter models. In particular, LIGO/Virgo observations could reveal or constrain the nature of the dark matter candidates. Similarly, after the proposal of the gauge/gravity duality, the nonlinear dynamics of black holes became relevant to understand their dual strongly coupled field theories. In particular, the duality was used to construct simple superconductor models, where the nonlinear dynamics are highly relevant.

Dark Matter

The theory of General Relativity (GR) describes how matter interacts gravitationally. In addition to providing a new perspective to the origin and evolution of the Universe, it also

predicted the existence of astrophysical black holes, as well as the existence of gravitational waves.

On the other hand, the interactions at very small scales are accurately described by the Standard Model of particle physics. It provides an incredibly precise understanding of the fundamental building blocks of matter, however, the description of gravity at these very small scales is still missing.

It has become increasingly clear that our Universe is incompatible with either GR on the large scales, or the Standard Model. The analysis of the rotation curves of galaxies showed some "anomalies" that could only be explained by either assuming a large amount of unseen dark matter or by assuming a deviation from the known laws of gravitation at large scales [7, 8, 9]. Similarly, the study of supernovae observations have provided an insight into how the universe is expanding [10]. Confirmation of these observations provides robust evidence that the baryonic matter is not the main contributor to the composition of the Universe, at $\sim 5\%$. The remaining 95% is not well understood, and is composed of a dark matter contribution, $\sim 27\%$ of the Universe, while dark energy makes up for $\sim 68\%$ of the Universe [11, 12]. Dark matter is necessary to explain the apparent existence of more matter than what is actually observed [8, 9], while the cosmological acceleration relies on dark energy as its key ingredient [10]. Both of them still remain a mystery given that dark matter has never been detected experimentally on Earth, and the magnitude of the cosmological constant necessary to explain dark energy is 120 orders of magnitude smaller than what predicted with quantum field theory [13].

A general aspect, of some proposals, to solve the dark matter problem or the accelerated expansion of the Universe, is the prediction of new fundamental degrees of freedom. Fundamental bosonic fields, in particular, are a quite generic and well-motivated feature of extension to the Standard Model, and to modified theories of gravity.

In contrast to the elementary bosons, which are either massless or massive ~ 100 GeV, (pseudo)Goldstone bosons of spontaneously broken global symmetry give rise to small but non-vanishing particle masses. In fact, a well-motivated candidate for such a particle is the QCD axion, a pseudoscalar particle coupled to the QCD instanton number and invariant under the Peccei-Quinn symmetry. An axion potential, which gives rise to a solution for the strong CP problem, is generated when the symmetry is explicitly broken by the QCD instanton effects. As a result the axion acquires a mass of $\sim 10^{-10}$eV. Not only this ultra light boson can solve the strong CP problem, but it is also an interesting candidate for cold dark matter [14, 15, 16].

The Compton wavelength of the QCD axion can be, thus, comparable to the size of

stellar mass black holes (in geometric units) [1]. A large numbers of axions with masses lower than $\sim 10^{-10}$eV, however, might arise from "generic" string compactifications. This motivates the search for, not only the QCD axion, but ultra light bosons in the mass range $\sim 10^{-22} - 10^{-10}$eV, which can interact with stellar or galactic astrophysical black holes through superradiance.

A bosonic field can extract energy from a rotating black hole through superradiant scattering [17, 18], resulting in the increase of the field's amplitude. If, in addition, the field is reflected by a potential barrier sufficiently far away, then this amplification process repeats itself, resulting in an effective exponential growth. This is know as the superradiant instability. In fact, the presence of a massive boson can give rise to a potential barrier. The boson field, then, can tap into the rotational energy of the black hole, leading to an axioninic Bose-Einstein condensate cloud rotating around the black hole.

It is, then, of wide interest to have a more complete picture of the dynamics and the end point of the superradiant instability. It may even lead to observable gravitational wave emission associated to axion transitions between different levels, and with axion annihilations to gravitons [19, 20]. In astrophysics, this instability can be used to constrain the mass of the ultra light bosons[2] and, thus, dark matter models. Testing physics beyond the Standard Model and GR is starting to become a possibility given the increasing number of observations in high-energy astrophysics, and gravitational-wave astronomy.

Global anti-de Sitter (AdS) spacetime has a timelike boundary at infinity that can play the role of the potential barrier for asymptotically AdS black holes. Rotating black holes in asymptotically AdS are subject to the superradiant instability [21, 22, 23]. A similar process occurs for (charged) Reissner-Nordström (RN) black holes [21, 24, 25, 26], with the charge playing the role of the angular momentum.

When perturbations are small a linearized analysis is suitable. Several studies have determined the quasinormal mode spectra of Kerr-AdS [22, 27] and RN-AdS [4, 28]. As the perturbation grows, however, the backreaction onto the spacetime becomes significant, and the linearized description breaks down.

[1] In geometric units, $G = c = 1$, the wavelength of the bosonic field λ_a and the mass of the black hole M should satisfy $M/\lambda_a \sim 1$.

[2] Astrophysical constraints can be set on axion-like (pseudo)scalar particles, as well as more general massive vector boson fields like a massive dark photon.

Holographic Superconductors

The gauge/gravity duality, which also goes by the name of anti-de Sitter (AdS)/ conformal field theory (CFT) conjecture, has provided additional motivation for studying black holes in asymptotically AdS spacetimes. In the AdS/CFT correspondence, a large static black holes correspond to thermal states in the CFT. The timescale to reach a thermal equilibrium in a strongly coupled CFT will be given, then, by the decay timescale of a black hole perturbation described by the imaginary part of its quasinormal frequency. Black hole equilibration is, thus, believed to be holographically dual to thermalization of strongly coupled field theories, whereas instabilities seem to describe phase transitions [29].

In particular, within the AdS/CFT context, *holographic superconductors* have been constructed. The minimal ingredients for this model are a plane symmetric black hole in AdS, a Maxwell field and a charged scalar field. The black hole provides the notion of temperature in the CFT through its Hawking temperature. The charged scalar fields, in the black hole AdS spacetime, describes the condensate in the superconductor. A non-trivial condensate corresponds, then, to a non-trivial configuration of the field outside the black hole. This is usually called black hole "hair" or "scalar hair". Above a critical temperature the system is stable and develops no hair. Below a critical temperature, however, this system gives rise to an instability which forms scalar hair, and, thus, holographically indicates a phase transition. This model, then, has captured the basic elements to describe a superconductor in which a condensate forms at low temperatures, but not at high temperatures [30].

At lower temperatures, *i.e.* as the black hole approaches extremality, the planar RN-AdS black hole is subject to the near-horizon scalar condensation instability [30], which lead to a hairy black hole under dynamical evolution [31]. The nature of the instability is, in fact, related to the Breitenlöner-Friedman (BF) bound, which depends on the dimension and the radius of curvature of the AdS spacetime. The spacetime is stable provided the squared mass of the scalar field satisfies the bound. Remarkably, AdS spacetimes can support scalar fields with negative squared mass as long as they are above the BF bound provided by that spacetime. Extremal planar RN-AdS black holes have a near-horizon geometry which is $AdS_2 \times \mathbb{R}^2$. This in turn provides a near-horizon BF bound, which is less restrictive than the global bound. If the negative squared mass of a scalar field does not satisfy the near-horizon BF bound, then, an instability arises. We refer to this instability as the near-horizon instability. This type of instability can be thought of as the trivial value for the scalar field being unstable and the field rolls off the potential, thus, forming a condensate. The instability halts when the amplitude of the scalar field is significant enough to backreact onto the geometry, hence, modifying the geometry. Indeed

the near-horizon geometry will no longer be $AdS_2 \times \mathbb{R}^2$, rendering the near-horizon BF bound irrelevant, and the stability of the spacetime will be provided by the global BF bound.

Our comprehensive study of charged scalar perturbations of charge black holes in AdS reveal the presence of the superradiant instability and the near-horizon instability in the case the horizon topology is a sphere. We provide nonlinear studies of these instabilities elucidating their end state, which plays a role in determining the final thermal state. Additionally, we study the behavior of a class of exotic black holes which are dynamically unstable due to the near horizon instability.

Classical General Relativity

Questions of black hole instabilities are of theoretical interest in classical General Relativity. Astrophysical black holes form by gravitational collapse, which is a time-dependent process. We expect the final isolated black hole, however, to settle down into a time-independent equilibrium state. It is desirable to classify all of these equilibrium configurations, *i.e.* finding all possible stationary black holes solutions of the vacuum Einstein or Einstein-Maxwell equations. Through a series of uniqueness theorems due Hawking, Carter and Robinson in the '70s [32, 33, 34], it was established that all isolated black holes in Einstein-Maxwell theory are described by the Kerr-Newman family. Black holes in this theory are, then, very simple objects, defined by at most three parameters: the mass, the electric charge and the angular momentum. It is generally accepted that astrophysical black holes are neutral to a very good approximation, due to electron-positron pair production [35] and charge neutralization by astrophysical plasma. The geometry of astrophysical black holes in GR is, therefore, simply described by the two-parameter Kerr metric [36].

An observation of a black hole with a metric that deviates from the Kerr family would point in the direction of a departure from standard physics, either in the gravitational or the matter sector. More recently, developments in cosmology and string theory have encouraged the studies of uniqueness theorem or "no-hair" theorems in higher dimensional black hole spacetimes and black holes in the presence of many new matter field combinations.

In this work we provide examples of entropically favoured hairy black holes in AdS. We construct these black holes through dynamical evolution, which are the end state of the charged superradiant instability. We also show the nonlinear development of a planar Schwarzschild-AdS with two interacting scalar fields, with particular boundary conditions at the AdS boundary, that give rise to the near-horizon instability. In this case, it gives rise to a runaway instability, and leads to a violation of the spirit of the weak cosmic censorship

conjecture. Indeed, arbitrarily high curvature close to the event horizon seem to no longer be hidden from an observer at infinity.

1.2 Summary and Organization of the thesis

In this work we present the full nonlinear behavior of different types of instabilities of black holes in asymptotically anti-de Sitter spacetimes. We will first focus on a charged black hole in asymptotic anti-de Sitter spacetime perturbed by a charged scalar field. Linear studies [4] have identified that the system is unstable under charged scalar field perturbations by means of the superradiant instability. The final fate of the system under this instability, however, has not been elucidated. We present a comprehensive analysis following the dynamics from the linear regime of the instability, at early times, through to the nonlinear regime, where we identify some complex dynamics that take place at intermediate times, and up until the spacetime reaches a stationary state at late times. In fact, with this dynamical study we elucidate the end state of the instability and show its connection to the linear instability. As the linear perturbation grows it interacts nonlinearly with the black hole extracting charge and mass. Eventually, due to the energy extraction, the instability stops and settles into a stationary state. We show that the end state of the superradiant instability is a stationary configuration of a charged black hole with a non-trivial profile of the charged scalar field. The amount of charge in the black hole and in the scalar field change parametrically with the gauge coupling. Indeed, we find solutions were the scalar field has extracted nearly all of the charge from the black hole, resulting in a Schwarzschild-AdS black hole surrounded by a distant low-mass, high-charge scalar field condensate.

Large charged black holes in asymptotically AdS have enjoyed less attention. In fact, less is know about the effect of the superradiant instability or lacktherof. A near-horizon instability, however, has been identified in the linear regime for planar and spherical horizons alike [30, 37]. We perform linear stability and nonlinear dynamical studies of the large charged black hole in asymptotic AdS under a charged scalar perturbation. Through the linear analysis we produce a comprehensive mode picture and use it as a stepping stone for the nonlinear analysis. We identify the known near-horizon instability for near-extremal black holes, as well as modes which are unstable under the superradiant instability. Although the two instabilities are different in nature, we show they coexist in a region of the parameter space for large black holes. We elucidate the fully nonlinear dynamics of both instabilities and show their hairy black hole end states. As a final demonstration, we construct initial data consisting of several superradiant modes, such that the solution

cascades through a series of unstable excited black hole equilibria.

Lastly, we study the nonlinear development of a planar Schwarzschild black hole in asymptotically AdS with two massive scalar fields with a non-trivial coupling, and particular boundary conditions. The system is largely motivated by holographic models such as the ones presented in [38, 39], and shares some properties with the holographic superconductors of [40, 29]. A planar RN-AdS black hole can grow a non-trivial neutral scalar profile due to the near-horizon instability. The instability is directly linked to the Breitenlohner-Friedman bound of the near-horizon region. The scalar field condensate, then, is localized close to the horizon. We introduce an extra scalar field coupled to the original field that condensates, and study how the near-horizon instability is triggered dynamically for this new field. We elucidate the final fate of this dynamical instability with fully nonlinear dynamical evolution. Our nonlinear analysis points in the direction that the end state of this dynamical instability is a singular solution reached in finite time, which would violate the spirit of the weak cosmic censorship conjecture. Observers far away can be reached by signals emanating from spacetime regions with an arbitrarily high curvature. We show how the Kretschmann at the apparent horizon and the event horizon blow up in finite asymptotic time.

In Chap. 2 we introduce the model used in Chaps. 3 and 4 as well as the equations of motion of the system. Additionally, we present the approach taken for the linear analysis, and for the generation of special initial data consisting of several modes which are relevant for Chap. 4. In Chap. 2 we present the basic coordinate choices made, as well as the main characteristics of our implementation.

Chap. 3 we study the nonlinear scattering of a charged scalar field off a small charged black hole in AdS. In particular, we elucidate the end state of the superradiant instability, and explore how it changes parametrically with the charge of the field. We compare our results in the linear regime with perturbative results to validate our code.

Chap. 4 is devoted to the linear and nonlinear analysis of a large charged black hole in AdS. We present a comprehensive picture of the mode spectrum for small and large black holes, alike, and provide evidence for two instabilities in the large black hole regime. Then, we follow the nonlinear development of the near-horizon and the superradiant instabilities. We compare the end state of the superradiant instability in the large and small black hole regimes. Furthermore, we construct special initial data containing specific superradiant modes and show that the solution cascades through a series of unstable excited hairy black hole equilibria.

In Chap. 5 a system largely motivated by *holographic superconductors* is studied. In particular, we study a planar Schwarschild-AdS black hole with two massive scalar fields,

one with negative squared mass and the other with positive squared mass, with a non-trivial interaction between them. We show the linear stability of the planar Schwarzschild-AdS black hole with a tachyon condensation. Furthermore, we present evidence that above the critical energy density, in the linear regime, the non-tachyonic scalar field decays exponentially without oscillations. On the other hand, below the critical energy density it displays a non-oscillatory exponential growth. We explore the fully non-linear development of both cases. We present compelling evidence that in the unstable case the non-tachyonic field grows without bounds, leading to a divergent behavior of the Kretschmann scalar and the area of the event horizon.

As final remark, we make use of Geometric units throughout the thesis, *i.e.* $G = c = 1$, we work in $d = 4$ dimensions, the metric signature is $(-, +, +, +)$, and Latin indices range from 0 to 3.

Chapter 2

Preliminaries

The most general vacuum black hole solution to Einstein equations, in four-dimensional asymptotically flat spacetimes, is the (uncharged) Kerr metric with mass M and spin $J = aM$. The study of a minimally coupled scalar field perturbation in the Kerr background was studied in [41], where they reported the separability of the equation. Teukolsky showed that the perturbation equation decoupled and separate for all Petrov type-D spacetime, if one works directly with the curvature invariants [42]. Physically Petrov type-D spacetimes are associated with the gravitational field of massive object, which is completely characterized by its mass and an angular momentum. This approach is based on the Newman-Penrose formalism, in which one introduces a tetrad of null vectors $\mathbf{l}$, $\mathbf{n}$, $\mathbf{m}$, and $\mathbf{m}^*$, at each point in the spacetime. All tensors are, then, projected onto this null tetrad. Together with the Einstein equations, it gives rise to the Newman-Penrose equations, which link the tetrad vectors, the spin coefficients, the Ricci tensor, the scalar curvature and the Weyl tensor [43]. The most relevant perturbation variables are the Weyl scalars $\mathbf{\Psi}_0$ and $\mathbf{\Psi}_4$, which both vanish in the background spacetime. They are obtained by contracting the Weyl tensor $C_{\mu\nu\lambda\sigma}$ with the tetrad vectors[1]. Roughly speaking, these quantities describe the ingoing and outgoing gravitational radiation. Analogous quantities for the electromagnetic perturbations can, similarly, be constructed by contraction of the Faraday tensor with a combination of the null tetrad. Then, the spin-s field is Fourier-transformed and expanded into spin-weighted spheroidal harmonics

$$\Psi_s(t, r, \theta, \phi) = \frac{1}{2\pi} \int e^{-i\omega t} \sum_{l=|s|}^{\infty} \sum_{m=-l}^{l} e^{im\phi}{}_s S_{lm}(\theta) R_{lm}(r) d\omega \,, \tag{2.1}$$

[1] $\Psi_0 = -C_{\mu\nu\lambda\sigma} l^\mu m^\nu l^\lambda m^\sigma$ describes the ingoing gravitational waves, whereas $\Psi_4 = -C_{\mu\nu\lambda\sigma} n^\mu m^{*\nu} n^\lambda m^{*\sigma}$ describes the outgoing radiation.

where Ψ_s is the so-called master variable. The field's spin weight is equal to $s = \{\, 0, \pm 1/2, \pm 1, \pm 2\}$ for scalar, Dirac, electromagnetic and gravitational perturbations, respectively. In doing so, Teukolsky finds separated ODEs for the angular and the radial part

$$\left(\partial_u(1-u^2)\partial_u\right) {}_sS_{lm} + \left(a^2\omega^2u^2 - 2a\omega su + s + {}_sA_{lm} - \frac{(m+su)^2}{1-u^2}\right) {}_sS_{lm} = 0 \tag{2.2}$$

$$\Delta\partial_r^2 R_{lm} + (s+1)(2r-2M)\partial_r R_{lm} + V(r)R_{lm} = 0\,. \tag{2.3}$$

Where $u \equiv \cos\theta$, $\Delta = (r-r_+)(r-r_-)$ with $r_\pm$ the Cauchy and the event horizon, and with a potential

$$\begin{aligned} V(r) = {} & 2is\omega r - a^2\omega^2 - {}_sA_{lm} \\ & + \frac{1}{\Delta}\left((r^2+a^2)^2\omega^2 - 4Mam\omega r + a^2m^2 + is(am(2r-2M) - 2M\omega(r^2-a^2))\right). \end{aligned} \tag{2.4}$$

The solution to the angular equation is known as spin-weighted spheroidal harmonics, and it reduces to spin-weighted spherical harmonics when the spin of the black hole vanishes. The separation constant ${}_sA_{lm}$ in the general cases is a non-trivial problem. Finally, upon the appropriate transformation of variables the radial equation can be reduced to a one-dimensional Schrödinger equation with an effective potential. In a nutshell, these equations describe the perturbations of black holes due to linearized field of spin s.

With boundary conditions such that at the event horizon only ingoing waves are present and at infinity only outgoing waves are allowed, then, the solution to these equations are quasinormal modes (QNM). They have a definite complex frequency $\omega = \omega_R + i\omega_I$ that is the *quasinormal frequency*, and physically represent the relaxation of the black hole upon the perturbation. There is a discrete set of possible value for ω in the complex plane. The real part of the frequency ω_R corresponds to the oscillation frequency, and the imaginary part of the frequency ω_I, if negative, governs the decay rate over time. If, in fact, the ω_I is negative, then, the black hole relaxation will vanish in time as a superposition of damped oscillations. These quasinormal frequencies can be used to identify black holes, given that they depend on the black hole parameters such as the mass, charge and the angular momentum.

With this in mind we will rederive the radial equation for a charge scalar perturbation on a Reissner-Nordström-AdS background, and use it to find the quasinormal frequencies. Indeed, by studying the QNM spectra we can determine whether an instability is present, as well as understanding the mode structure of the spacetime. Finding a quasinormal

frequency with a positive imaginary frequency would lead to an exponential growth, at least in the linear regime. We would then have to analyze the full nonlinear behavior in order to understand the full extent of such instability. Moreover, spacetimes can have several families of quasinormal modes associated with different features of the geometry. In the quasinormal mode spectrum there may be modes associated to the near-horizon geometry or to the asymptotics of the spacetime, for instance. Successfully identifying these families of modes will allow us to understand the types of instabilities at play.

In what follows, we show the explicit radial equation we solve and provide details of our implementation of Leaver's method [44, 45] to the charged scalar perturbation of RN-AdS. In Uchikata *et al.* [4], the onset of the superradiant instability was established for small black holes in the linear regime. We introduce they key concepts for our numerical implementation of the full nonlinear equation to evolve the superradiant instability well into the nonlinear regime and elucidate its final state. This results will be presented in Chap. 3 and 4.

2.1 Linearized Analysis of RN-AdS spacetime

2.1.1 Model

We will consider Einstein gravity with a negative cosmological constant, coupled to Maxwell and massive charged scalar field, we follow the conventions of [30]. The Lagrangian density is, thus,

$$16\pi G_{\rm N}\mathcal{L} = R + \frac{6}{L^2} - \frac{1}{4}F_{ab}F^{ab} - \left(|D_a\psi|^2 - m^2|\psi|^2\right), \tag{2.5}$$

where $D_a \equiv \nabla_a - iqA_a$ is the gauge covariant derivative, and q is the gauge coupling. We work in $d = 4$ dimensions and $G_{\rm N}$ is Newton's constant. The first two terms are the Einstein-Hilbert Lagrangian plus a negative cosmological constant, thus, the simplest solution to the equations of motion is anti-de Sitter spacetime.

This gives rise to Einstein equation

$$G_{ab} - \frac{3}{L^2}g_{ab} = 8\pi T^{\psi}_{ab} + 8\pi T^{\rm EM}_{ab}, \tag{2.6}$$

where the stress energy tensors are

$$8\pi T^{\rm EM}_{ab} = \frac{1}{2}\left(g^{cd}F_{ac}F_{bd} - \frac{1}{4}g_{ab}F_{cd}F^{cd}\right) \tag{2.7}$$

$$8\pi T^{\psi}_{ab} = \frac{1}{2}\left[(D_a\psi)^*(D_b\psi) + (D_a\psi)(D_b\psi)^*\right] - \frac{1}{2}g_{ab}|D_c\psi|^2. \tag{2.8}$$

The Maxwell equation,

$$\nabla^b\left(\nabla_b A_a - \nabla_a A_b\right) = iq\psi^* D_a\psi - iq\psi(D_a\psi)^*, \tag{2.9}$$

and the Klein-Gordon equation,

$$D^a D_a\psi - m^2\psi = 0. \tag{2.10}$$

We restrict the problem to spherical symmetry. Hence, the metric

$$ds^2 = -f(r)dt^2 + \frac{1}{f(r)}dr^2 + r^2 d\Omega_2^2, \tag{2.11}$$

where the metric function

$$f(r) = 1 - \frac{2M}{r} + \frac{Q^2}{r^2} + \frac{r^2}{L^2}, \tag{2.12}$$

with Maxwell field

$$A_\mu dx^\mu = \left(\frac{Q}{r} + C\right), \tag{2.13}$$

and vanishing scalar field, $\psi = 0$, solves the field equations. This corresponds to a charged black hole solution in anti- de Sitter (AdS) spacetime. Where L is the AdS length scale, M and Q are the Abbott-Deser (AD) mass and charge, respectively. We can see that $M = 0$ and $Q = 0$ we recover empty AdS, if $Q = 0$ we have a Schwarzschild-AdS black hole solution, and if L, M, and Q are non-vanishing we have a Reissner-Nordstrom-AdS black hole (RN-AdS) solution.

The $C\,dt$ term in the Maxwell field corresponds to pure gauge. It is common to choose $C = \frac{Q}{r_{\rm H}}$ to set $A(r_{\rm H}) = 0$, which is convenient for studying the near-horizon geometry. For our numerical implementation and the linearized analysis we will take $C = 0$, so that $A(\infty) = 0$. Under a gauge change $C \to C + \Delta C$, the scalar field undergoes a frequency shift $\psi \to e^{iq\Delta C t}\psi$.

The metric Eq. (2.11), with metric function Eq. (2.12) with non-vanishing L, M, and Q is the RN-AdS black hole metric. The AdS length scale is defined by $L \equiv \sqrt{-3/\Lambda}$ with

Λ being the cosmological constant. The event horizon r_+ and the Cauchy horizon r_- are the two real roots of $f(r) = 0$, as depicted in its Penrose diagram in Fig. 2.1. Thus, we can write the mass M in terms of the charge Q and the event horizon radius r_+,

$$M = \frac{r_+}{2} + \frac{r_+^3}{2L^2} + \frac{Q^2}{2r_+}. \tag{2.14}$$

The Hawking temperature is

$$T = \frac{1}{4\pi}\left(\frac{d\ f(r)}{dr}\right)\Bigg|_{r=r_+} = \frac{1}{4\pi r_+}\left(1 - \frac{Q^2}{r_+^2} + \frac{3r_+^2}{L^2}\right), \tag{2.15}$$

and requiring its positive definiteness we can constrain the charge Q as follows

$$Q \leq Q_{\text{ext}} \equiv r_+\sqrt{1 + \frac{3r_+^2}{L^2}}, \tag{2.16}$$

where Q_{ext} is the maximum value for the charge. We use the ratio

$$0 \leq \alpha \equiv Q/Q_{\text{ext}} \leq 1 \tag{2.17}$$

to quantify the amount of charge in the black hole. In Sec. A.1 we express the metric function, the mass and the charge in terms of the inner and outer horizon radii r_- and r_+, respectively.

2.1.2 Separation of the Klein-Gordon Equation

While equations (2.6), (2.9), and (2.10) describe the fully nonlinear evolution of the system, we will use perturbation theory to first approach the problem, that is we will consider the scalar field ψ to be small of order $\mathcal{O}(\varepsilon)$. In doing so, we will be able to obtain the quasinormal mode frequency and radial profile of the modes which will be needed in the analysis and discussion further down the line. Given that the stress-energy tensor in Eq. (2.6) and the current in Eq. (2.9) are quadratic in the scalar field, to order $\mathcal{O}(\varepsilon)$ the gravitational and the gauge sectors remain the same. It can be thought of as the scalar field propagating on a fixed Reissner-Nordstrom-AdS geometry. The backreaction onto the metric and the gauge field comes at order $\mathcal{O}(\varepsilon^2)$ in the scalar field.

Assuming the charged scalar field is propagating on the Reissner-Nordstrom-AdS background, the equation for a minimally coupled charged scalar field in this curved spacetime is

$$\left(\nabla_a - iqA_a\right)\left(\nabla^a - iqA^a\right)\psi - m^2\psi = 0. \tag{2.18}$$

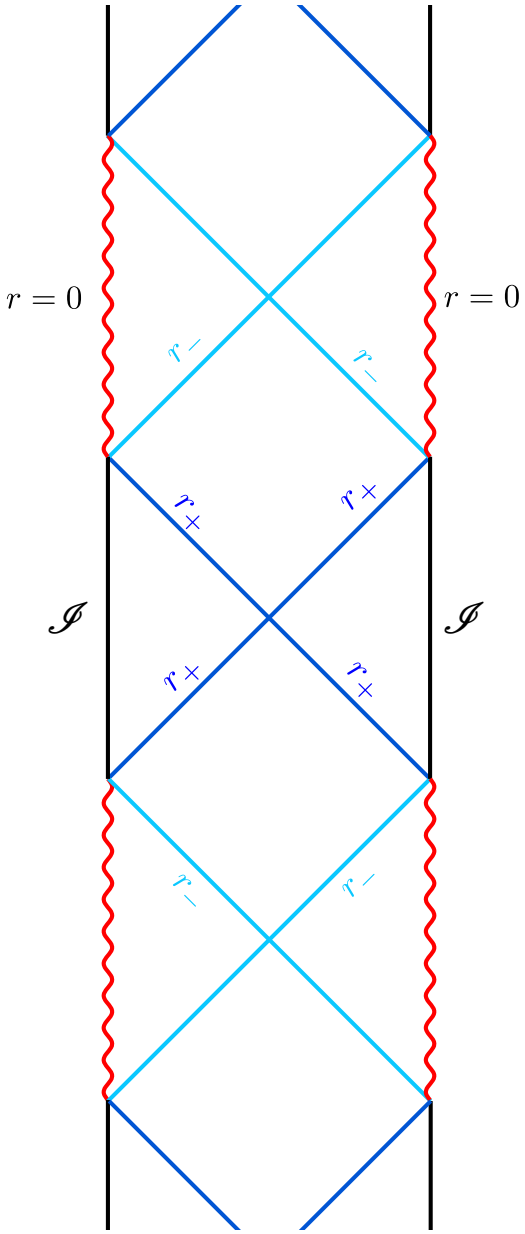

Figure 2.1: Penrose diagram for a part of the maximal analytical extension of Reissner-Nordström-AdS black hole Eqs. (2.11) and (2.12). The dark blue lines are the future/past outer event horizons $\mathcal{H}^{\pm}$ at r_+. The light blue lines are the inner Cauchy Horizons at r_-. The red squiggly lines are the singularity at $r = 0$, and the thick black vertical lines are the AdS timelike boundary $\mathscr{I}$.

Imposing spherical symmetry, the Klein-Gordon equation 2.18 take the form

$$-\frac{1}{f}\partial_t^2\psi+\frac{2iqA_0}{f}\partial_t\psi+\frac{1}{r^2}\partial_r\left(r^2f\ \partial_r\psi\right)-\left(m^2-\frac{q^2A_0^2}{f}\right)\psi=0. \tag{2.19}$$

Separating the equation using the ansatz

$$\psi(t,r,\theta,\phi)=e^{-i\omega t}R(r)Y_{lm}(\theta,\phi), \tag{2.20}$$

where $Y_{lm}(\theta,\phi)$ are the usual spherical harmonics, $R(r)$ is the radial wavefunction and ω is a complex frequency. Then the Klein-Gordon equation (2.18), in Schwarzschild coordinates, reduces to the radial equation

$$\frac{d}{dr}\left(r^2f\frac{dR}{dr}\right)+\left(\frac{(\omega r^2-qQr)^2}{r^2f}-l(l+1)-m^2r^2\right)R=0. \tag{2.21}$$

Furthermore, we have chosen the gauge $C=0$ for the Maxwell field, in Eq. (2.13). The charge of the black hole is denoted by Q, q is the gauge coupling, m is the mass of the scalar field, and f is the metric function of Eq. (2.11). We will use this form of the radial equation to compute the quasinormal frequencies. Additionally, in what follows, we will also use the radial equation in ingoing Eddington-Finkelstein coordinates to obtain the radial function related to each individual frequency.

Solving Eq. (2.21) is not a trivial matter since we need to know the value of the frequency ω corresponding to the radial solution $R(r)$ we're looking for. The frequencies ω are not purely real frequencies as would be the case for perturbed non-dissipative physical systems, they are complex frequencies displaying the fact that gravitational systems are dissipative systems. The imaginary part of the frequency will inform us on the timescales involved for the perturbation to decay away.

2.1.3 Quasinormal frequencies

The study of black hole perturbations due to linearized fields of spin s can be reduced to the study of a Schröginger-type equation of the form

$$\frac{d^2\Psi_s}{dr_*^2}+(\omega^2-V_s)\Psi_s=0, \tag{2.22}$$

the subscript s refers the the spin of the field and will be set to $s=0$ henceforth, Ψ_s is the radial wave function, and where we define the "tortoise" coordinate as

$$\frac{dr_*}{dr}=\frac{1}{f(r)}, \tag{2.23}$$

with f the metric function of Eq. (2.11). To determine the modes of oscillations of the black hole, we have to solve this ordinary differential equation with the appropriate boundary conditions at the horizon ($r_* \to -\infty$) and at spatial infinity ($r_* \to \infty$).

The boundary conditions at the horizon correspond to only ingoing modes, since classically nothing should leave the horizon. For most spacetimes the potential $V \to 0$ as $r_* \to -\infty$. In this limit the solutions to the wave equation Eq. (2.22) behave like $\Psi \sim e^{-i\omega(t\pm r_*)}$. Choosing only the ingoing modes, which correspond to the plus sign, the boundary condition at the horizon takes the form

$$\Psi \sim e^{-i\omega(t+r_*)}, \qquad r_* \to -\infty \ (r \to r_+). \tag{2.24}$$

The boundary conditions at spatial infinity for asymptotically anti-de Sitter spacetimes differs from the general approach of only outgoing waves at spatial infinity in asymptotically flat. When the cosmological constant does not vanish, then, the field must behave like

$$\Psi \sim \frac{A}{r^2} + Br, \qquad r \to \infty, \tag{2.25}$$

for a scalar field perturbations. For regular scalar perturbations we need $B = 0$, corresponding to Dirichlet boundary conditions at infinity. For electromagnetic and gravitational perturbations the boundary conditions have a slightly different decay at infinity, and the boundary conditions one has to impose are less clear.

In our case, the perturbation of a RN-AdS black hole by a charged scalar field, we can rewrite the radial equation Eq. (2.21) in the Schrödinger-like form of Eq. (2.22) with the potential

$$V(r) = -f\left(\frac{l(l+1)}{r^2} + \frac{f'}{r} + m^2\right) - \frac{2qQ\omega}{r} + \frac{q^2Q^2}{r^2} \tag{2.26}$$

where r is defined in terms of $r*$ through Eq. (2.23).

From the previous analysis we can obtain the appropriate boundary conditions for the radial function $R(r)$ in Eq. (2.21),

$$R(r) \sim \begin{cases} (r-r_+)^{\pm\frac{iL^2 r_+(r_+\omega - qQ)}{(r_+ - r_-)\left(L^2 + r_-^2 + 3r_+^2 + 2r_- r_+\right)}} & \text{as } r \to r_+, \\ r^{\frac{1}{2}\left(\pm\sqrt{4m^2L^2+9}-3\right)} & \text{as } r \to \infty. \end{cases} . \tag{2.27}$$

We require the solution to decay at infinity so we take the solution with the minus sign as $r \to \infty$, this corresponds to reflecting boundary conditions at the AdS boundary. For the

ingoing wave conditions at the horizon we choose the minus sign of the solution, as well, as $r \to r_+$.

To determine the QNM and their frequencies we solve the eigenvalue problem presented in Eq. (2.22), with boundary conditions Eq. (2.27). We will use the *continued fraction method* to compute the QNM frequencies. Leaver used this method to compute the QNM frequencies of Schwarzschild and Kerr geometries in asymptotically flat [44, 46, 45].

We compute these QNM frequencies following Leaver's general approach [44, 47], where we expand the solution as

$$R(r) = (r - r_+)^A (r - r_-)^{B-A} F(u), \tag{2.28}$$

where

$$A = -\frac{iL^2 r_+ \left(r_+\omega - qQ\right)}{\left(r_+ - r_-\right)\left(L^2 + r_-^2 + 3r_+^2 + 2r_- r_+\right)}, \tag{2.29}$$

$$B = -\frac{1}{2}\left(\sqrt{4m^2L^2 + 9} + 3\right), \tag{2.30}$$

and where $F(u)$ is a new unknown function with $u = (r - r_+)/(r - r_-)$. If F is smooth on $u \in [0, 1]$ then R satisfies the desired asymptotic conditions.

We can expand F as a power series

$$F(u) = \sum_{n=0}^{\infty} a_n(\omega) u^n, \tag{2.31}$$

with u as defined above. Using the series expansion form of Eq. (2.28) we substitute it back into Eq. (2.21). We obtain a recursion relation for the a_n, which can be simplified into a three-term recursion relation using Gaussian reduction. Thus, we obtain a relation of the form

$$\begin{aligned} \alpha_0 a_1 + \beta_0 a_0 &= 0, \\ \alpha_n a_{n+1} + \beta_n a_n + \gamma_n a_{n-1} &= 0, \qquad n \geq 1, \end{aligned} \tag{2.32}$$

where α_n, β_n, and γ_n depend on the parameters of the system and the frequency ω. If the series Eq. (2.31) converges uniformly for some value ω, then that value of the frequency corresponds to a quasi-normal frequency.

The method relies on the fact that the power series Eq. (2.31) converges uniformly if the continued fraction

$$\frac{-\gamma_1}{\beta_1 - \frac{\alpha_1\gamma_2}{\beta_2 - \frac{\alpha_2\gamma_3}{\beta_3 - \cdots}}} \tag{2.33}$$

converges. Furthermore, if it is in fact the case that the continued fraction converges then it converges to a_1/a_0. This allow us to close the recurrence relation Eq. (2.32) with

$$\frac{-\gamma_1}{\beta_1 - \frac{\alpha_1\gamma_2}{\beta_2 - \frac{\alpha_2\gamma_3}{\beta_3 - \cdots}}} = -\frac{\beta_0}{\alpha_0}. \tag{2.34}$$

We solve Eq. (2.34) by truncating the continued fraction up to a number N of terms. The accuracy of the method will depend directly in the number of terms included. We use the numerical values of ω that solve Eq. (2.34), given N, as the quasi-normal frequencies.

The *continued fraction method* is a successful algorithm to compute the QNM frequencies, specially overtone frequencies, however, it is purely numerical [44]. Other methods, for example the WKB approximation or the Pösch-Teller approximation, rely on approximating the potential and finding analytic solutions to the radial wave function and the QNM frequencies [48]. The analytical intuition, however, comes at the cost of the precision in the QNM frequencies.

2.1.4 Radial function

In Chapter 4 we will use *special* initial data which we construct by solving the radial equation. We use ingoing Eddington-Finkelstein coordinates for the full nonlinear evolution of the system. Hence, we will solve the radial equation in those same coordinates. To do so we use our implementation of Leaver's method which provides the quasi-normal frequency spectrum for a complex scalar field perturbation on a RN-AdS background.

In fact, one could obtain the radial profile from the series expansion Eq. (2.28) using up to a number N of terms and apply an appropriate coordinate transformation. Our goal is to include as little (numerical) noise as possible, however, and solving the radial equation in the same coordinates than the nonlinear evolution code proved to be our most successful approach. We know that the quasi-normal frequencies are robust by performing convergence analysis, and we choose the number of terms N included in the series expansion within this convergent regime.

We set the background metric to ingoing Eddington-Finklestein coordinates

$$ds^2 = -f(r)dv^2 + 2dvdr + r^2 d\Omega_2^2. \tag{2.35}$$

We use this metric to compute the equation of the charged scalar field propagation on a RN-AdS background Eq. (2.18). Then, we make a mode decomposition of the complex scalar field

$$\psi(v, r, \theta, \phi) = e^{-i\omega v} R(r) Y_{lm}(\theta, \phi), \tag{2.36}$$

where Y_{lm} are the usual spherical harmonics, and with the ingoing null coordinate $v = t+r_*$. Thus, the Klein-Gordon equation (2.18) in these coordinates reduces to the radial equation

$$fR^{''}(r)+R^{'}(r)\left[f^{'}-2i\omega+\frac{2f}{r}-2iq\Phi\right]+R(r)\left[-m^2-\frac{l(l+1)}{r^2}-\frac{2i(\omega+q\Phi)}{r}-iq\Phi^{'}\right]=0, \tag{2.37}$$

where the primes denote radial derivatives, f is the metric function of Eq. (2.35), Φ is the electrostatic potential, and we have set the separation constant $\lambda = l(l+1)$ to zero.

To obtain the radial profiles for individual modes we will solve Eq. (2.37) for each desired frequency ω, with reflecting boundary conditions at the AdS boundary. With this approach we are able to construct precise radial mode functions for different overtones ($n = 0, 1, 2, \ldots$). In Chapter 4 we will use this procedure to construct radial overtone mode profiles which we will use as *special* initial data, and evolve nonlinearly.

2.2 Characteristic Formulation

We adopt a null coordinate formulation which is well suited to our scattering problem. We use spherically symmetric ingoing Eddington-Finkelstein coordinates for black holes as a metric ansatz. It provides a null slicing of the spacetime constructed from infalling null geodesics, and leads to a characteristic formulation of the gravitational dynamics. Moreover, the metric remains regular across the future event horizon, and provides good coordinates covering the entire domain. Another advantage of choosing this approach is that the gauge freedom is significantly restricted. Lastly, this choice will yield a set of evolution equations which are well suited for a marching algorithm, simplifying the computational strategy.

2.2.1 General Motivation

The Einstein equations are highly nonlinear coupled partial differential equations, and solving them, in general, represents a difficult task. Known analytical solutions, generally, have a high degree of symmetry, and are static or stationary metrics. For highly dynamical scenarios, even with symmetry assumptions included, it becomes increasingly challenging to use analytical methods. Numerical implementation of Einstein equations is, then, required for those type of problems.

Einstein equations in their covariant form are not well suited for numerical implementation. To do so, they need to be reformulated into a well-posed initial value problem for

which a numerical solution could be found using a stable (convergent) algorithm. Several well-posed formulations of the Einstein equations have been proposed and tested throughout the years. These include the constrained Arnowitt-Deser-Misner (ADM), the hyperbolic Baumgarte-Shapiro-Shibata-Nakamura (BSSN) [49, 50], and the generalized harmonic (GH) formulation [51, 52, 53], to name a few. The GH formulation attracted significant attention due to its use in the first long-term evolution of binary black hole inspiral and merger. The BSSN formulation, however, has also been a popular choice for long-term evolution of compact objects. In this thesis we focus on the specific approach known as characteristic evolution [54]. This form of the Einstein equations have been used for the evolution of single black holes, as well as for the extending the Cauchy evolution to future null infinity, where the extraction of gravitational waves is well defined [54].

In general, the method of characteristics is a tool to solve hyperbolic partial differential equations (PDE). It finds *characteristic curves* along which the the PDE is reduced to a family of ordinary differential equations (ODE). Then, the solution can be found by integrating the ODEs along these *characteristic curves*, provided suitable initial data. In our case, these characteristic curves are null hypersurfaces that will provide the foliation needed for the implementation of a numerical evolution scheme. A typical choice is to use two null hypersurfaces (*double null* approach), however, in our case the spacetime will be foliated by single null hypersurfaces [2].

A property of the characteristic formulation, in stark contrast with the other approaches aforementioned, is that the gauge or "coordinate" freedom is rather restricted, and needs to be fixed at a given hypersurface. Common choices for the hypersurface are a timelike worldtube, that sometimes is collapsed into a timelike worldline; the use of a second null hypersurface, also known as the *double null* approach; or spacelike hypersurfaces, which are used for Cauchy-characteristic matching. In our case, we use the AdS boundary as the timelike worldline. An important advantage of this method is the fact that there are no elliptic constraints on the data, so some of the initial data is free. The rest must be obtained by solving constraints on the hypersurface, but these are simple radial integrations. Additionally, there are no second derivatives in time, *i.e.* along the null direction, so there are fewer variables, and the resulting system of coupled ODEs can be solved using a marching algorithm. Furthermore, null infinity can be compactified and brought to a finite coordinate distance.

In what follows we provide the details of our implementation used to solve the scattering

[2]The domain of dependence of single (non-singular) hypersurfaces is empty. In global anti-de Sitter spacetime there is a timelike boundary at infinity which provides the additional boundary needed to have a non-trivial domain of dependence. From this remark we see that the the AdS boundary plays an important role, and, hence, an appropriate treatment of the boundary conditions is required.

of a complex scalar field off of a charge black hole in asymptotically AdS spacetime. Our implementation follows the structure of Chesler and Yaffe's formulation [55].

2.2.2 Metric Ansatz

We will be adapting the method outlined in [55] to our specific problem, with a few differences along the way. We will use a metric ansatz which greatly restrict the diffeomorphism freedom and is consistent with the physical symmetries of the problem at hand, and is well suited for gravitational infall problems. The metric ansatz we choose is the standard ingoing Eddington-Finkelstein coordinates, which will lead to a characteristic formulation of the equations of motion. Hence, the spacetime is foliated by null infalling geodesics. Furthermore, we are restricting the problem to spherical symmetry, hence, the metric takes the form

$$ds^2 = -A(v,r)dv^2 + 2dvdr + \Sigma(v,r)^2 d\Omega_2^2, \tag{2.38}$$

where v is the null time coordinate, r the non-inverted radial coordinate, and with the spacetime boundary at $r \to \infty$. From the metric we can see that the lines along which r is allowed to vary while keeping the other coordinates fixed are null curves, hence, the radius parameterizes the infalling null geodesics.

Another advantage of using ingoing Eddigton-Finkelstein coordinates is that they are horizon penetrating coordinates. Hence, the are regular across the event horizon of a black hole spacetime. This is useful since we will implement an excision scheme by means of an apparent horizon finder, which generically will lie inside the event horizon, so the event horizon will be included in the computational domain. In this way our grid domain is free of coordinate singularities at the horizon.

2.2.3 Equations of Motion

We have adopted ingoing Eddington-Finklestein coordinates in spherical symmetry, Eq. (2.38). For the Maxwell field we choose a gauge such that

$$A_\mu dx^\mu = W(v,r)dv, \tag{2.39}$$

and require that the scalar field $\psi = \psi(v,r)$. Replacing the fields in the Einstein equations, Eqs. (2.6), the Maxwell equations, Eqs. (2.9), and the Klein-Gordon equation, Eq. (2.10),

the equations of motion take the form, for the Einstein field equations

$$0 = \Sigma(d_+\Sigma)' + (d_+\Sigma)\Sigma' - \frac{3}{2L^2}\Sigma^2 - \frac{1}{2} + \frac{1}{8}\Sigma^2 W', \tag{2.40}$$

$$\begin{aligned} 0 = {} & A'' - \frac{4}{\Sigma^2}(d_+\Sigma)\Sigma' + \frac{2}{\Sigma^2} + (\psi')^* d_+\psi \\ & + \ (d_+\psi)^*\psi' - (W')^2 + iqW\left[\psi^*\psi' - (\psi')^*\psi\right], \end{aligned} \tag{2.41}$$

$$\begin{aligned} 0 = {} & d_+ d_+\Sigma - \frac{1}{2}A' d_+\Sigma + \frac{1}{2}\Sigma|d_+\psi|^2 + \frac{1}{2}q^2W^2\Sigma|\psi|^2 \\ & + \ \frac{1}{2}iqW\Sigma\left[\psi^* d_+\psi - \psi(d_+\psi)^*\right], \end{aligned} \tag{2.42}$$

$$0 = \Sigma'' + \frac{1}{2}\Sigma|\psi'|^2, \tag{2.43}$$

for the Maxwell equations,

$$\begin{aligned} 0 = {} & (d_+W)' - \frac{1}{2}A'W' + 2\frac{d_+\Sigma}{\Sigma}W' - 2q^2W|\psi|^2 \\ & + \ iq\left[\psi^* d_+\psi - \psi(d_+\psi)^*\right], \end{aligned} \tag{2.44}$$

$$0 = W'' + \frac{2}{\Sigma}\Sigma' W' + iq\left[\psi^*\psi' - \psi(\psi')^*\right], \tag{2.45}$$

for the Klein-Gordon equation,

$$\begin{aligned} 0 = {} & 2(d_+\psi)' + 2\frac{\Sigma'}{\Sigma}d_+\psi + 2\frac{d_+\Sigma}{\Sigma}\psi' - iq\psi W' \\ & - \ 2iq\frac{\Sigma'}{\Sigma}W\psi - 2iqW\psi', \end{aligned} \tag{2.46}$$

where we denote $f' \equiv \partial_r f$, and the derivative along the outgoing null direction, $d_+ f \equiv \partial_v f + \frac{1}{2}A\partial_r f$.

The metric ansatz has a remaining shift symmetry, which will become apparent in the asymptotic expansion, in the choice of radial coordinate. An arbitrary radial shift

$$r \to \bar{r} = r + \lambda(v), \tag{2.47}$$

and metric functions that transform as

$$A(v,r) \to \bar{A}(v,\bar{r}) \equiv A(v,\bar{r} - \lambda(v)) + \partial_v\lambda(v), \tag{2.48}$$

will leave the metric (2.38) invariant. The derivative introduced in the equations of motion

$$d_+ \equiv \partial_v + \frac{1}{2}A(r)\partial_r, \tag{2.49}$$

transforms covariantly under arbitrary radial shifts of the form (2.47). This is helpful to write expressions in a way which makes explicit the invariance under the radial shift symmetry. Thus, we have that ∂_r will be a directional derivative along the ingoing radial null geodesic and d_+ is the directional derivative along the outgoing null geodesics.

2.2.4 Asymptotic Expansion

To set the appropriate boundary conditions for the equations of motion to be solved we do an asymptotic expansion for the relevant fields. Specifically, we will solve the equations of motion imposing reflecting boundary conditions at $r \to \infty$, which corresponds to the AdS timelike boundary.

Using expansions of the form

$$\begin{aligned} A &= \sum_{i=-2} \frac{a_i}{r^i}\,, \qquad \Sigma \;\; = \sum_{i=-1} \frac{\sigma_i}{r^i}\,, \\ W &= \sum_{i=0} \frac{w_i}{r^i}\,, \qquad \psi \;\; = \sum_{i=0} \frac{\varphi_i}{r^i}, \end{aligned} \tag{2.50}$$

noting the different extents of the indices i, we can substitute them back into the equations and solve for the coefficients $\{a_i, \sigma_i, W, \varphi_i\}$. Thus, the asymptotic expansions take the form

$$\begin{aligned} A = \frac{r^2}{L^2} + \lambda(v)r + \left(1 + \frac{L^2\lambda(v)^2}{4} - L^2\partial_v\lambda(v)\right) - \frac{2M}{r} \\ + \left(L^2\lambda(v)M + \frac{Q^2}{4}\right)\frac{1}{r^2} + \mathcal{O}(r^{-3}) \end{aligned} \tag{2.51}$$

$$\Sigma = r + \frac{L^2\lambda(v)}{2} + \mathcal{O}(r^{-5}) \tag{2.52}$$

$$W = \nu(v) + \frac{Q}{r} + \mathcal{O}(r^{-2}) \tag{2.53}$$

$$\psi = \frac{\varphi_3(v)}{r^3} + \mathcal{O}(r^{-4}). \tag{2.54}$$

The constants M and Q represent the Abbott-Deser (AD) mass and charge [56], respectively. In what follows, these will be prescribed as boundary data. The functions $\lambda(v)$ and $\nu(v)$ are the remaining gauge freedom discussed previously. Namely, $\lambda(v)$ is related to the radial shift Eq. (2.47), which leaves the metric invariant, and $\nu(v)$ corresponds to C in the Maxwell field in Eq. (2.13), which is pure gauge. The function $\varphi_3(v)$ is an unknown function that is determined by the solution. In fact, this will be the output of the simulation.

As mentioned previously, we will make the gauge choice $\nu(v) = 0$ for the Maxwell field A, so that it does to zero when $r \to \infty$. Another common choice is $\nu(v) = -\frac{Q}{r_+}$ so that the the Maxwell field vanishes at the horizon, which is a convenient gauge to study the near-horizon geometry of the black hole. Moreover, the remaining radial shift freedom $\lambda(v)$ can be freely specified, and can be used to specify the location of the apparent horizon as done in [55] and [3]. In those cases exploiting freedom in $\lambda(v)$ to set the location of the apparent horizon at a constant radial coordinate is quite useful since it keeps the computational domain constant and makes it easier to implement spectral methods. However, in our case, we choose to set $\lambda(v) = 0$, find the apparent horizon at each incoming null surface and excising a number of grid points inside of it. Additionally, instead of pseudospectral methods we will employ finite differences with derivatives satisfying summation by parts [57, 58]. Furthermore, setting $\lambda(v) = 0$ allows us to identify Σ as the areal radius.

2.2.5 Propagating fields and auxiliary fields

Upon closer inspection of the equations of motion (2.40)-(2.46), we can identify (2.41), (2.43), and (2.45) as linear second order radial ordinary differential equations (ODE) for A, Σ, and W. Furthermore, the Einstein equation (2.40) and the scalar equation (2.46) are first order radial ordinary differential equations for the modified time derivative d_+ of Σ and ψ.

Given that there are no time derivatives of the functions A, Σ, and W in the equations (2.41), (2.43), and (2.44), we consider them as being auxiliary fields. To find A, Σ, and W, we integrate their respective second order radial ODE on every time slice after determining the fields appearing in the source term of their respective equations, and with their appropriate boundary conditions. In this sense, the auxiliary field are completely local in time. We will consider $d_+\Sigma$ as an independent field, and upon inspection of Eq. (2.40) we determine it to be an auxiliary field as well.

The scalar field will contain all the propagating information, and it is the field that will be evolved forward in time. From Eq. (2.46) we obtain $d_+\psi$ and use the definition of

the modified derivative d_+ to get $\partial_v \psi$ at that given time slice. Having this, we can evolve forward one step in time. Thus, the scalar field will be the only propagating field.

The remaining two equations (2.42) and (2.44) are redundant, and may be viewed as boundary value constraints. Our evolution scheme does not rely on these constraint equations , *i.e.* it is a *free evolution* scheme. We do monitor them, however, at each time step, and use them as independent residuals to test and have an estimate of the accuracy of the fully nonlinear numerical code.

2.2.6 Apparent Horizon

Motivated by the black-hole-excision strategy first proposed by Unruh, we implement a *singularity excision* method to excise the black hole's interior region from the computational domain of integration. It is crucial, then, to be able to locate the black hole's *horizon* at each time slice, and to be certain that the excised region is located *within* that horizon.

We need to make the distinction between the different types of horizons related to black holes. The event horizon is the boundary between null geodesics that reach future null infinity and the null geodesics that fall back into the black hole. The event horizon is defined in a global way, so one needs to know *a priori* the full evolution of the spacetime to be able to locate it. On the other hand, apparent horizons are defined locally as the outermost marginally trapped surface on a given hypersurface. A closed 2-surface is trapped if the expansion of the outgoing null geodesics orthogonal to the surface is negative everywhere on the surface. It will be a marginal trapped surface if the expansion of the outgoing null geodesic orthogonal to the surface vanishes everywhere on the surface. Provided cosmic censorship and the null energy conditions are satisfied, the apparent horizon will lie inside the event horizon. Furthermore, for stationary spacetimes the apparent horizon and the event horizon will coincide. The apparent horizon is a local-in-time quantity that can be computed at each time slice during the evolution. We will use the location of the apparent horizon to excise the interior of the black hole during the evolution.

To find the apparent horizon during the evolution we need to compute the expansion of null geodesics

$$\theta_{\rm out} = \nabla_\mu k^\mu = \frac{1}{\sqrt{-g}} \partial_\mu \left(\sqrt{-g}\ k^\mu \right), \tag{2.55}$$

where θ is the expansion and k^μ is the tangent vector of the outgoing null geodesic congruence. Using the metric ansatz Eq. (2.38), and $k^\mu = \alpha \left(1, \frac{A}{2}, 0, 0\right)$, the expansion takes the form

$$\theta_{\rm out} = \frac{2\alpha}{\Sigma} \left(\partial_v \Sigma + \frac{A}{2} \partial_r \Sigma \right). \tag{2.56}$$

Furthermore, we identify the term between brackets as the modified time derivative $d_+\Sigma$, and combined with the fact we are looking for surfaces with vanishing expansion $\theta_{\rm out}$ at the apparent horizon, we get the rather simple condition

$$d_+\Sigma|_{r_{\rm AH}} = 0. \tag{2.57}$$

In other implementations [55, 3] the residual radial reparametrization freedom is used to pin the apparent horizon at a fixed radial position. Thus, the computational domain becomes a simple rectangular region which is well suited for pseudo-spectral methods. In our implementation, we set the residual radial shift of Eq. (2.47) to $\lambda(v) = 0$, thus the horizon will not be at a fixed location throughout the evolution. We will find the apparent horizon at each incoming null surface and excise a number of grid point inside it. For our convenience we will use a finite difference implementation instead of a pseudo-spectral one.

2.2.7 Field Redefinition and domain compactification

In order to discretize the spacetime we adopt a compact spatial domain as to include the AdS boundary ($\mathscr{I}$) in our computational grid and ensure the full equations are consistently implemented. Hence, we introduce the inverse radial coordinate $\rho = 1/r$ as our spatial coordinate and define new variables,

$$A(v,r) = \alpha(v,1/r) = \alpha(v,\rho), \tag{2.58}$$
$$\Sigma(v,r) = \sigma(v,1/r) = \sigma(v,\rho), \tag{2.59}$$
$$d_+\Sigma(v,r) = s(v,1/r) = s(v,\rho), \tag{2.60}$$
$$W(v,r) = w(v,1/r) = w(v,\rho), \tag{2.61}$$
$$\psi(v,r) = \varphi(v,1/r) = \varphi(v,\rho), \tag{2.62}$$
$$d_+\psi(v,r) = \Pi(v,1/r) = \Pi(v,\rho). \tag{2.63}$$

From the asymptotic expansions, Eqs. (2.51)-(2.54), we see that the metric functions A and Σ, as well as $d_+\Sigma(v,\rho) \sim 1+\rho^{-2}L^{-2}+\mathcal{O}(\rho)$, diverge as we approach the AdS boundary $\rho \to 0$ ($r \to \infty$). It is convenient to redefine the fields such that their leading divergent piece is removed, and they vanish linearly as we approach the boundary at $\rho \to 0$. This procedures diminishes the loss of precision, which would otherwise occur, near the boundary $\rho = 0$ [55]. Let us use $d_+\Sigma(v,r) = s(v,\rho)$ as an explicit example of the field redefinition. The asymptotic expansion, in the compact radial coordinate and with $\lambda(v) = 0$, is

$$s(v,\rho) = \frac{\alpha(v,\rho)}{2} = \frac{1}{2\rho^2 L^2} + \frac{1}{2} - \rho M + \frac{\rho^2 Q^2}{8} + \mathcal{O}(\rho^3). \tag{2.64}$$

Now, if we remove the first and second term, in fact, we remove the divergent piece and the field vanishes linearly. Upon inspection of the other fields, we notice this can be done by a adding $-\sigma(v,\rho)^2 L^{-2}/2 - 1/2$ to $s(v,\rho)$. Hence, the redefined field $\hat{s}$ will have the desired properties. If the field does not have a divergent term, then a simple rescaling by an appropriate power of ρ will be enough to get the desired linear leading term. Using these guidelines, we introduce the redefined fields used in our numerical work:

$$\hat{\alpha} = \alpha - \frac{1}{L^2}\sigma^2 - 1, \tag{2.65}$$

$$\hat{\sigma} = \sigma - \frac{1}{\rho}, \tag{2.66}$$

$$\hat{s} = s - \frac{1}{2L^2}\sigma^2 - \frac{1}{2}, \tag{2.67}$$

$$\hat{w} = w, \tag{2.68}$$

$$\hat{\varphi} = \frac{1}{\rho^2}\varphi, \tag{2.69}$$

$$\hat{\Pi} = \frac{1}{\rho}\Pi. \tag{2.70}$$

Given that equations (2.41),(2.43), and (2.45) have second order spatial derivatives, we will introduce the three new fields $\hat{\beta} = \partial_\rho \hat{\alpha}$, $\hat{\tau} = \partial_\rho \hat{\sigma}$, and $\hat{z} = \partial_\rho \hat{w}$. With the compact domain we can impose the asymptotic conditions as boundary conditions at $\rho = 0$. In Table 2.1 we show the explicit boundary conditions for the redefined fields and their derivatives. Some equations of motion involve 0/0-type terms at the boundary $\rho = 0$. In those cases we impose explicitly the boundary conditions directly on the radial derivatives, with the values shown in Table 2.1. We regularize the equations via the L'Hôpital rule where needed. Furthermore, the equation for $\hat{s}$ is of the form $\partial_\rho \hat{s} \sim \hat{s}/\rho + \cdots$, which is problematic as its regularization leaves no equation. We solve this problem by using a 2nd order implicit scheme for this equation.

2.2.8 Marching Algorithm

As a result of the characteristic formulation, the set of equations (2.40)-(2.46) have a very convenient structure, which allows us to implement a simple integration strategy. In fact the set of equations we want to solve have no second time derivatives, and they form a system of coupled ODEs with respect to the parameter varying along the characteristics,

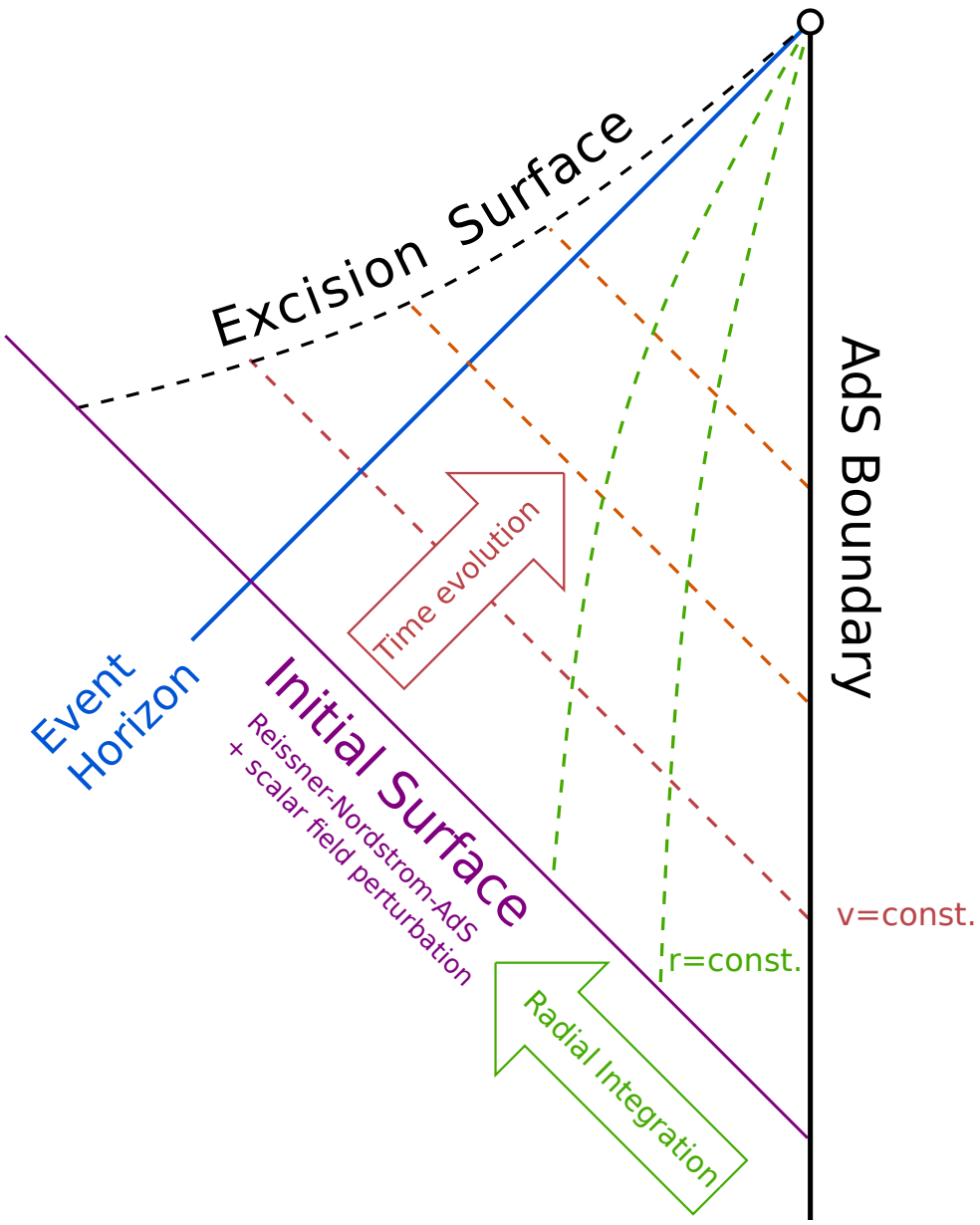

Figure 2.2: Schematic representation of the computational domain and our marching algorithm strategy. Initial data for the scalar field is provided on the initial surface. Additionally, the mass and the charge are provided as boundary values at the AdS boundary. We integrate radially inwards, from the boundary towards the horizon, all auxiliary fields. We find the apparent horizon at each $v = \text{const.}$ slice and excise its interior (leaving ~ 10 points inside the AH). Finally, we evolve the the scalar field forward in time, and repeat the procedure.

f	$f\|_{\rho=0}$	$\partial_\rho f\|_{\rho=0}$
$\hat{\alpha}$	$-L^2\lambda$	$-2M$
$\hat{\sigma}$	$\frac{L^2\lambda}{2}$	0
$\hat{s}$	0	$-M$
$\hat{w}$	ν	Q
$\hat{\varphi}$	0	φ_3
$\hat{\Pi}$	0	$-\frac{3\varphi_3}{2L^2}$
$\hat{\beta}$	$-2M$	$2L^2\lambda M + \frac{Q^2}{2}$
$\hat{\tau}$	0	0
$\hat{z}$	Q	$-L^2\lambda Q$

Table 2.1: Boundary conditions for the evolved fields and their derivatives

which in our case is the radial coordinate. This allows us to implement a marching algorithm along the characteristics. We show the schematic representation of the marching algorithm and our computational domain in Fig. 2.2.

As mentioned before, the AD mass and charge M and Q will be provided as boundary data, whereas for the scalar field we will use different profiles as initial data. For the radial derivatives of the scalar field we employ finite differences with derivatives satisfying summation by parts [57, 58]. Provided the initial and boundary data, and the gauge choices $\lambda = \nu = 0$ we are in good shape to address the marching algorithm we implemented.

The equations of motion for the redefined fields are obtained by substitution into the equations (2.40)-(2.46). Then, given appropriate boundary conditions M and Q, and initial data for the scalar field $\hat{\varphi}$, we solve the system of first order in space ODEs with a fourth-order Runge-Kutta integrator. We impose the initial value of each field at the AdS boundary $\rho = 0$, as shown in Tab. 2.1, and integrate towards the black hole. Once we have integrate radially all the fields, we are in position to move forward in time. We will make use of the modified time derivative of the scalar field $d_+\psi$, written in terms of the hatted fields, and use it to obtain $\partial_v\hat{\varphi}$ at time $v = v_0$. We can, thus, evolve forward in time, using a fourth-order Runge-Kutta method, as well, and iterate the procedure on the next $v =$ const. slice, as shown in Fig. 2.2.

The full equations are discretized using a uniform grid from the AdS boundary $\rho = 0$ to an inner radial value ρ_{inner}, with $\rho_i = (i-1)d\rho$ and $d\rho = \rho_{\text{inner}}/(N-1)$. The total number of points used to discretize the inverted radial coordinate is $N+1$. The domain stretches a number of grid points inside the apparent horizon, usually of order 10 grid points inside, such that $\rho_{\text{inner}} < \rho_{\text{AH}}$.

Null hypersurfaces are discretized in time with the time step separation $dv = \gamma d\rho$, where γ is the Courant-Friedrichs-Lewis (CFL) number. The typical value for the CFL number, in our runs, is $\gamma = 0.4$ to ensure we satisfy the CFL condition.

We showed the steps used in the marching algorithm we implemented to evolve the system of equations from a null time slice $v = v_0$ to the next slice at $v = v_0 + \delta v$. It is worth mentioning, that the characteristic formulation with the marching algorithm breaks down the process of solving highly nonlinear equations, into a sequence of steps whereby we solve linear first or second order radial ODEs and then we evolve forward the first order in time ODEs for the dynamical fields. The procedure described, however, is not unique and can be modified. For example, instead of treating the field Σ as an auxiliary field, one could choose to treat it as a dynamical field which is evolved using $d_+\Sigma$, and then extract $\partial_v\Sigma$. Even though this alternative would be formally equivalent to the one we adopted, it would give rise to a different implementation and algorithm with different numerical stability properties. It was shown in [55], however, that the numerical scheme enjoys improved stability if the auxiliary fields are computed at each null time slice, validating our choice of marching algorithm.

2.2.9 Initial Data

To integrate the system of equations we need to provide appropriate boundary and initial data. We need to provide the radial profile of the scalar field $\hat{\varphi}$ at some give null time slice $v = v_0$. The choice of initial data is arbitrary and there are few ways of specifying it.

We will mainly study two types of initial data, one where the mode content of the initial state is well known and correspond to states which would have a simple evolution if they were considered without backreaction onto the spacetime. The radial profile for the scalar field will be a quasi-normal mode, that is a solution to Eq. (2.37), with its corresponding quasi-normal frequencies. Furthermore, we will use this single mode radial profiles to construct multi-mode initial data by linear superposition.

On the other hand, to test the robustness and the independence of the dynamics on the initial data we use different generic radial profiles. In this case, the radial profile of the scalar field has some overlap with the specific modes which solve Eq. (2.37), however, the full general profile will not be a solution of the radial equation. Thus, we will use this type of initial data with small amplitude to perturb the black hole background and allow it to evolve dynamically.

Chapter 3

End State of the Superradiant Instability in RN-AdS

3.1 Introduction

In this chapter we study the nonlinear dynamics of the scattering of a charged scalar perturbation impinging on a RN-AdS black hole. When the perturbation is small, the description through a linearized analysis is suitable. Several studies have determined the quasi-normal mode spectra of Kerr-AdS [22], [27] and RN-AdS [6] in the small black hole regime, *i.e.* $r_+/L \ll 1$, where L is the AdS length scale. Hence, the instability has been identified in the linear regime.

Less is know about the final state of the instability, although it is, in general, expected to be a "hairy" black hole, that is, a black hole with a non-trivial profile of the perturbing field. A similar process occurs for RN-AdS black hole, with the charge playing the role of the angular momentum [21, 24, 25, 59]. Similarly, the end state of the charged superradiant instability is unclear. In the RN-AdS case, static BHs surrounded by a scalar field condensate have been constructed, and have been conjectured to be the endpoint of the instability [60, 61]. In the Kerr-AdS case, rotating black holes with a single helical Killing vector field have been constructed [62], but these black holes are unstable themselves and are, therefore, not plausible end points. The final state might be a hairy black hole without any symmetries, or the instability may lead to a violation of cosmic censorship [63]. Further complications arise from the fact that gravitational interactions can result in significant nonlinear mode coupling in confined geometries such as AdS, where dissipation is low [64, 65].

We study this scenario using the model described in Sec. 2.1.1, as well as the characteristic formulation of the problem to numerically evolve the perturbation forward in time, presented in Sec. 2.2. In the charged case, the instability is present even in spherical symmetry, and the instability time scale is shorter. We will track the perturbation solving the full nonlinear equations, allowing us to access the dynamics in the highly nonlinear regime. We will assess the final state of the perturbation, whether it's a runaway instability or a stationary hairy black hole, by tracking the area of the apparent horizon, the charge within the apparent horizon and the one in the scalar field. In addition we will look at the late-time behavior of the scalar field and the generalized Misner-Sharp mass, as well as comparing the late-time irreducible mass of the black hole to what would be the Schwarzschild-AdS equivalent. We will closely analyze the details of the nonlinear dynamics by means of a spectrogram, giving us an intuitive and unified picture of the charged superradiant instability. By studying this system, one could hope to draw some general conclusions that could be applied more broadly; for instance to the rotating case in asymptotically flat spacetime.

3.2 Superradiant Condition

It was shown by Bekenstein, that the superradiant condition can be easily understood from thermodynamic arguments [59]. The first law of black hole mechanics relates the change in mass M to the changes in horizon area $A_{\rm H}$, angular momentum J, and charge Q, of a stationary black hole when it is perturbed. The first law, then, is

$$\delta M = \frac{\kappa}{8\pi}\delta A_{\rm H} + \Omega_{\rm H}\delta J + \Phi_{\rm H}\delta Q, \tag{3.1}$$

where κ is the surface gravity, $A_{\rm H}$ is the horizon area, $\Omega_{\rm H}$ is the angular velocity of the horizon, and $\Phi_{\rm H}$ is the electrostatic potential at the horizon.

Let us consider a static charged black hole ($\Omega_{\rm H} = 0$) perturbed by a charged scalar field. The spacetime has a Killing vector field $\xi^\mu \equiv \partial^\mu t$. The conserved flux vector, for the stress-energy tensor of the scalar field $T^{\psi}_{\mu\nu}$, is

$$\varepsilon^\mu = -T^{\mu}_{\ \nu}{}^{\psi}\xi^\nu, \tag{3.2}$$

and the conserved current is

$$j_\mu = iq\psi^* D_\mu\psi - iq\psi(D_\mu\psi)^*. \tag{3.3}$$

Over a hypersurface $\mathrm{d}\Sigma_\mu$, the energy and charge fluxes are

$$\delta E = \varepsilon^\mu \, \mathrm{d}\Sigma_\mu, \qquad \delta Q = j^\mu \, \mathrm{d}\Sigma_\mu. \tag{3.4}$$

Over a spherical surface $\mathrm{d}\Sigma_\mu \equiv n_\mu r^2 dt \, d\Omega$, where n_μ is the radial outgoing normal vector to the surface. Hence, the charge to mass ratio is

$$\frac{\delta Q}{\delta E} = -\frac{j^r}{T^r{}_t}. \tag{3.5}$$

For a wave with (real) frequency ω, such that $\psi = e^{-i\omega t} R(r)$, the ratio of charge flux to energy flux at infinity is

$$\frac{\delta Q}{\delta E}\Big|_\infty = \frac{q}{\omega}, \tag{3.6}$$

where q is the charge of the wave. Thus, by conservation of charge and energy when the wave impinges upon the black hole, the change in energy δM, and charge δQ are to be related by

$$\frac{\delta Q}{\delta M} = \frac{q}{\omega}. \tag{3.7}$$

Now, using Eq. (3.7) back in the first law Eq.(3.1) relates the change in mass to the change in area of the black hole as a consequence of interacting with the mode,

$$\delta M = \frac{\kappa}{8\pi} \frac{\omega}{(\omega - q\Phi_{\mathrm{H}})} \delta A_{\mathrm{H}}. \tag{3.8}$$

Now, using the second law of black hole thermodynamics, $\delta A_{\mathrm{H}} \geq 0$; waves that extract energy from the black hole $\delta M < 0$ satisfy the condition

$$\omega < q\Phi_{\mathrm{H}}. \tag{3.9}$$

The interaction of a spinning black hole, with $\Phi_{\mathrm{H}} = 0$, with a scalar wave of frequency ω and azimuthal number m, can be computed in a similar way. The spacetime has two Killing vector fields which, contracted with the stress-energy tensor, give rise to the conserved energy flux and conserved angular momentum flux vectors. Using analogous arguments as above we get that the ratio of angular momentum to mass is

$$\frac{\delta J}{\delta M} = \frac{m}{\omega}. \tag{3.10}$$

Using Eq. (3.10) in Eq. (3.1) and invoking the second law of black hole thermodynamics gives rise to the superradiance condition

$$\omega < m\Omega_{\mathrm{H}}. \tag{3.11}$$

The two superradiance conditions Eqs. (3.9) and (3.11) display similar behavior for the charged and rotating black hole. One can relate the charge of the wave with the azimuthal number and the electrostatic potential of the black hole at the event horizon with the angular frequency at the event horizon.

Using the laws of black holes thermodynamics, one can understand the nature of the superradiant condition. However, the argument assumes that the waves are initially ingoing at infinity and that the matter fields satisfy the weak energy condition as required by the second law. For our purposes this argument holds, and gives rise to the superradiance condition Eq. (3.9) that we will use throughout.

The modes themselves are provided by the confinement mechanisms. For small RN-AdS black holes, that is $r_+/L \ll 1$, there is a set of modes that are deformations of the global AdS normal modes, which have real frequencies [6]

$$\omega_n^{\pm} = \pm\frac{2n+3}{L}, \quad n = 0, 1, 2, \cdot \, . \tag{3.12}$$

We therefore expect instability for ω_n^+ with

$$2n \lesssim qQ\frac{L}{r_+} - 3. \tag{3.13}$$

By choosing sufficiently large gauge coupling q, this condition should be easily satisfied.

3.3 Linear Regime

In this section we will use the characteristic formulation shown in Sec. 2.2, to dynamically evolve the nonlinear equations provided by the model in Sec. 2.1.1. We will touch base with the linear calculations that have been made for the small black holes regime [6], that is the radius of the black hole is much smaller than the AdS length scale, $r_+/L \ll 1$. We verify that the growth or decay rates, given a set of parameters, match the predictions made by linear theory. We confirm the onset of the instability for the fundamental mode, which follows from Eq. (3.13).

3.3.1 Recovering the QNMs

For small enough amplitudes of the perturbation, the dynamics follow the expected behavior from the linearized case. If the black hole is stable under such perturbations, the field

will decay in a rapid ringdown to the RN-AdS solution. In this scenario, we can analyze the decay timescale and the oscillation frequency of the field and compare them to the predictions made in the linearized case. If the black hole is unstable, a small perturbation of scalar field will undergo an exponential growth, like the linear analysis predicts. After some time of interacting with the black hole, the scalar field will backreact onto the black hole spacetime, causing it to lose charge and mass. When this takes place the nonlinear dynamics take over and we are no longer in the linear regime.

We start with the model described in Chap. 2, that is with a Lagrangian including the Einstein-Hilbert term, a negative cosmological constant, a Maxwell field, and a massless complex scalar field. We use the characteristic formulation to describe and evolve numerically the system. We will restrict to a region of the parameter space where the superradiant instability does not seem to take action, to be able to compare the decay rates of the scalar field to those of Uchikata & Yoshida's [6] linear calculations. By restricting to this specific region of the parameter space, even if we are solving the full nonlinear problem, we will be in the linear regime. That is, if the amplitude of the scalar field is small enough compared to the black hole, the backreaction will be negligible.

We prescribe compact support initial data for the scalar field on the initial null time slice, such that

$$\psi = \begin{cases} -(\rho-\rho_1)^3(\rho-\rho_2)^3\left(\kappa_1+\kappa_2\sin(\kappa_3\rho)\right) & \rho\in[\rho_1,\rho_2] \\ 0 & \text{otherwise} \end{cases}, \tag{3.14}$$

where $\rho_1 = \rho_{\text{in}} + 0.25\,(\rho_{\text{out}} - \rho_{\text{in}})$ and $\rho_2 = \rho_{\text{in}} + 0.55\,(\rho_{\text{out}} - \rho_{\text{in}})$. The two values ρ_{in} and ρ_{out} correspond to the grid boundaries. We use small values of $\{\kappa_1, \kappa_2\} \sim 10^{-4}$, so the scalar field is initially negligible compared to the black hole. In Fig. 3.1 we show some generic initial data profiles used to perturb the black hole.

We set the parameters $L = 1$, $q = 1$, $M = 0.12192$, and $Q = -0.169328$, which corresponds to a small black hole compared to the AdS length scale, since the radius of the black hole is $r_{\text{H}} = 0.2$, and 40% extremal with respect to the critical charge. Using the approximate instability criteria Eq. (3.13), the black hole should be stable under perturbations.

We start the simulation with a generic profile of the scalar field, following Eq. (3.14) as shown in Fig. 3.1, which impinges upon the black hole. We extract the scalar field at $\mathscr{I}$, that is the timelike boundary of AdS at infinity. After the initial pulse is scattered, the scalar field decays with its characteristic quasi-normal frequencies. This shows that the spacetime is settling towards a RNAdS black holes solution with a vanishing scalar

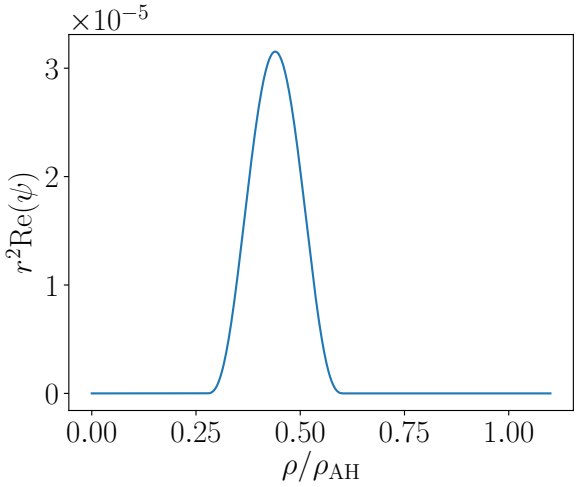

(a) $\kappa_1 = 10^{-4}$,$\kappa_2 = 0$, and $\kappa_3 = 0$

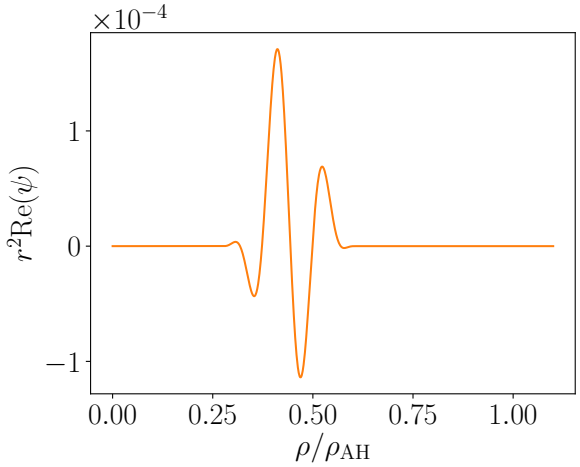

(b) $\kappa_1 = 10^{-4}$,$\kappa_2 = 5 \times 10^{-4}$, and $\kappa_3 = 10$

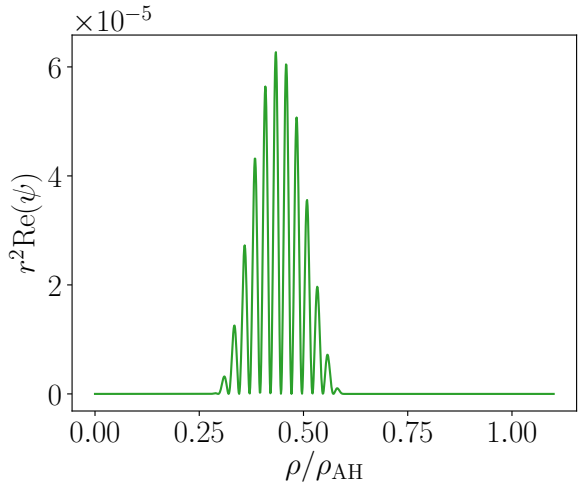

(c) $\kappa_1 = 10^{-4}$,$\kappa_2 = 10^{-4}$, and $\kappa_3 = 50$

Figure 3.1: Examples of different generic compact support initial data for the scalar field. By varying the parameters κ_1, κ_2 we verified that different initial configurations for the complex scalar field did not affect the features of the final solution provided the amplitude is small. The AdS boundary is at $\rho/\rho_{\text{AH}} = 0$, and the apparent horizon of the black hole is at $\rho/\rho_{\text{AH}} = 1$.

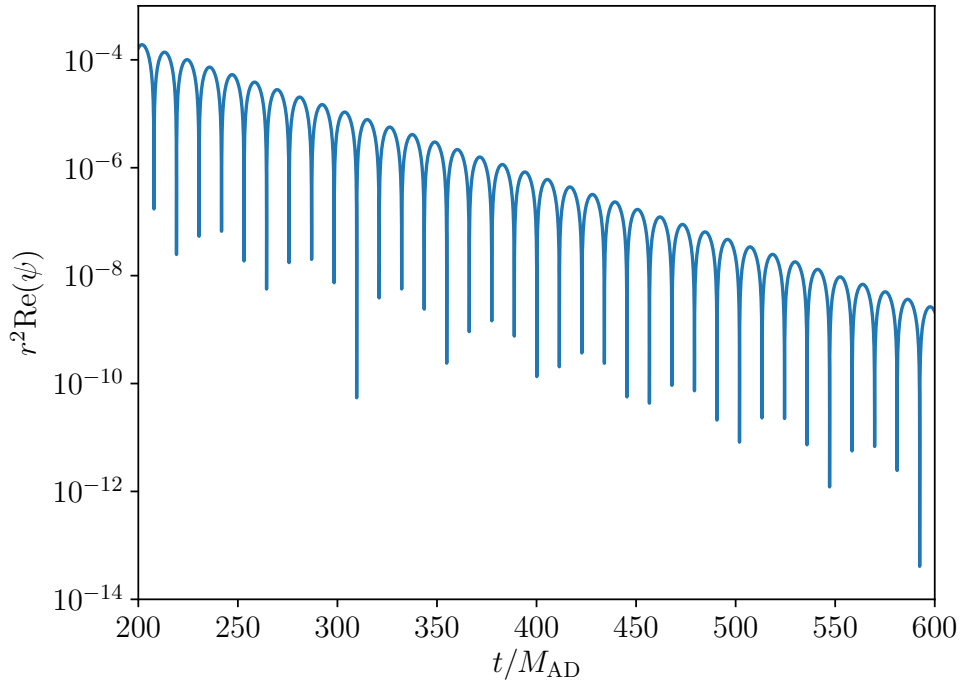

Figure 3.2: Quasi-normal ringdown of the scalar field at late times, extracted at $\mathscr{I}$. We set $L = 1$, $M = 0.12192$, $Q = -0.169328$, which corresponds to a 40% extremal black hole with $r_{\mathrm{H}} = 0.2$, and the gauge coupling is $q = 1.0$. We observe the presence of the fundamental mode with $\omega = 2.6702 - 0.27173i$, which matches the linear predictions very well [6]. The scalar field is decaying because the imaginary part of the frequency is negative.

field, confirming that the black hole is in fact stable against such perturbation with these parameters. Furthermore, this matches the linear prediction by [6], and we are able to reproduce the real and imaginary values of the fundamental frequency, $\omega_0 = 2.6702 - 0.27173i$, to very high accuracy (better than $\sim 0.02\%$). In Appendix A, in Tab. A.1 we show we are in very good agreement with the linear calculations for a number of different parameters.

We performed some extensive testing of the system in this linear regime, resulting in very good agreement with the linear calculations. However, most of those evolution lie in the stable regime of the system. To trigger the superradiant instability and evolve it into the nonlinear regime we need to find mode with a positive imaginary part of the frequency $\mathrm{Im}(\omega) > 0$. However, we will first find the onset of the instability, that is $\mathrm{Im}(\omega) \sim 0$, and compare with the linear calculations of [6].

3.3.2 Onset of the instability

The onset of the instability is identified when, for a given set of parameters, the imaginary part of the quasi-normal frequency vanishes. Parametrically varying the gauge coupling one can find a regime where the imaginary part of the frequency changes from negative, that is decaying, to a positive value. The positive value of the quasi-normal frequency tells us that the mode will undergo an exponential growth. We follow the procedure used in the linearized analysis where they find the onset on the instability for a different range of parameters, however, always staying within the small black hole regime $r_+/L \ll 1$.

For concreteness we will set the spacetime parameters as before, $L = 1$, $M = 0.17568$, and $Q = -0.33865$, however, we increase the value of the gauge coupling to $q = 2$. Guided by the instability criteria (3.13) we expect to see a growing mode developing. We used the three different types of initial data for the scalar field which, in turn, yielded the same type of evolution after the the initial profile is scattered. We show on Fig. 3.3 that the scalar field extracted at infinity; a growing mode is visible. We get that the imaginary part of the frequency of the mode is $\mathrm{Im}(\omega) = 1.555 \times 10^{-3}$, which matches the predicted value obtain through linear analysis by Uchikata and Yoshida [6].

We have identified the onset of the instability and established that it is independent of the initial data used. The frequency of the growing mode matches the value of the fundamental frequency computed at the linear level with $\mathrm{Re}(\omega) = 3.3620$ and $\mathrm{Im}(\omega) = 1.555 \times 10^{-3}$. However, given that the black hole area grew a negligible amount, of order $\sim 10^{-4}$, we have not yet reached the nonlinear regime to determine what the end state of the instability is. We will increase the gauge coupling q to investigate further the dynamics and elucidate the end state of the black hole.

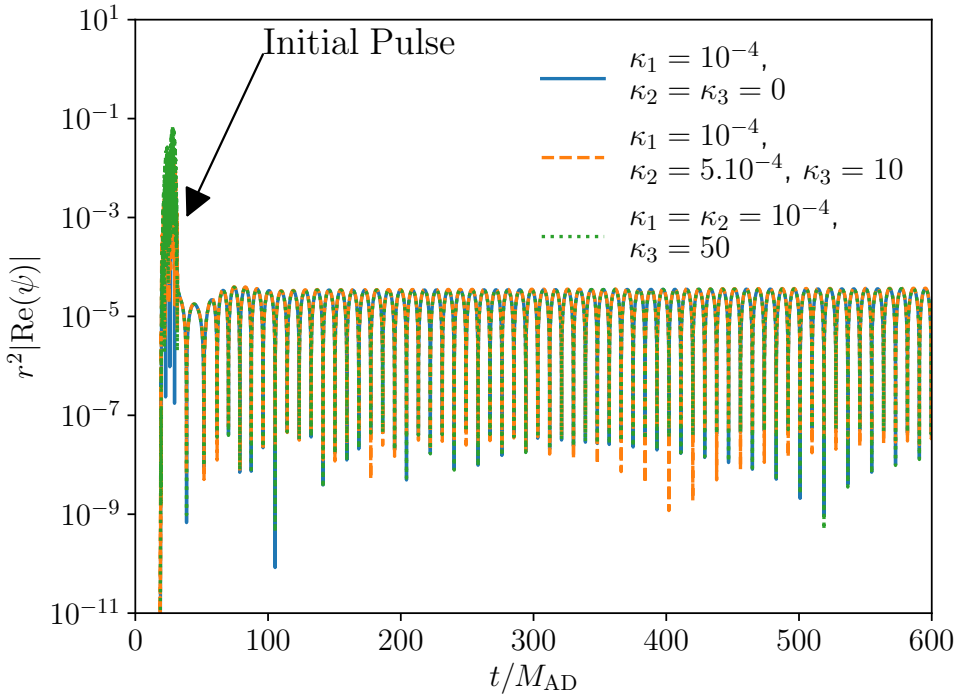

Figure 3.3: Onset of the superradiant instability. The figure shows the scalar field growing at a very small rate $\mathrm{Im}(\omega) = 1.555 \times 10^{-3}$, after the initial pulse is scattered. Three different configurations of the initial data are used, with colors matching Fig. 3.1. The late time evolution of the scalar field does not seem to depend on the initial data provided it has small amplitude.

3.4 Nonlinear Evolution

In the previous section we verified the decay rates and the onset of the instability predicted by linear theory, using an ingoing null formulation and the full nonlinear equations. In this section we push things further by evolving the system well into the nonlinear regime. We elucidate the end state of the superradiant instability, and characterize the stationary solution by the charge remaining in the black hole and the charge extracted by the scalar field. The superradiant instability, thus, reaches a saturation point and the extraction of energy stops. During the evolution of the system the cosmic censorship conjecture still holds.

We use different generic initial data with compact support to verify that the final state

is independent of it, albeit giving rise to slightly different dynamics. Having fixed M and Q we will vary parametrically the gauge coupling and compare the results for each of the cases. We track several gauge invariant quantities to better understand the underlying dynamics and we use a spectrogram to view the dynamics through a mode picture.

At early times, the growth rates match the prediction of [6] in the linearized case. At later times, the perturbation becomes nonlinear, as backreaction onto the black hole becomes significant, with the spacetime eventually settling into a stationary hairy black hole, that is with a non-trivial profile of the scalar field.

The superradiant cases display some general characteristics. The scalar field, at late times, saturates in amplitude and has a harmonic time dependence, resulting in a *time-independent* stress-energy tensor and metric. As the evolution takes place, significant amounts of charge, measured at the apparent horizon, are extracted from the black hole by the scalar field. More charge is extracted the larger the value of the gauge coupling q is. The irreducible mass of the black hole, which is proportional to the square root of the area, approaches that of the a Schwarzschild-AdS black hole of mass M for large values of q. The scalar hair is distributed farther away from the black hole for larger values of q. Lastly, the approach to the final state is less smooth for larger values of q.

In the following we will address these points in two stages. First we will look at the final state of the full nonlinear development of the superradiant instability, and its dependence, or lack thereof, on the initial data. Next we will focus on the dynamics of the superradiant instability. We will mainly turn our attention to gauge invariant quantities that we track, and to using a "mode perspective" on the evolution of the scalar field to show the mode dynamics.

3.4.1 End State of the Superradiant Instability

We fix $L = 1$, $M_{\rm AD} = 0.17568$, and $Q_{\rm AD} = -0.338656$, which corresponds to a small black hole compared to the AdS length scale, since $r_{\rm H} = 0.2$, with a charge of 80% of the critical value. We prescribe the initial profile of the scalar field as compact support pulse of the form Eq. (3.14), and perform the full nonlinear evolution of the system.

We show in Fig. 3.4 the typical behavior of the real part of the scalar field extracted at infinity, that is at the AdS boundary. We identify at early times the scattered initial perturbation, followed by a period of exponential growth of the field. During this growth period the scalar field extracts mass and charge from the black hole through superradiance. The exponential growth of the scalar field at early times is consistent with the linear calculations. The perturbation has a small amplitude such that the backreaction onto the

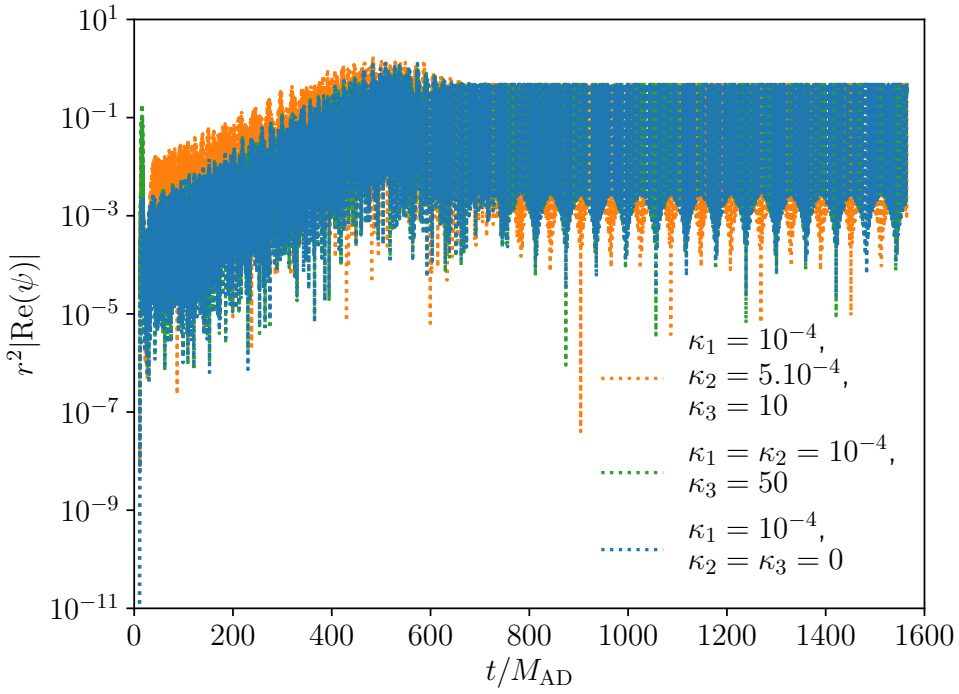

Figure 3.4: We follow the evolution of the real part of the scalar field $\mathrm{Re}(\psi)$, given different generic, compact support, initial data, as shown in Fig. 3.1, with $L = 1$, $M_{\mathrm{AD}} = 0.17568$, $Q_{\mathrm{AD}} = -0.338656$, and $q = 15$. At early times we identify the initial perturbing pulse. At intermediate times, the field grows exponentially, however, the field seems to contain more than one mode as the growing oscillations suggest. At late times, regardless of the initial data, and provided it is initially negligible compared to the black hole, the field settles into a single frequency mode with vanishing imaginary part. The real frequency of the field saturates the superradiance bound, and it is the same for all three initial data used.

spacetime remains small, we are in the "linear regime". As the scalar field's amplitude grows large the backreaction on the black hole becomes significant. Eventually, the growth of the scalar field reaches a plateau, where the imaginary part of the frequency vanishes, and the real part of the frequency saturates the superradiant condition Eq. 3.9. The spacetime settled into a stationary hairy black hole, where the "hair" refers to the non-trivial profile with harmonic time dependence of the scalar field. We show in Fig. 3.5, the charge transfer between the field and the black hole, and the area growth, respectively.

Focusing our attention on the black hole growth, in Fig. 3.5, we show the area of the apparent horizon normalized by the its initial value. The curve labeled by $q = 15$

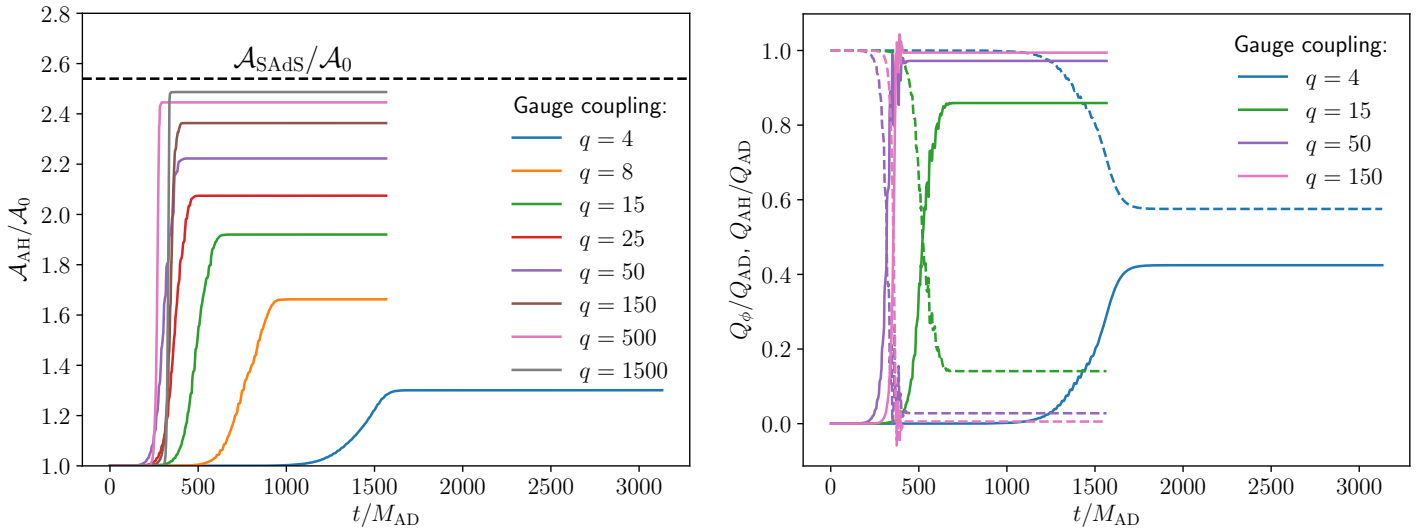

Figure 3.5: Dynamics of the area of the apparent horizon and the charge transfer. In these two figures we set $L = 1$, $M_{\rm AD} = 0.17568$, and $Q_{\rm AD} = 0.338656$. We show some representative values of the gauge coupling showcasing the difference between smaller and larger values. (Left:) Area growth of the apparent horizon $\mathcal{A}_{\rm AH}$ as a function of time for various choices of the gauge coupling q. The area has been normalized by the initial area of the apparent horizon, denoted by $\mathcal{A}_0$. The dashed line represents the normalized area of a Schwarzschild-AdS black hole with mass $M_{\rm AD}$. We observer, as q increases, the saturation value of $\mathcal{A}_{\rm AH}$ tends to $\mathcal{A}_{\rm SAdS}$. (Right:) Normalized charge as a function of time, for representative values of the gauge coupling q. The charge within the apparent horizon $Q_{\rm AH}$ is depicted with dashed lines, whereas the charge of the scalar field outside the apparent horizon, on a constant-v slice, is shown with solid lines.

corresponds to the apparent horizon dynamics related to the scalar field dynamics of Fig. 3.4. As expected from the area theorem, the area of the apparent horizon, that is the entropy, never decreases. For smaller values of the gauge coupling q, the growth of the apparent horizon has a very smooth approach to its final value, while for larger values of q, it displays some step-like behavior before reaching the plateau where the growth saturates. We observe that the larger the value of q the larger the increase in area, which is equivalent to an increase of the irreducible mass $M_{\rm irr}$ of the black hole. Furthermore, for large values of q the area of the apparent horizon tends to the value of the area of a Schwarzschild-AdS black holes $\mathcal{A}_{\rm SAdS}/\mathcal{A}_0 = 2.54$, shown in Fig. 3.5 with as a dashed line. Furthermore, in Fig. 3.6, we show the ratio of the irreducible mass $M_{\rm irr}$ to that of a Schwarzschild-AdS

black hole with same mass $M_{\rm AD}$ (and $Q_{\rm AD}=0$), at late times when the spacetime settles to a stationary regime, as a function of the gauge coupling q. We observer, again, that for larger values of q, the irreducible mass $M_{\rm irr}$ tends to the value for a SAdS black holes; in Fig. 3.6 that is $M_{\rm irr}/M_{\rm SAdS}\to 1$. For a value of $q=1680$ we have that $M_{\rm irr}/M_{\rm SAdS}\approx 99\%$.

We show in Fig. 3.5 the charge within the apparent horizon, and the integrated charge at each constant time surface and outside the apparent horizon. We will treat the former as the charge of the black hole, and latter as the charge of the scalar field; by charge conservation these two quantities sum to the charge at infinity $Q_{\rm AD}$. The charge displays richer dynamics than the area growth, including some "up-and-down" oscillations. Similar to the area growth, for lower values of q the approach to saturation is the smoothest. We find that at late times, for large values of q, nearly all of the charge is extracted from the black hole and transferred onto the scalar field. For $q=150$ roughly 99.4% of the charge is extracted from the black hole and transferred onto the scalar field, likewise for $q=1500$ nearly 99.6% of the charge is extracted.

We show the normalized Misner-Sharp mass $M_{\rm MS}(r)$, suitably defined to include the AdS curvature contribution [66], as a function of the radius in Fig. 3.7. This generalized Misner-Sharp quasi-local mass

$$M_{\rm MS}(r)=\frac{1}{2}\Sigma(v,r)\left(\frac{\Sigma(v,r)^2}{L^2}+1-g^{ab}\partial_a\Sigma(v,r)\partial_b\Sigma(v,r)\right) \tag{3.15}$$

converges to the global mass, in this case the Abbott-Deser mass $M_{\rm AD}$, and has the properties of being monotonic and positive. As q is increased, $M_{\rm MS}$ increases in value at the apparent horizon AH, located at small $r/M_{\rm AD}$. Hence, as q is increased less mass is extracted from the black hole by the scalar field. This contrast between the mass and the charge arise from the charge-to-mass ratio, Eq. (3.7), of the final state scalar field mode, which is larger for larger values of the gauge coupling q. Moreover, for large q, $M_{\rm MS}$ remains constant in r near the black hole, whereas for smaller values of q it has an evident radial dependence.

We turn our attention to the radial profile of the scalar field at late times, when the spacetime has reached a stationary state. We show the norm squared of the scalar field and rescaled by r^4, in Fig. 3.7. For lower values of the gauge coupling q, the scalar field condensate sits closer to the black holes, whereas for larger values of q it is localized farther away from the horizon. Additionally, from the previous discussion on Fig. 3.7, we observe that the condensates sitting closer to the horizon contain more mass. As q is increased and the scalar field sits farther out and contains less mass, which is in agreement with the larger mass-to-ratio, for larger values of q, of the final state scalar field mode.

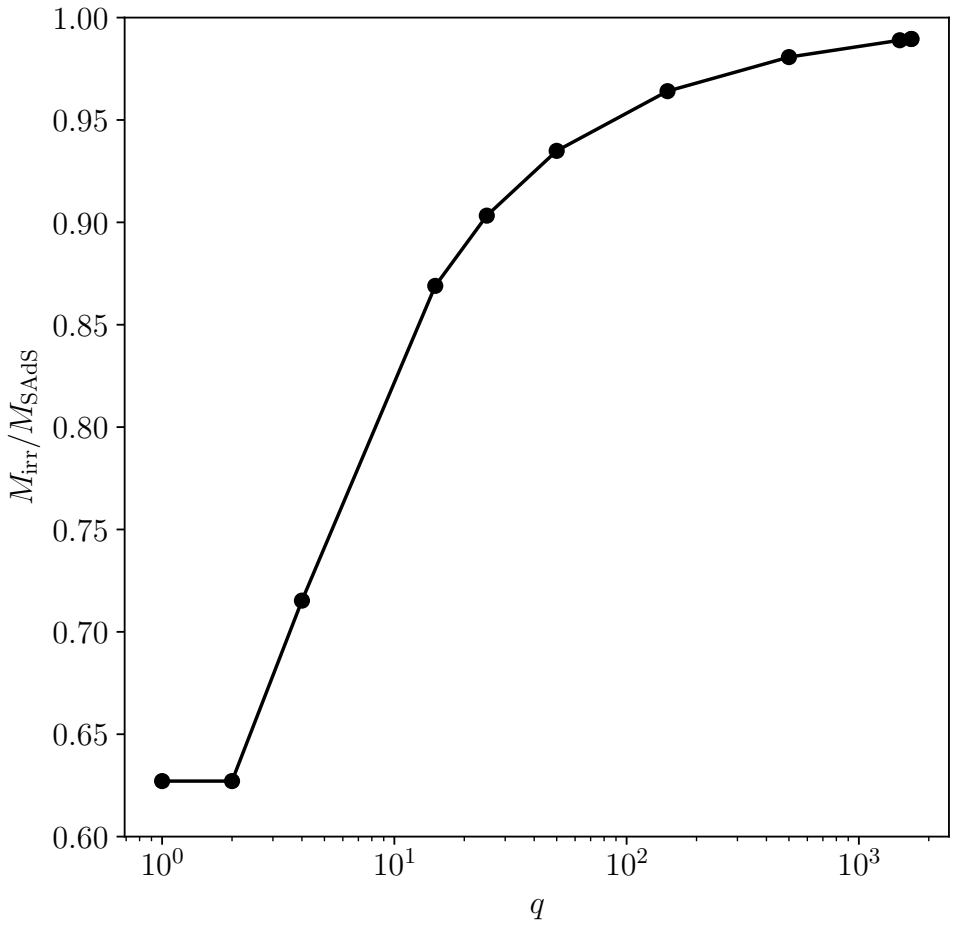

Figure 3.6: Normalized irreducible mass as a function of the gauge coupling q. As q is increased, $M_{\rm irr}/M_0 \to 1$. This is consistent with the claim that the final BH state for sufficiently large values of q is a Schwarzschild-AdS black hole of mass $M_{\rm AD}$ (the mass imposed at the boundary), surrounded by a distant high charge, low-mass scalar field condensate.

Combining the information of Figs. 3.4, 3.5, 3.6, and 3.7 we can fully describe the end state of the superradiant instability as a RN-AdS black hole surrounded by a harmonic time-dependent charged scalar field. For larger values of q, significant amounts of charge are extracted, with a low-mass scalar hair distributed farther away from the black hole, and with the black hole state being a (uncharged) Schwarzschild-AdS black hole of mass $M_{\rm AD}$. In particular, the scalar hair contains a single mode, the fundamental one, that saturates

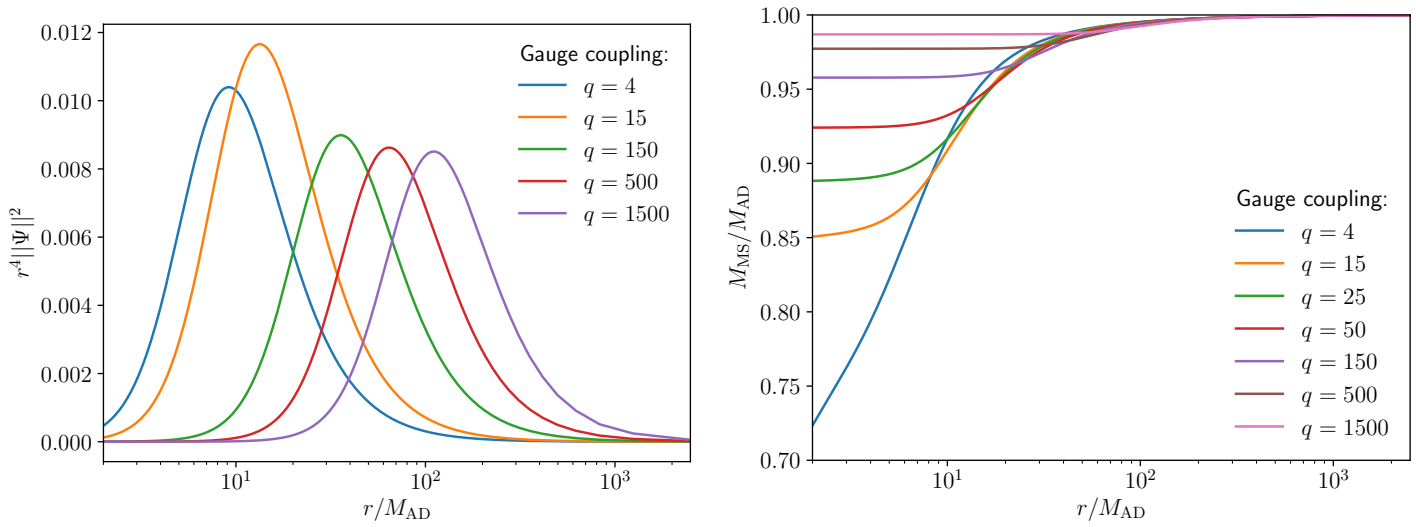

Figure 3.7: Late-time radial profiles of the scalar field and the measured generalized Misner-Sharp mass. In these two figures we set $L = 1$, $M_{\rm AD} = 0.17568$, and $Q_{\rm AD} = 0.338656$. We show some representative values of the gauge coupling showcasing the difference between smaller and larger values. (Left:) Norm squared and rescaled by r^4 of the scalar field at late times, that is when the spacetime reached a stationary state. The field is localized closer to the black hole for smaller values of q, whereas for larger values of q it condensates farther away from it. The rescaling of the norm squared of the scalar field comes from the redefinition of the field in Eq. (2.69). (Right:) Generalized Misner-Sharp mass as a function of the radius, Eq. (3.15), for representative values of q. These values of the mass have been measured at late times, when the spacetime has reached a stationary state. For large values of q, $M_{\rm MS}$ is constant up to a relatively large radial distance, indicating that the BH contains most of the mass and the scalar field hair lies far away from it. At larger radii the radial dependence arises because of the scalar field.

the (new) superradiant bound, after the backreaction has been taken into account.

We have successfully linked and described the linear regime of the perturbation with the end state of the fully nonlinear evolution of the superradiant instability of a RN-AdS black hole due to a complex scalar field perturbation. Moreover, we have robust evidence that the final state is independent of the initial perturbation, however, the dynamics of the exponential growth period are not. In what follows we will focus on the details of the growth dynamics to painting a unified and coherent picture of the whole process, tying together the linear regime, the strongly nonlinear dynamics, and final state of the instability.

3.4.2 Dynamics of the Superradiant Instability

We have successfully linked an initial perturbation to a stationary hairy black hole end state. Furthermore, we characterized the final state analyzing the profile of the scalar hair, the black hole mass and charge, as well as the distribution of mass at late times through the generalized Misner-Sharp mass. In this section, we will be focusing on the nonlinear dynamics that take place between the time in which the initial pulse perturbs the black hole up until the spacetime settles into a stationary hairy configuration.

To analyze the dynamics we make use of a spectrogram, decomposing the scalar field in its mode content and plotting in as a function of time. This will give an intuitive picture of the how the superradiant instability is acting on the system. In addition to the spectrogram, we will track, and overlay on Fig. 3.8, the superradiant bound, that is the right-hand-side of Eq. (3.9). Furthermore, we will compute the values of the quasinormal frequencies for the given set of parameters, using the continued fraction method described in Sec. 2.1.3, and compare them with the nonlinear evolution.

The less smooth behavior of the instability at large q, seen in Fig. 3.5, can be understood by studying the mode content. In Fig. 3.8 we show a spectrogram of an evolution, where we plot the frequency content of the scalar field as a function of time. This reveals the individual modes present in the scalar field, and their growth or decay rates as a function of time. The initial data contains a large number of modes, however, most of these modes do not satisfy the superradiant condition and decay rapidly, as we showed previously. The lower frequency modes that satisfy the superradiant instability condition, Eq. (3.9), are unstable. These exponentially growing modes are visible in the spectrogram, Fig. 3.8. In this representative example, nine unstable modes (dashed pink lines of Fig. 3.8) are visible, and can be seen to be below the superradiant bound (solid blue line of Fig. 3.8) at early times. In this case, the lower-Re(ω_n) modes have larger growth rates, Tab. 3.1. A striking feature is that the value of the imaginary part of the fundamental mode is not the largest, *i.e.* the fastest growing mode; the $n = 1$ and $n = 2$ overtones have larger values for the imaginary part of the frequency. This plays an important role in the mode dynamics, as can be seen from the spectrogram Fig. 3.8, where, over time, the unstable modes extract charge and mass from the black hole, and one by one (starting at large n) they begin to decay, and are re-absorbed by the black hole. As the modes are being re-absorbed, the superradiant bound oscillates back and forth, rendering the previously-stable modes unstable, again. This process continues until the black hole is discharged to the level where only the fundamental mode ($n = 0$) with zero growth rate is present, and the real part of its frequency saturates the superradiant instability condition Eq. 3.9. The fundamental mode of the scalar field remains as the condensate, described in the previous section.

n	ω
0	$6.6109 + 0.0720i$
1	$9.0368 + 0.0780i$
2	$11.1611 + 0.0757i$
3	$13.0737 + 0.0718i$
4	$14.8156 + 0.0674i$
5	$16.4046 + 0.0626i$
6	$17.8429 + 0.0572i$
7	$19.1146 + 0.0502i$
8	$20.1540 + 0.0220i$

Table 3.1: Quasinormal frequencies for $r_+ = 0.2$, $Q_{\rm AD}$ set to 80% of the extremal value, and $q = 12$. These modes are shown with a pink dashed line on Fig. 3.8. All of these modes satisfy the superradiant instability condition.

We can now understand the oscillations of Fig. 3.5 as the effect of having a mixture of modes, some of which are extracting energy, and other depositing, charge and mass into the black hole. In the end, the black hole reaches the hairy state, with all the higher mode having decayed. Indeed, when a value for q is chosen to be just above the instability threshold, only a single mode is present, giving rise to a very smooth evolution and approach to the stationary end state.

We have shown an intuitive picture of the behavior, at intermediate times, of individual modes as charge and mass are nonlinearly extracted from the black hole. We have identified that the less smooth behavior of system for large values of q depends heavily on the nontrivial mode dynamics that take place during the exponential growth period. The spectrogram show evidence for the harmonic dependence of the scalar field containing a single mode, specifically the fundamental mode with vanishing growth rate. In the end, through the dynamical evolution, we have linked the early times corresponding to the linear regime, the intermediate time involving complicated mode dynamics corresponding to the exponential growth of the modes, and the late times corresponding to the final stationary black hole state, confirming the expectations.

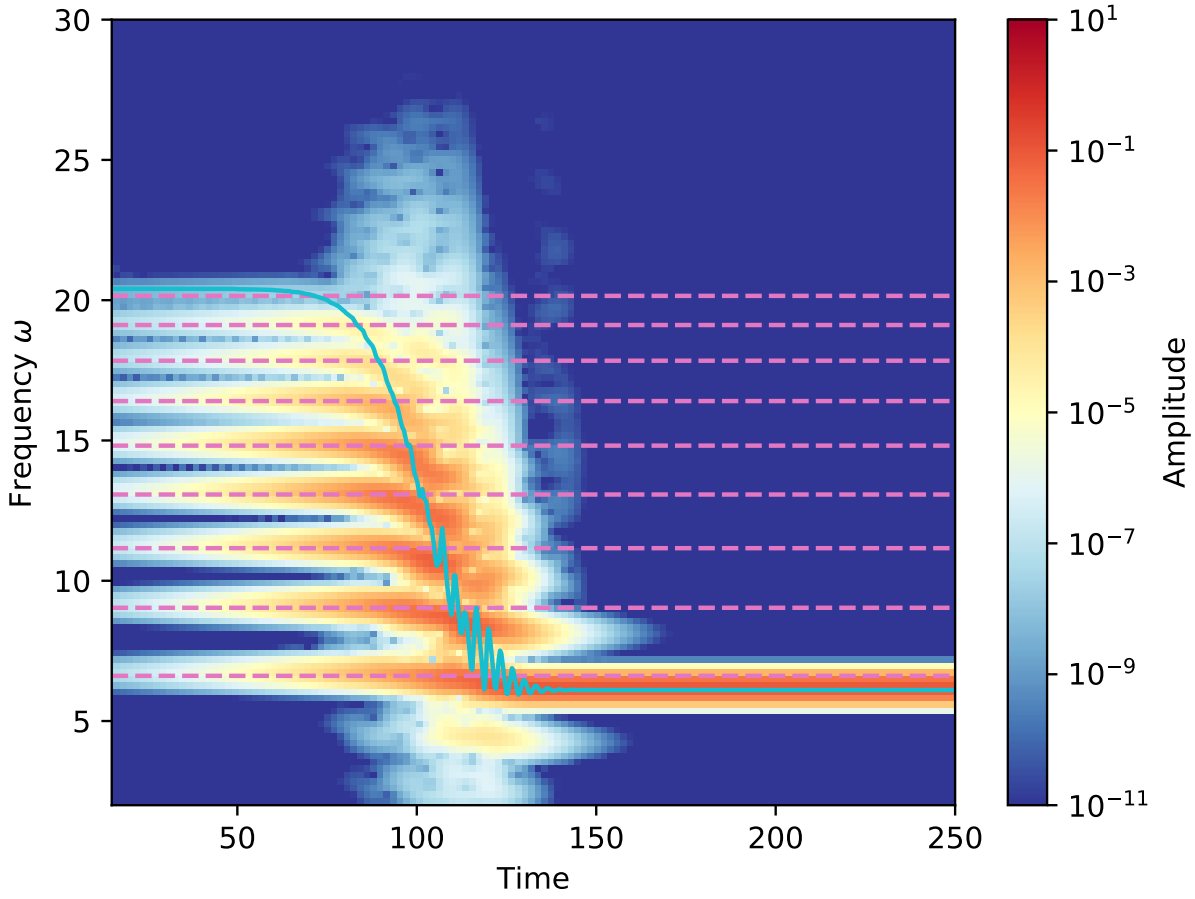

Figure 3.8: Spectrogram of $\mathrm{Re}(\varphi_3(v))$. This is computed by partitioning the time axis into intervals, and performing discrete Fourier transforms on these intervals. The intervals overlap, thus the starting point is offset. The case shown here has $q = 12$, $r_+ = 0.2$, and Q_{AD} set to 80% of the extremal value, that is $Q_{\mathrm{AD}} = -0.338656$, $M_{\mathrm{AD}} = 0.17586$, and we set $L = 1$. The colorscale shows the amplitude of the scalar field on a logarithmic scale. The vertical axis represents the real part of the frequency, and the horizontal axis shows the evolution over time. We overlay the values of the quasinormal frequencies present in the field, shown with pink dashed lines. Similarly, we overlay the dynamical value of the superradiant bound, RHS of Eq. (3.9), extracted from the numerical evolution of the system, shown in blue. At early times, the lowest eight modes grow exponentially, with faster growth rate for lower frequencies. As charge and mass is extracted, all modes , aside from the fundamental one, eventually start to decay, with higher frequencies decaying first. Consistent with the evolution of the superradiant bound, those higher frequencies cease to be superradiant as the instability evolves. The growth rate of the fundamental mode approaches zero, leaving a final static black hole with a harmonically oscillating scalar condensate.

3.5 Summary

We have shown the full nonlinear development of the charged superradiant instability for small Reissner-Nordstrom-anti de Sitter black holes. Initially, superradiant modes extract charge and mass from the black hole and grow exponentially [67, 6]. As this process unfolds the scalar field backreacts onto the black hole, effectively modifying the superradiant bound. Hence, the higher-frequency modes cease to be superradiant and fall back into the black hole, returning energy and charge, and resulting in nontrivial dynamics. Eventually, the fundamental mode remains as a condensate with zero growth rate. While nonlinear coupling between modes (via gravity and electromagnetism) can generate higher-frequency modes in AdS [64, 65], any such process would be overwhelmed by the fact that in the end, all modes beyond the fundamental are decaying. The ultimate fate of the charged superradiant instability in AdS is a stable hairy black hole, with the scalar condensate distributed far away from the black hole for large q.

Among the scalar modes, the final mode that remains maximizes the charge-to-mass ratio q/ω, and its growth corresponds to maximizing the entropy increase of the black hole. This observation may elucidate possible behavior of the superradiant instability in the rotating case. For a Kerr-AdS black hole, the stability criterion for a mode is Eq. (3.11), where m is the azimuthal number and $\Omega_{\rm H}$ is the angular frequency of the black hole [21]. We can see the two superradiant conditions, Eq. (3.9) and Eq. (3.11), are comparable with the key difference that for the charged case q is fixed parameter of the system, whereas in the rotating case m depends on the perturbation. In the rotating case, a given perturbation may be expected to spin down the black hole to the point where only the most superradiant mode remains, *i.e* that which causes the black hole to maximize its entropy, but this state will be just marginally stable, akin to a "black resonator" [62]. This supports the conjecture that that there is no stationary endpoint to the rotating superradiant instability in AdS. However, modes with increasing m continue to be excited and will keep developing.

The results presented in this chapter are consistent with results developed and published in a similar time frame by Sanchis-Gual, Degollado, Montero, Font & Herdeiro [68]. However, there are some differences and similarities worth pointing out. Their setup is similar to ours with the exception that they work in an asymptotically flat spacetime. Hence, they need to surround their Reissner-Nordstrom black hole by an artificial mirror. As we have mentioned before, any confining mechanism, whether a mirror, a mass term for the perturbing field, or the timelike AdS boundary, can give rise to the superradiant instability.

Similar to our result, they find that the end state of the superradiant instability is a stationary hairy black hole. However, the observation that the scalar hair is distributed far

away from the black hole highlights the difference between placing an artificial boundary at some location with respect to the black hole versus at the boundary of AdS. Working in AdS provides a natural setting free of ambiguities and potential sources of constraint violations. Additionally, they observed similar oscillations in the charged extracted from the black hole, but they identified them as a "bosenova" [69, 70], or explosion. The bosenova arises, instead, when axion self-interactions cause the collapse of the axion cloud. By adopting the mode picture for the scalar field we linked the oscillations to the nontrivial mode dynamics taking place; with all the modes eventually decaying and only supporting the fundamental mode with zero growth. Overall, the two results seem consistent with each other and the represent the first description of the end state of the charged superradiant instability.

In astrophysical applications, the outer potential barrier is no longer infinite, as in the AdS case, and it is instead typically provided by a mass term for the field [69, 71, 72]. Such a case provides a cutoff in the mode energy, and on the efficiency of the energy extraction. Moreover, a charged black hole in asymptotically flat spacetime is stable against the superradiant instability even when a mass term is added to the perturbing field [67]. Hence, without the possibility of analyzing a system bearing similarities to the astrophysically relevant problem, one would have to analyze the full development of the superradiant instability of a rotating black hole in asymptotically flat spacetime with a massive field acting as the perturbation.

In the next chapter we will focus on the behavior of a large RN-AdS black hole. We will show a unified picture of the different modes, and instabilities that can take place in the large black hole regime, and elucidate their end sates. We will explore the possibility of dynamically constructing excited hairy black holes and we will analyze the transitions between the excited levels.

Chapter 4

Excited Hairy Black Holes: Dynamical Construction and Level Transitions

4.1 Introduction

In the previous chapter we showed the full nonlinear development of the charged superradiant instability of a (charged) Reissner-Nordstrom-anti de Sitter black hole, in the small black hole regime $r_+/L \ll 1$. In general, the instability will be triggered by the modes in the pertubating field that satisfy the superradiant condition Eq. (3.9); growing exponentially at early times, and a intermediate times backreacting onto the black hole. We showed, by decomposition into modes of the perturbing field and using a spectrogram to plot them (Fig. 3.8), a complex dynamical behavior at intermediate times. The modes grow exponentially extracting mass and charge from the black hole, eventually backreacting onto the black hole and inducing a change of the superradiant bound. As the bound changes, the higher modes cease to be superradiant and fall back into the black hole, giving it back charge and mass. This process repeats itself for all the modes, one by one, until only the lowest frequency mode is present. At this point, the real part of the frequency of the fundamental mode saturates the superradiant bound, and the imaginary part of the frequency vanishes, thus, the exponential growth stops. Hence, the final state of the charged superradiant condition of small RN-AdS black holes is a stationary charged black hole with a non-trivial scalar hair profile with harmonic dependence. We showed that, with a fixed set of spacetime parameters $M_{\rm AD}$, $Q_{\rm AD}$, L, and q, the final state is independent of

the initial data.

The superradiant instability of black holes in AdS has mainly been studied in the small black hole regime [4, 22, 27, 61, 60, 73]. There has been significantly less attention to instabilities in the large black hole regime $r_+/L \gg 1$. An instability has been identified, however, in the near-horizon region of planar black holes in AdS [40, 29, 30], albeit in the context of the gauge/gravity duality. In particular, in the context of holographic superconductors, this near-horizon instability was identified for planar RN-AdS black holes, perturbed by a neutral or charged scalar field. Furthermore, numerical studies have explored to full nonlinear development of the near-horizon instability [31] and estbalished that the end state of the instability is a hairy black hole. The near-horizon instability has been identified for RN-AdS case with spherical topology in [37].

In this chapter we will explore the mode spectrum, in the linear regime, of spherical Reissner-Nordstrom-AdS black holes. We expect the near-horizon instability to be present in the large black hole regime. Moreover the superradiant instability has not been clearly identified in this limit, but we don't see a clear reason of why it should be suppressed. Furthermore, this linear analysis will clarify the presence and migration of modes in the small black hole regime with respect to the large black hole regime. Effectively, we will show the complete picture for the mode spectrum of RN-AdS black holes. Having identified the different families of modes, as well as the modes that can trigger instabilities, we will compute the full nonlinear evolution of perturbation containing these modes. Hence, we will show the existence and the full development of the superradiant instability in the large black hole regime, which was previously thought not to operate, elucidating its final state. Furthermore, we will compute the full nonlinear evolution of the near-horizon instability in the near-extremal regime, and show that the dynamics are largely similar to the ones found for the planar case. Finally, using the knowledge from the linear analysis, we will dynamically construct excited hairy black holes. These will represent marginally stable solutions that will transition dynamically between the different dominant modes present. With the perturbation sourcing lower overtones, the excited hairy black hole decays to the ground state.

4.2 General Motivation

Explorations of spacetime dynamics in general relativity have uncovered many surprising phenomena with theoretical and astrophysical implications. Examples include the discovery of critical phenomena [74, 75], spacetime turbulence [64, 76, 77, 78], and the black hole superradiant instability [79], the latter of which has been proposed as a probe of dark

matter [19, 80]. In recent years, the AdS/CFT correspondence has provided additional motivation for studying black holes in anti-de Sitter (AdS) spacetimes: black hole equilibration is believed to be holographically dual to thermalization of strongly coupled field theories, whereas instabilities describe phase transitions [29, 30].

One interesting theme is the explosion of black hole solutions when standard assumptions are relaxed. Black holes with "hair" (i.e., stationary black holes described by quantities other than the total mass, angular momentum, and electric charge) are generally forbidden as asymptotically-flat solutions to the Einstein-Maxwell system in four dimensions. But with additional fields, higher dimensions, or more general boundary conditions, the various theorems can be circumvented, and additional solutions with the same conserved quantities can emerge [81, 82]. For instance, in five dimensions, with one compactified dimension, there exist black string *and* black hole solutions. Generally, one of these solutions will be entropically preferred, and this often implies dynamical instability of the other solutions [83]. Indeed, if the compactified dimension is large compared to the black hole radius, then the black string is linearly unstable [84]. Nonlinearly, the string bifurcates self-similarly into a chain of black holes [85].

Black holes can have hair made up of additional fields if there is a confining mechanism to prevent dissipation. This occurs, for instance, in asymptotically AdS spacetimes, or for massive fields. One example is a charged planar AdS black hole in the presence of a charged scalar field: for sufficiently low temperature, there exist two stationary solutions, RN-AdS and a charged black hole with a scalar condensate. At these temperatures, RN-AdS is subject to the near-horizon scalar condensation instability [30], which leads to the hairy black hole under dynamical evolution [31]. For small RN-AdS, the superradiant instability also leads to a hairy black hole [1].

The hairy black holes obtained as end states of evolution in [31, 1] are in their *ground state.* In the superradiant case, the final black hole can be understood as an equilibrium combination of a small RNAdS black hole with the fundamental mode of a charged scalar field in global AdS [37]. However, the scalar field also has overtone solutions, and it is intriguing to ask whether these might also give rise to hairy black holes, now in their *excited state.*

The central result of this chapter is the dynamical construction of stationary *excited hairy black holes.* Our approach is to start with a fine-tuned perturbation of an unstable black hole that corresponds to an unstable overtone quasinormal mode. We evolve the instability numerically, and it eventually forms the excited hairy black hole. This black hole, is, however, unstable, and after some time decays to the ground state.

We take our initial black hole to be RNAdS, which is dynamically unstable to charged

scalars even in spherical symmetry. Although our end goal is the excited hairy black hole, we begin in Sec. 4.3 with a numerical study of RN-AdS massive charged scalar field quasinormal modes. Ultimately, we use the results of this analysis to construct the special initial data, but this section also constitutes a thorough analysis of the various modes of RNAdS throughout parameter space. Instabilities of RNAdS are usually studied using approximations that rely on the smallness of some parameter, either the black hole radius in the case of the superradiant instability, or the surface gravity for the near-horizon instability. We use the continued fraction method of Leaver [44], so our numerical analysis does not require these approximations.

Previous analyses have identified several mode families. For small black holes, RNAdS is "close" to global AdS, and therefore its spectrum contains quasinormal modes that are deformations of AdS normal modes. The normal-mode frequencies are evenly spaced along the real axis, so for sufficiently large gauge coupling q, they can be made to satisfy the superradiance condition, $0 < \mathrm{Re}\omega < qQ/r_+$. Modes satisfying this condition are amplified when they interact with the black hole, leading to instability [4].

Extremal RNAdS, meanwhile, has a near-horizon region with metric $\mathrm{AdS}_2 \times S^2$ [86]. This gives rise to an instability whenever the effective near-horizon mass of the scalar field lies below the Breitenlohner-Freedman (BF) bound [87] of the near-horizon region and the true mass is kept above the global BF bound [30]. This condition is most easily satisfied for large black holes in global AdS [37], and by continuity it also extends to near-extremal black holes [88, 89, 90].

In addition to the AdS modes, which can be superradiantly unstable, and the near-horizon mode, the spectrum of RNAdS also contains a collection of "zero-damped" modes. These modes are associated to the near-horizon region of near-extreme black holes, and indeed they are present also in the asymptotically flat case [91]. For small RNAdS they are described by a tower of evenly-spaced quasinormal frequencies extending below the real axis near the superradiant-bound frequency, with imaginary part proportional to the surface gravity. As extremality is approached, these merge into a branch point representing the horizon instability of Aretakis [92].

The interplay between superradiant and near-horizon instabilities was studied in [37], where it was shown that for small black holes, the near-horizon instability condition for a massless field becomes $q^2 > 1/(4r_+^2)$, so that it ceases to operate for fixed q as the black hole is made smaller. Conversely, the near-horizon instability does not require superradiance, as it will occur with $q = 0$ provided m^2 is sufficiently negative [89].

All of the modes above can be seen in our figures in Sec. 4.3.2. Our numerical results, however, provide further clarity on the nature of the near-horizon instability. We show by

varying the black hole size and the gauge coupling, that the zero-damped modes for small black holes migrate to become superradiantly unstable for large black holes. This family of modes has in fact many similarities to the small black hole AdS modes. Finally, we show that the leading unstable mode migrates to become the near-horizon unstable mode under suitable variation of parameters.

Although a dynamical instability can be identified through a linearized analysis, this cannot capture its complete time development. In Sec. 4.4 we present results of numerical simulations showing the full nonlinear development of the unstable modes of large RNAdS in spherical symmetry. In Sec. 4.4.2, we evolve generic initial perturbations, and observe a dynamical behavior similar to that observed in [1] for the small RNAdS superradiant instability: the modes extract charge and mass until the system settles to a final static black hole with a scalar condensate. For smaller gauge coupling, the final condensate lies closer to the black hole, similar to simulations of the near-horizon instability in the planar limit [31].

In Sec. 4.4.3, we construct the excited hairy black holes. We select parameters such that the corresponding large RNAdS solution has more than one unstable mode. Taking the quasinormal modes from the analysis of Sec. 4.3, we carefully perturb the background RNAdS solution with the first overtone mode, $n = 1$. We observe that under evolution the field extracts charge and mass until the mode saturates and superradiance stops. This time, however, the black hole is in an $n = 1$ excited state. This black hole appears to be a stationary solution, but it is in fact unstable to the fundamental $n = 0$ perturbation, since only the $n = 1$ mode saturated the superradiant bound. Because of small nonlinearities and numerical errors, we cannot avoid seeding this mode, albeit at much smaller amplitude. After some time, it grows and overtakes the $n = 1$ mode, and the black hole decays to the ground state.

As a final demonstration, we construct initial data consisting of *several* superradiant modes, such that the solution cascades through a series of unstable excited black hole equilibria corresponding to different overtones. A sample evolution is shown in figure 4.1.

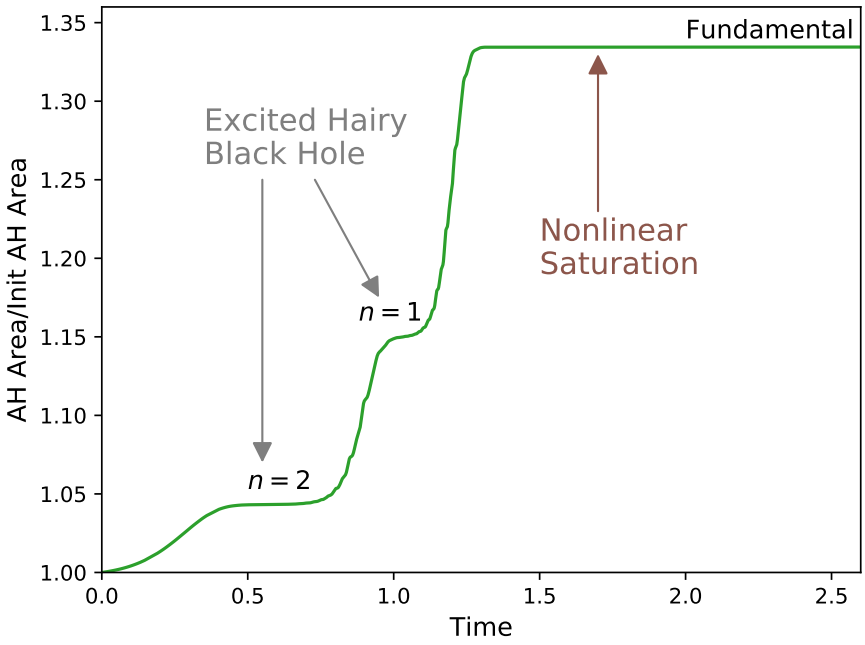

Figure 4.1: Apparent horizon area of a black hole as it undergoes a series of transitions through metastable excited hairy black hole states. Initial data chosen to consist primarily of $n = 2$ overtone, with subleading $n = 1$ overtone.

4.3 Linear perturbations

In this section we study the test scalar field (2.19). We begin in Sec. 4.3.1 by describing the mode families and instabilities that we expect to see in our numerics. In Sec. 2.1 we describe the continued fraction method for finding quasinormal frequencies numerically, and we present our results in Sec. 4.3.2.

4.3.1 Preliminaries

This section describes three families of modes that appear in the spectra we obtain in Sec. 4.3.2: the near-horizon mode, the AdS modes, and the zero-damped modes. These have all been derived analytically under various approximations elsewhere in the literature. We include them for completeness and for interpreting our numerical results in Sec. 4.3.2.

Near-horizon condensation instability

Four-dimensional extremal black holes with spherical horizon topology have near-horizon geometries closely related to $\mathrm{AdS}_2 \times S^2$ [86]; for extremal RNAdS, this correspondence becomes exact. The near-horizon instability is based on the violation of the BF bound of the near-horizon geometry by the scalar field. Holographically, the condensation corresponds to a temperature [30, 29].

To take the near-horizon limit it is useful to set the constant $C = Q/r_+$ in the Maxwell field, so that A_a vanishes on the horizon. For extremal RNAdS, we then have

$$ds^2_{\mathrm{ext}} = -f_{\mathrm{ext}} dt^2 + \frac{1}{f_{\mathrm{ext}}} dr^2 + r^2 d\Omega_2^2, \tag{4.1}$$

$$A_{\mathrm{ext}} = \frac{Q_{\mathrm{ext}}(r - r_+)}{r r_+} dt, \tag{4.2}$$

where

$$f_{\mathrm{ext}} = \frac{(r - r_+)^2}{L^2 r^2} \left[r^2 + 2 r_+ r + (L^2 + 3 r_+^2) \right]. \tag{4.3}$$

We then define a change of coordinates depending on a parameter $\lambda > 0$,

$$t = \frac{\tilde{t}}{\lambda}, \qquad r = r_+ + \lambda \tilde{r}. \tag{4.4}$$

Taking the $\lambda \to 0$ limit in these coordinates, we obtain the near-horizon fields,

$$ds^2_{\mathrm{NH}} = -\frac{\tilde{r}^2}{R^2} d\tilde{t}^2 + \frac{R^2}{\tilde{r}^2} d\tilde{r}^2 + r_+^2 d\Omega_2^2, \tag{4.5}$$

$$A_{\mathrm{NH}} = \frac{Q_{\mathrm{ext}} \tilde{r}}{r_+^2} d\tilde{t}, \tag{4.6}$$

where

$$\frac{1}{R^2} = \frac{6}{L^2} + \frac{1}{r_+^2}. \tag{4.7}$$

The metric (4.5) is recognized as $\mathrm{AdS}_2 \times S^2$ in Poincaré coordinates, where the AdS_2 factor has radius R. Note that the choice of C ensures that the Maxwell field remains finite in the near-horizon limit.

The scalar field acquires an effective mass in the near-horizon region. Taking the near-horizon limit of the Klein-Gordon equation (2.19), this is seen to be

$$\begin{aligned} m_{\text{eff}}^2 &= m^2 - \left.\frac{q^2 A_{0,\text{ext}}^2}{f_{\text{ext}}}\right|_{\lambda\to 0} \\ &= m^2 - q^2 \cdot \frac{L^2 + 3r_+^2}{L^2 + 6r_+^2}. \end{aligned} \tag{4.8}$$

In the large black hole limit, $m_{\text{eff}}^2 \to m^2 - q^2/2$. Instability can occur if m_{eff}^2 lies below the near-horizon BF bound,

$$m_{\text{NHBF}}^2 = -\frac{1}{4R^2} = -\frac{1}{4}\left(\frac{6}{L^2} + \frac{1}{r_+^2}\right), \tag{4.9}$$

which in the large black hole limit becomes $m_{\text{NHBF}}^2 \to -3/(2L^2)$. It was further shown using energy arguments that for large black holes this bound is sharp [93]. To be globally stable, it is necessary that the global BF bound be respected, i.e., $m^2 \geq -9/(4L^2)$. Thus, in the large black hole limit, the near-horizon instability is triggered if

$$-\frac{9}{4L^2} \leq m^2 < -\frac{3}{2L^2} + \frac{q^2}{2}, \tag{4.10}$$

which can be easily satisfied by choosing sufficiently large q^2 or negative m^2 (but not too negative). By continuity, the instability is expected to also occur for near-extreme black holes [29, 90].

For small black holes, it is not possible to trigger the near-horizon instability with negative m^2 since in this case the near-horizon BF bound is below the global BF bound. In addition, q^2 must be taken very large to obtain an instability, i.e.,

$$q^2 \geq \frac{1}{4r_+^2} + m^2. \tag{4.11}$$

For these reasons, the near-horizon instability is said to not operate for small black holes [37].

It should be noted that in the rest of the chapter we will set the gauge constant $C \to 0$, so mode frequencies pick up an additional shift $\Delta\omega = qC = qQ/r_+$. In that gauge, the near-horizon unstable mode frequency for near-extreme black holes will lie near the superradiant bound frequency, qQ/r_+.

Superradiant instability

In Sec. 3.2, we show the derivation of the superradiant condition from thermodynamic arguments [59]. The superradiant instability, or "black hole bomb", occurs when the superradiant scattering is combined with a confinement mechanism [79]. As we showed in the previous chapter, the AdS timelike boundary is a suitable confinement mechanism, and the system does display the superradiant instability.

With respect to the modes themselves, they are provided by the confinement mechanism, and for small RN-AdS black holes, there is a set of modes that are deformations of global AdS normal modes, which have frequencies,

$$\omega_n^{\pm} = \pm\frac{2n+3}{L}, \qquad n = 0, 1, 2, \ldots \tag{4.12}$$

We therefore expect instability for ω_n^+ with

$$2n \lesssim qQL/r_+ - 3. \tag{4.13}$$

By choosing q sufficiently large, this condition is easily satisfied, and the superradiant instability is triggered, as we have seen before.

Naively the superradiant condition Eq. (3.9) should still hold for large black holes, however, an approximate criterion similar to Eq. (4.13) might not exist. For large black holes we will explore the quasinormal mode spectrum which correspond to these superradiant modes. Given the nature of the large black hole limit, however, the modes will not be deformations of global AdS normal modes. We will find the connections between these different types of modes by studying the black hole spectra in the small regime and parametrically increasing the radius, tracking the modes as they move in the complex plane, and determine their nature.

Zero-damped modes

A final class of modes that is relevant to our analysis is associated to the near-horizon region of near-extremal black holes. These modes, which are present also for asymptotically flat black holes, can be viewed as trapped in the extended black hole throat region, with decay rate that goes to zero in the extremal limit. They are often referred to as "zero-damped" modes to distinguish them from Kerr-Newman modes with nonzero decay rate in this limit [94, 95]. We will use this terminology, although it should be kept in mind that the

zero-damped modes are not necessarily the longest lived modes for our asymptotically AdS black holes.

In the asymptotically flat case, the zero-damped modes were shown in [91] to fall into one of two families, *principal* or *supplementary*, depending on the charge coupling and angular mode number of the scalar field. (The terminology refers to the near-horizon $SO(2,1)$ representations in which these modes lie.) Using a matched asymptotic expansion, the quasinormal frequencies of asymptotically-flat RN in spherical symmetry can be shown [91] to be

$$\omega_n^{\mathrm{P}} = \frac{qQ}{r_+} + \kappa \left[qr_+ - i \left(\frac{1}{2} - \sqrt{\frac{1}{4} - (qr_+)^2} + n \right) + \eta r_+ \right] \tag{4.14}$$

and

$$\omega_n^{\mathrm{S}} = \frac{qQ}{r_+} + \kappa \left[qr_+ - i \left(\frac{1}{2} + \sqrt{\frac{1}{4} - (qr_+)^2} + n \right) \right], \tag{4.15}$$

where $n = 0, 1, 2, \ldots$ is the overtone number, κ is the surface gravity, and η is a small complex number. If the quantity under the square root is positive, then the supplementary family (4.15) applies, otherwise the principal family (4.14).

We see that both families consist of a κ-spaced tower of modes extending below the superradiant bound frequency. As $\kappa \to 0$ these modes converge to qQ/r_+, which becomes a branch point; this is associated to the horizon instability of Aretakis [91].

Notice that the quantity under the square root in (4.14)–(4.15) becomes negative when the near-horizon instability condition (4.11) is satisfied, i.e., the effective mass violates the near-horizon BF bound. The frequency (4.14) nevertheless does not correspond to an instability in asymptotically-flat RN, as the imaginary part remains negative. For small RNAdS, we expect[1] similar behavior, with small (r_+/L)-corrections to the quasinormal frequencies. For large RNAdS, however, we will show numerically in Sec. 4.3.2 that these modes can become unstable when the near-horizon BF bound is violated.

4.3.2 Results

We now present the mode spectra obtained numerically as we vary the black hole parameters, $\alpha \equiv Q/Q_{\mathrm{ext}}$ and r_+, and the field parameters, q and m. We fix $L = 1$.

[1] We thank P. Zimmerman for helpful discussions on this point.

To disentangle the various instabilities, in the small and the large black hole regimes, we use a numerical implementation of Leaver's method to compute the quasinormal modes and track their migration as we vary parametrically the size of the black hole r_+ and the gauge coupling q. Leaver's method relies on expanding the solution of the radial Klein-Gordon equation (2.21) as a power series, then obtaining a recursion relation for its coefficients. If the power series converges uniformly for a give frequency ω, then that value will correspond to a quasinormal frequency. Furthermore, the series converges uniformly if the continued fraction Eq. (2.33) converges. Finally, the values of the frequency ω that solve Eq. (2.34) are the quasinormal frequencies that we are interested in. This method is purely numerical, and does not provide the analytical intuition some other methods do. Using the properties of the modes, discussed in Sec. 4.3.1, we will identify the relevant modes.

Let us call the superradiant strip the region $\mathrm{Re}(\omega) \in (0, qQ/r_+)$; this is the region where, if present, the superradiantly unstable modes should lie. Other modes, however, might still lie within this region, and in general they will be unstable.

Small black hole

A typical quasinormal spectrum for small RNAdS is shown in left panel of Fig. 4.2. This shows two branches of modes: the vertical branch extending below the real axis is the supplementary branch (4.15) of zero-damped modes, and the horizontal branch is the family of AdS modes. The $n = 0$ positive-frequency AdS mode lies within the superradiant strip $0 < \mathrm{Re}\omega < qQ/r_+$, and is therefore superradiantly unstable; it lies above the real axis in the left panel of Fig. 4.2. Note that since the black hole is nonextremal, the "zero-damped" modes have nonzero decay rate, and are in fact less long-lived than the AdS modes.

For the stable AdS modes, we see that the decay rate is proportional to the distance from the superradiant strip. We have also verified that the separation between zero-damped modes is equal to κ: this is shown in the right panel of Fig. 4.2 This separation, although expected to hold only for small RNAdS, holds also for larger r_+. In the right panel of this figure, we plot the mean spacing $\delta = \langle \omega^{\mathrm{S}}_{n+1} - \omega^{\mathrm{S}}_{n} \rangle$ for $r_+ = 1$ and $q = 0$, as a function of the surface gravity κ. We observe that $\delta \to \kappa$ as $\kappa \to 0$, in agreement with [37].

We now study the influence of varying the field charge q on the spectrum; this is shown in Fig. 4.3. As q increases, so does the superradiant bound frequency, qQ/r_+. The tower of zero-damped mode frequencies remains tied to this frequency, and shifts to the right in the complex plane as well. The AdS modes also shift to the right, but more slowly than the superradiant bound frequency. As q is increased, the real part of the frequency of the modes drop below the superradiant bound and migrate towards a positive value of their

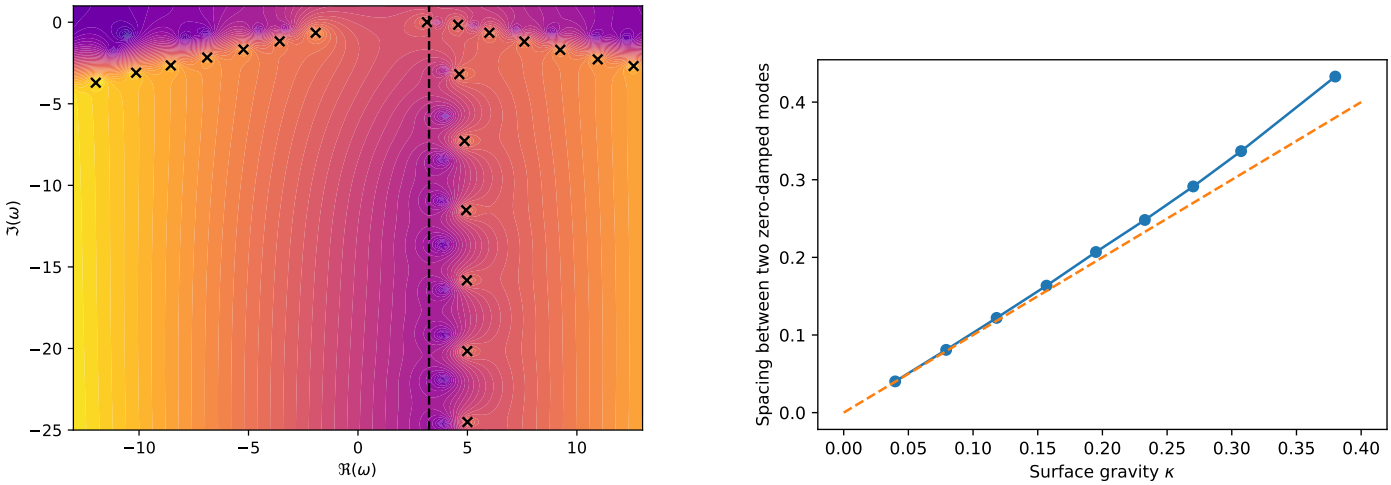

Figure 4.2: (Left:) Continued fraction values for RNAdS with $r_+ = 0.1$, $\alpha = 0.8$, $q = 4$, and $m = 0$. We plot the logarithm of the difference between the left hand side and right hand side of (2.34). Darker colors correspond to higher values. Quasinormal modes (minima in the plot) are marked by black crosses. We see that nonzero q breaks the symmetry between positive and negative real part. Two branches of modes are present, a vertical branch of zero-damped modes, and a more horizontal branch of AdS modes. The dashed vertical line corresponds to the superradiant bound frequency; modes satisfying $0 < \mathrm{Re}\omega < qQ/r_+$ are unstable. (Right:) Spacing δ between two zero-damped modes versus surface gravity κ. Here, we take $q = 0$ and $r_+ = 1$. We see that $\delta \to \kappa$ as $\kappa \to 0$.

imaginary frequencies. Hence, the modes satisfying these conditions become unstable. We show in Fig. 4.3 two distinct set of modes, the zero-damped modes and the deformations of the AdS modes. The former can be most easily identified in the $q = 0$ case were they lie on top of the superradiant bound. The latter, with $q = 0$, are seen as the diagonal branch with regular spacing between the modes. As q increases the zero-damped modes move along nearly horizontal trajectories getting increasingly closer to the AdS branch of modes. Furthermore, the lower frequency modes of the AdS branch become unstable, one by one, as the field charge is increased. This can be see clearly comparing the $q = 0$ case, in Fig. 4.3, and the $q = 12$ case; in the former all of the mode are stable. In contrast, in the latter the first four lower frequency modes drop below the superradiant bound and are unstable.

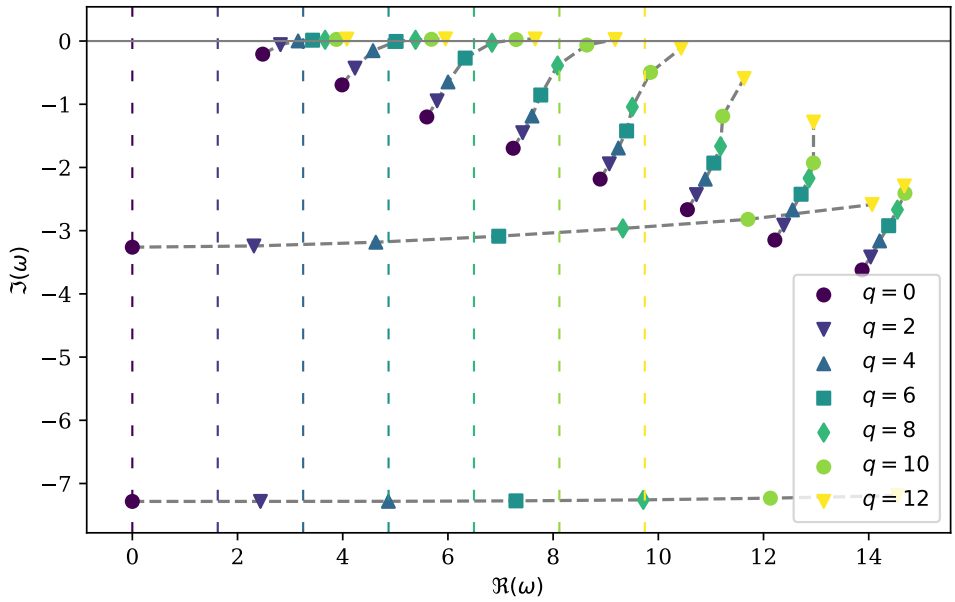

Figure 4.3: Quasinormal frequencies of RNAdS for $r_+ = 0.1$, $\alpha = 0.8$, $m = 0$, and $0 \leq q \leq 12$. Dashed gray curves track the quasinormal frequencies under variation of q. The two mostly-horizontal trajectories are zero-damped modes, and the others are AdS modes. The AdS modes become unstable when $\mathrm{Re}\,(\omega)$ drops below the superradiant bound frequency (indicated by dashed vertical lines) and pick up a positive $\mathrm{Im}\,(\omega)$.

Large black hole

The discussion of Sec. 4.3.1 indicates that for large RNAdS, we should see a near-horizon unstable mode and a tower of zero-damped modes. AdS modes, meanwhile, have been identified for small black holes, where they can be superradiantly unstable for appropriate values of q given a set of spacetime parameters $\{M,\ Q,\ L\}$. It is not clear in general, however, what role superradiance might play for large black holes, due to the lack of linear studies in this regime. The near-horizon instability, however, is well established in this limit.

To disentangle the different instabilities possibly present in the large black hole regime, we make use of the numerical procedure to compute the quasinormal frequencies. A typical large RNAdS spectrum is shown in the left panel of Fig. 4.4. This shows two diagonal branches of stable modes[2]and one unstable mode. We show in Fig. 4.4, with a represen-

[2]Note that one branch of stable modes has negative real frequency, $\mathrm{Re}\,(\omega) < 0$.

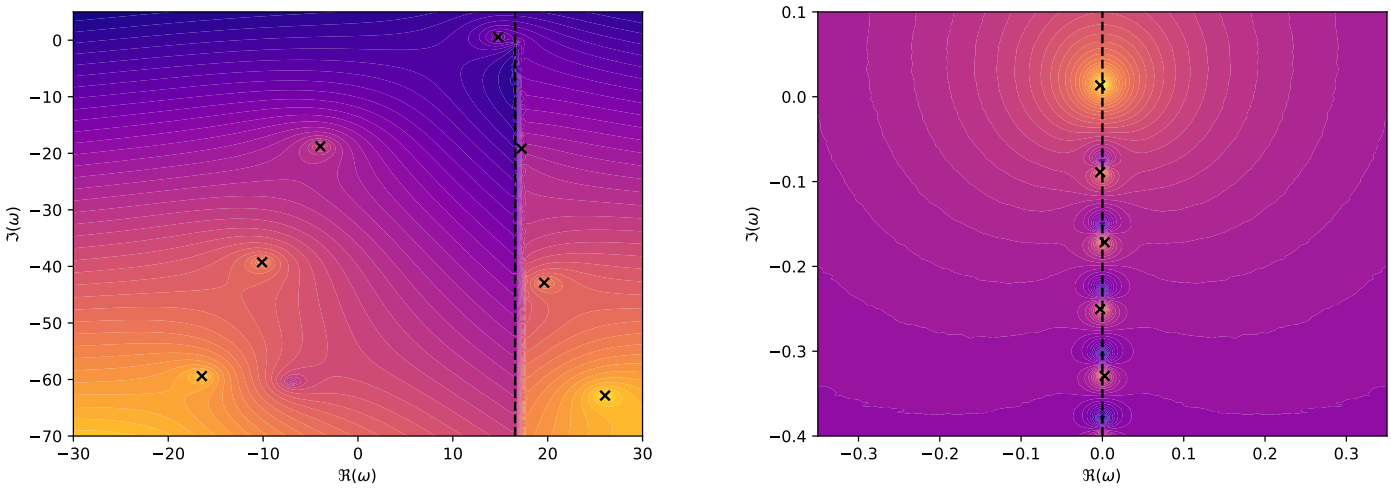

Figure 4.4: (Left:) Continued fraction values for RNAdS with $r_+ = 5.0$ and $\alpha = 0.95$, and field parameters $q = 2$, $m^2 = -1.49^2$. We see two diagonal branches, and one unstable mode. Not visible due to resolution is the set of zero-damped modes. (Right:) Quasinormal modes for $\alpha = 0.995$, $r_+ = 5$, $q = 0$ and $m^2 = -1.49^2$. The breaking of the BF bound gives rise to one unstable mode with $\mathrm{Re}(\omega) = 0$ and $\mathrm{Im}(\omega) > 0$. As the black hole is reaching extremality, we can also observe the piling of the zero-damped modes along the vertical axis, but with $\mathrm{Im}(\omega) < 0$. As extremality is reached, the spacing between the modes vanishes, and this tower of modes turns into a branch cut.

tative set of parameters, that the superradiance plays a role for large black holes, given that the unstable mode lies within the superradiant strip. Furthermore, we found, with our studies, that if an unstable mode exists it will lie within this superradiant strip. That is not to say that superradiance is the only process taking place when modes lie in this region; we find that the near-horizon and the superradiant instabilities coexist within this region.

Due to the resolution we are unable to display a tower of zero-damped modes that sit close to the superradiant bound, the vertical dashed line in the left panel of Fig. 4.4. Furthermore, these modes have a very close spacing which makes them hard to represent due to the scale of the vertical axis. The spacetime parameters are rather similar in both panels of Fig. 4.4, but the difference in the scale of the imaginary axis is relevant.

To isolate the near-horizon instability, we set $q = 0$, hence, turning off superradiance. In

the extremal case, the tachyonic instability can then be obtained with sufficiently negative m^2 such that

$$-\frac{9}{4L^2} \leq m^2 < -\frac{3}{2L^2}. \tag{4.16}$$

We choose $m^2 = -1.49^2$ to bring the mass squared close to the global BF bound, and we consider a near-extremal black hole with $\alpha = 0.995$. For these parameters, the quasinormal frequencies are shown in the right panel of Fig. 4.4. We show the presence of one unstable mode, directly above the the tower of zero-damped modes. The mode, however, can be discriminated as not being part of the zero-damped modes since it does not follow the regular spacing relationship with the rest of the modes. It certainly cannot be a superradiant mode since we forced it to be inactive by setting $q = 0$. Hence, the nature of the unstable mode is related to the breaking of the local BF bound and is a near-horizon mode. The mode lies close to real axis, and is, thus, unstable with a very long timescale. The near-horizon instability seems to trigger a single isolated unstable mode, as we have not been able to identify a second unstable mode by setting $q = 0$ and exploring the spacetimes parameters, such as the ones used for the right panel of Fig. 4.4.

We also show a tower of stable zero-damped modes in the right panel of Fig. 4.4. They are evenly spaced along the imaginary axis, whereas the near-horizon mode is separated by a larger distance, as mentioned before. The argument for the near-horizon mode is, strictly speaking, valid only for extremal black holes. As discussed in Sec. 4.3.1, we expect the instability to occur for near-extreme black holes by a continuity argument [37, 88, 89, 90]. Remarkably, as we decreased α, *i.e.* the extremality parameter of the black hole, the modes migrate into a single family. Indeed, all of the modes shifted downward increasing the space between each mode, and in particular the tachyonic mode drops below the real axis and positions itself at the top of the zero-damped family, with an even spacing. Thus, it seems that the near-horizon mode is the mode with largest $\mathrm{Im}(\omega)$, when the black hole is away from extremality. As the black hole tends towards extremality that mode detaches from the zero-damped tower of modes, becoming unstable in the process, and stops following the spacing properties of the other zero-damped modes.

We would now like to understand the connection between the modes of large and small RNAdS. To do so, we first track the mode frequencies as the size of the black hole is varied for $q = 0$. We shows the migration of several AdS modes and the leading zero-damped mode, as r_+ is varied between 0.1 and 5, in Fig. 4.5. We observe that the diagonal branches of the large black hole in Fig. 4.4 correspond to the AdS modes for small black holes. The importance of the different mode families seems to be reversed for small and large RNAdS: for large black holes, the zero-damped modes have slowest decay, whereas the AdS modes are longest lived in the small black hole case.

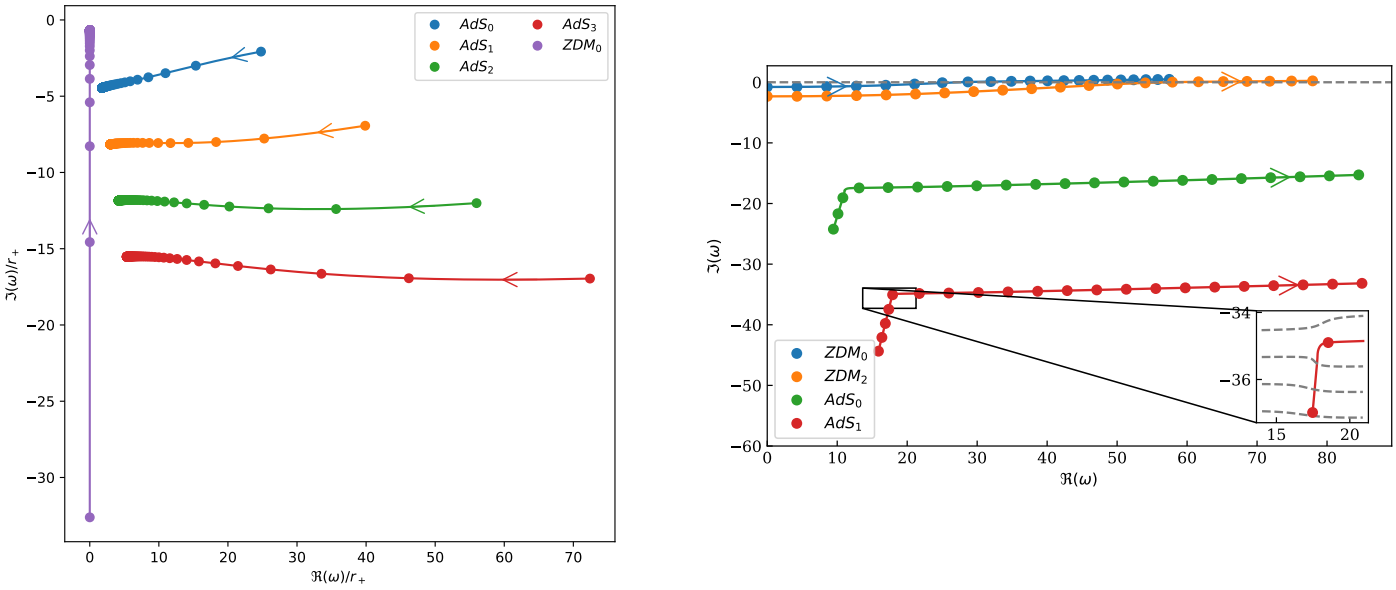

Figure 4.5: (Left:) Tracking of the first four AdS modes (AdS_i) and the first zero-damped mode (ZDM_0) for r_+ varied between 0.1 and 5 by steps of 0.05, for $\alpha = 0.8$, $q = 0$, and $m = 0$. On each trajectory, the arrow indicates the direction of increasing r_+. The trajectories approach a fixed point for large black holes, which arises as a consequence of a scaling symmetry: when $r_+ \gg L$, the modes are invariant under the transformation $r_+ \to \lambda r_+$, $r_- \to \lambda r_-$, $\omega \to \lambda\omega$. This can be derived from (2.21). We also find that whereas for small RNAdS, the AdS modes are longest lived, for large RNAdS the zero-damped modes are longest lived. (Right:) Quasinormal frequencies for a large black hole with $r_+ = 5$, $\alpha = 0.95$, $m = 0$, and q varying between 0 and 10 by steps of 0.5. In the main figure we plot trajectories for the first two zero-damped modes and the first two AdS modes, and the arrow indicates the direction of increasing q. We see that the zero-damped modes become unstable for large q. The AdS mode frequencies pass through a kink in their migration. The inset shows additional zero-damped mode trajectories (gray dashed), and illustrates how the second AdS mode slots itself in between two of them.

Next, we increase the gauge coupling q to connect the near-horizon mode to the general quasinormal spectrum of Fig. 4.4; results are presented in Fig. 4.5. We observe a very different behavior from the small black hole case of Fig. 4.3. First, the modes that become unstable are the *zero-damped modes*, not the AdS modes. This is not predicted by (4.15), which holds only for small black holes. Once unstable, zero-damped modes have a spectrum similar to the small black hole AdS-mode spectrum: the mode with smallest $\mathrm{Re}\omega$ has highest growth rate, and all unstable modes lie within the superradiant strip. Second, the AdS mode frequencies pass through a kink as they evolve; closer inspection reveals that they actually merge into the tower of zero-damped modes at large q.

Thus, the mode corresponding to the near-horizon instability is also the fastest growing mode in the case of a large black hole. For $q > 0$, this mode lies within the superradiant strip, so violation of the near-horizon BF bound and superradiance both contribute to its instability. This is not the case for a small black hole, where the fastest-growing mode is the first AdS mode, and instability occurs even when the near-horizon BF bound is satisfied.

To summarize, for small RNAdS, unstable modes come from the AdS branch, whereas for large RNAdS, they come from the zero-damped branch. When the near-horizon BF bound is violated for large black holes, the most unstable mode also exhibits near-horizon instability. Fig. 4.5 shows the crossover between the large and small black hole scenarios.

4.4 Nonlinear evolution

For our nonlinear studies, we solve the system of equations (2.6)–(2.10) numerically, with $m = 0$. As in the rest of the chapter and Chap. 3, we impose spherical symmetry and reflecting boundary conditions at infinity.

In the following subsection we give a quick description of the numerical method used, which we have described in detail in Chap. 2. We then describe the evolution for generic scalar field initial data in subsection 4.4.2 and the excited hairy black hole in subsection 4.4.3.

4.4.1 Method

We use the implementation describe in Chap. 2, and use the same numerical implementation as we used in [1]. This uses ingoing Eddington-Finkelstein coordinates (v, r), similar

to [55], but adapted to spherical symmetry. Equations are discretized with finite differences, using mixed second and fourth order radial derivative operators satisfying summation by parts (see, e.g., [57, 58]) and fourth order Runge-Kutta time stepping.

The spatial domain extends from an inner radius r_0, several grid points within the apparent horizon, to infinity. The singularity is thereby excised from the computational domain. To reach infinity, the domain is compactified by working with a spatial coordinate $\rho = 1/r$, and defining a uniform grid on the domain $0 \leq \rho \leq 1/r_0$.

Boundary data consist of the mass M, which agrees with the Abbott–Deser (AD) mass [56], and the charge Q; initial data are fully specified by the initial value of the scalar field, $\psi(v = 0)$. The system is solved by integrating radially inward along $v =$ constant null curves to obtain the remaining field values and their time derivatives; ψ is then integrated one step forward in time, and the procedure is iterated. With $\psi(v = 0) = 0$, this gives RN-AdS with mass M and charge Q as the solution, but more generally some of the mass and charge is contained in the scalar field. The characteristic formulation has some residual gauge freedom, which we use to set the Maxwell potential to vanish at infinity, and to set r to be the areal radius. We show the component form of the equations and the asymptotic conditions imposed at infinity in Chap. 2.

The scalar field can be expanded about infinity, and with the reflecting boundary condition, this takes the form Eq. (2.54). The quantity $\varphi_3(v)$ is an output of the simulation, and it contains information about the mode content of the solution. At each time v, we also compute the apparent horizon area $A_{\rm AH}$ and the distribution of charge between the black hole and the scalar field. The black hole charge $Q_{\rm AH}$ is evaluated as a flux integral of the electric field on the apparent horizon, and the field charge is integrated over the portion of the constant-v slice outside the apparent horizon. The sum of these two quantities is constant in time by charge conservation. To track the superradiant bound we extract the electrostatic potential at the apparent horizon $\Phi_{\rm AH}(v)$.

4.4.2 Generic evolution

We now study the evolution of large RNAdS black holes perturbed with generic scalar field configurations. We take the background solution to have $r_+ = 100$ and $\alpha \equiv Q/Q_{\rm ext} = 0.9$, fixing $L = 1$ throughout. Strictly speaking, we only have control over the mass M and the charge Q (which we impose as boundary data), but we take the initial scalar field to have very small amplitude, so to a good approximation these directly determine the background black hole parameters.

We take the scalar field initial data to be compactly supported outside the black hole, with profile $\psi(v=0) = (r^{-1} - r_1^{-1})^3 \, (r^{-1} - r_2^{-1})^3 \, (\kappa_1 + \kappa_2 \sin(10 r^{-1}))/r^2$ for $r_+ < r_1 \leq r \leq r_2 < \infty$, and zero otherwise. The observed dynamics are qualitatively similar to the small black hole superradiant instability [1]: when the black hole is unstable, charge and mass are extracted by the scalar field until a stationary hairy black hole final state is reached. The final state is, moreover, independent of the initial scalar field profile.

We experimented with varying the gauge coupling q; Fig. 4.6 shows the area of the apparent horizon as a function of time for several different values. For larger q, the final area is larger, and the growth in area happens over a much shorter time scale. Indeed, for the smallest value, $q = 4$, the area grows by just a few percent, whereas for larger values, $q > 200$, it more than doubles. Figs. 4.6 and 4.7 show the extraction of charge and the final radial profile of ψ, respectively. Indeed, the field has support closer to the black hole for the smaller values of q, consistent with the near-horizon instability [31]. For larger values of q, more charge is extracted, and the field has support further from the black hole. For very large q, nearly all the charge is extracted, and the final state is nearly Schwarzschild, with a scalar condensate far away. In all cases, the field profile has a single peak, so the condensate is in its ground state.

It is useful to examine also the dynamics of the boundary values of the scalar field, $\varphi_3(v)$. We present a time-frequency analysis in Fig. 4.8 for the $q = 24$ case. The peaks correspond to quasinormal modes, and we see that at early times, there are nine unstable modes, with the fastest growth rate for the lowest frequency. As mass and charge are extracted, however, the superradiant bound frequency decreases, and the higher frequency modes begin to decay (cf. Fig. 4.3). Eventually only the fundamental $n = 0$ mode remains. The final state is reached when the superradiant bound frequency matches the $n = 0$ mode frequency, so that this mode becomes marginally stable. Notice the shift in the $n = 0$ mode frequency over a very short time period just before saturation; this occurs because the background solution evolves very rapidly just before saturation, as seen in Fig. 4.6.

4.4.3 Excited hairy black hole

Initial data

We have seen in the previous subsection that the final state for generic initial data always corresponds to the fundamental superradiant mode, even in the case where multiple unstable modes are present. In all cases examined, the growth rate of individual modes decreases with increasing overtone number n; the fundamental mode grows fastest, as seen

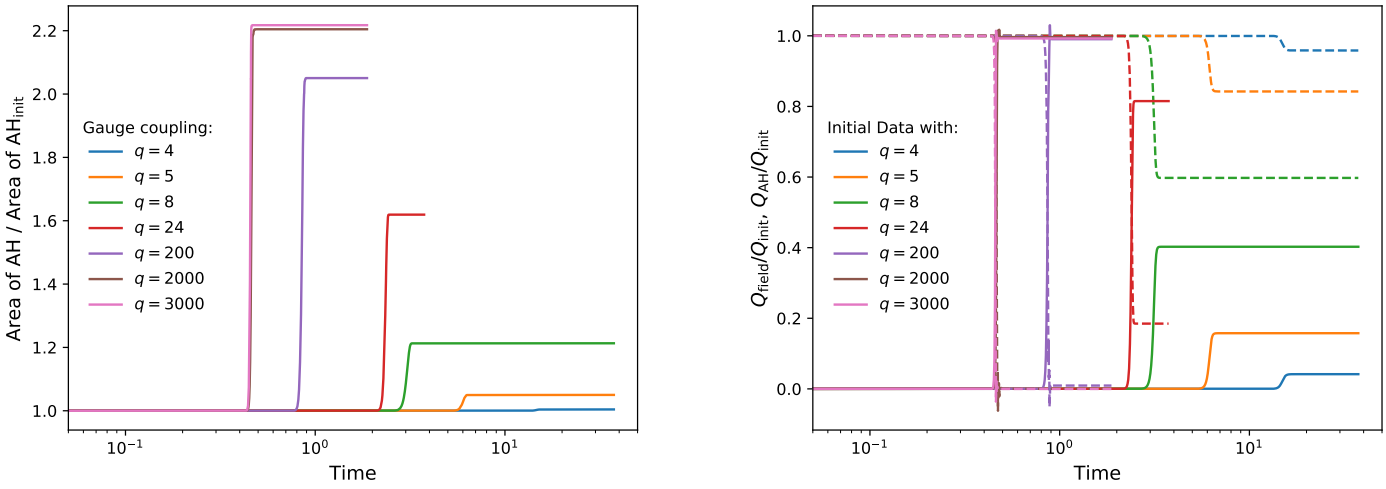

Figure 4.6: (Left:) Normalized area of the apparent horizon as a function of time, for initial black hole with $r_+ = 100$ and $\alpha = 0.9$. Different colors correspond to different gauge coupling q. (Right:) Normalized charge contained in the black hole and in the scalar field as a function of time, for initial black hole with $r_+ = 100$ and $\alpha = 0.9$. Solid curves denote scalar field charge outside the apparent horizon, and dashed curves denote charge within the black hole apparent horizon.

in Table 4.1. For *generic* initial data—with many modes initially excited—the evolution, after possibly complicated dynamics, always comes to be dominated by the fundamental mode.

Nevertheless, for *special* initial data—with overtone modes excited to higher amplitude—the evolution could be dominated (at least for some time) by $n > 0$ modes. If this time is longer than the saturation time for the overtone instability, then the system will reach the excited hairy black hole equilibrium.

To obtain suitable initial data, we require precise overtone mode functions. To obtain these, we first select parameters r_+, Q and q such that the background RN-AdS solution has multiple unstable modes, and then we use the method of Sec. 2.1 to calculate precise quasinormal frequencies. We then use the form of the radial equation, derived in Chap. 2, Eq. (2.37) which is in ingoing Eddington-Finklestein coordinates, and for each desired overtone we integrate this ODE numerically, with reflecting boundary conditions at the AdS boundary. We use this mode as initial data at the advanced time $v = 0$.

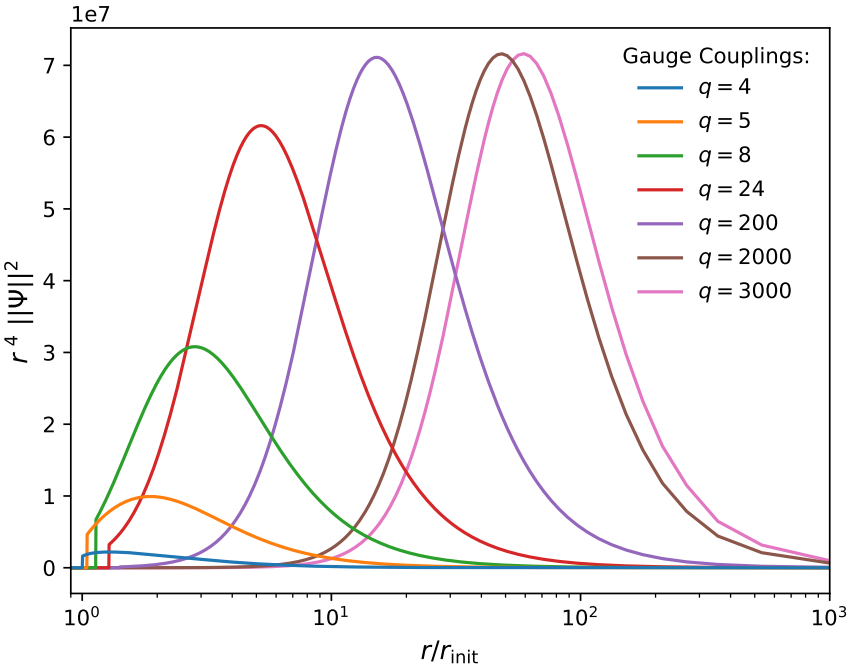

Figure 4.7: End state radial profile of the scalar field, for initial black hole with $r_+ = 100$ and $\alpha = 0.9$. For smaller gauge coupling q the field has support closer to the horizon, whereas for larger q the support is away from the black hole.

We consider two types of special initial data. The first consists of a single overtone mode ψ_n, which, if pure enough, we expect to evolve into an excited hairy black hole. The second type of initial data is a mixture of two modes, i.e.,

$$\psi_{\text{mix}} = a_{\text{mix}}\psi_2 + (1 - a_{\text{mix}})\psi_1, \tag{4.17}$$

with, e.g., $a_{\text{mix}} = 0.999$, and the amplitudes normalized using the infinity norm. With these data, we hope to achieve a cascade, where initially a $n = 2$ excited black hole forms, which then decays to $n = 1$, and then $n = 0$. Some initial data profiles are shown in Fig. 4.9.

Results

As in the generic evolution, we fix $r_+ = 100$, $\alpha \equiv Q/Q_{\text{ext}} = 0.9$, and $L = 1$. We then consider two cases for the scalar field charge, $q = 8, 11$. The significance of these latter

n	ω
0	$1780.01 + 17.29i$
1	$2277.33 + 16.59i$
2	$2655.28 + 14.29i$
3	$2952.42 + 11.97i$
4	$3188.37 + 9.83i$
5	$3374.87 + 7.89i$
6	$3519.76 + 6.15i$
7	$3628.68 + 4.55i$
8	$3705.19 + 3.00i$

Table 4.1: Quasinormal frequencies for $r_+ = 100$, $\alpha = 0.9$, and $q = 24$. The superradiant bound frequency is $q\Phi_{\rm H} = 3741.29$, from Eq. (3.9). The growth rate $\mathrm{Im}(\omega)$ decreases as the overtone number n grows.

two choices is that for $q = 8$, the background RNAdS solution has two unstable modes, whereas for $q = 11$, there are three unstable modes.

q=8: In this case, modes $n = 0, 1$ are unstable, with initial quasinormal frequencies $\omega_0 = 978.70 + 7.34i$ and $\omega_1 = 1168.69 + 4.79i$. To obtain the $n = 1$ excited hairy black hole, we take initial data to consist of ψ_1. We find that under evolution, the mode grows exponentially and extracts charge and mass from the black hole, similar to the generic evolution. This causes the superradiant bound frequency, $q\Phi_{\rm H}$, to drop until it matches $\mathrm{Re}\omega_1$. (The mode frequency $\mathrm{Re}\omega_1$ evolves due to the changing background spacetime, but this is negligible compared to the change in superradiant bound frequency.) At this point, superradiance stops, and the system settles into the excited hairy black hole state. The black hole is static, with the scalar field oscillating harmonically.

The area of the apparent horizon is shown in Fig. 4.10 (either one of the dashed curves). The excited hairy black hole is seen as a plateau, where the area stops growing because the scalar field is no longer extracting mass and charge. To this point, the description parallels that of Sec. 4.4.2. However, after some time, the area begins to grow *again*; this is because the $n = 0$ mode was present and growing the entire time. Indeed, since $\mathrm{Re}\omega_0 < \mathrm{Re}\omega_1$, the fundamental mode remains superradiantly unstable even after the overtone saturates. When the amplitude of the $n = 0$ mode becomes large, it disrupts the static black hole and causes its area to grow significantly. Once $q\Phi_{\rm H}$ drops below $\mathrm{Re}\omega_1$, the overtone mode falls back into the black hole, and once it reaches $\mathrm{Re}\omega_0$, superradiance stops completely.

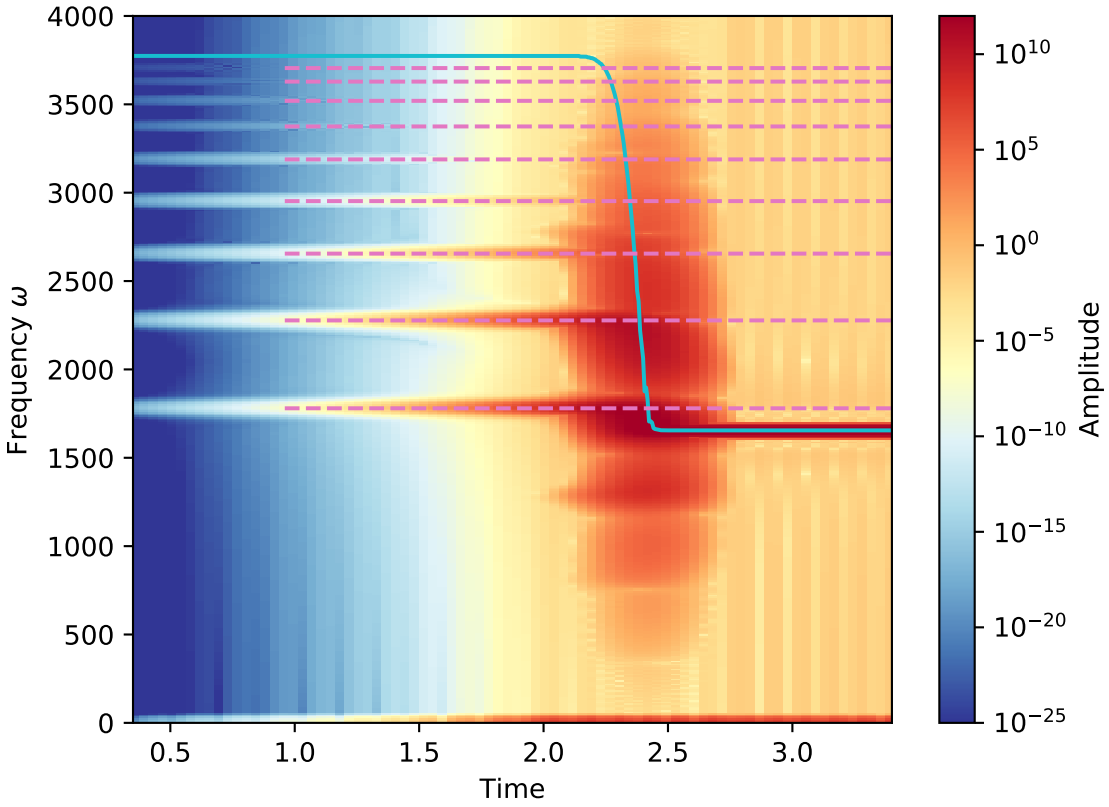

Figure 4.8: Spectrogram of $\mathrm{Re}\,(\varphi_3(v))$ for evolution starting from $r_+ = 100$, $\alpha = 0.9$, $L = 1$, and $q = 24$. Initially there are nine unstable modes; in the end, the final state is in the fundamental mode. Dashed lines correspond to the quasinormal frequencies of Table 4.1, solid to the superradiant bound frequency, $q\Phi_{\mathrm{AH}}(v)$.

At this point, the black hole is in its final state, described by the $n = 0$ ground state mode.

It is impossible to avoid triggering the $n = 0$ mode. At the initial time, the data for ψ_1 will always have numerical error, which will have some overlap with ψ_0. Moreover, during evolution, ψ_0 will be excited nonlinearly. To determine the origin of the observed $n = 0$ mode, we varied the initial perturbation amplitude, and read off the times t_1 and t_0 at which the $n = 1$ mode saturates and the $n = 0$ mode overtakes the dynamics, respectively.

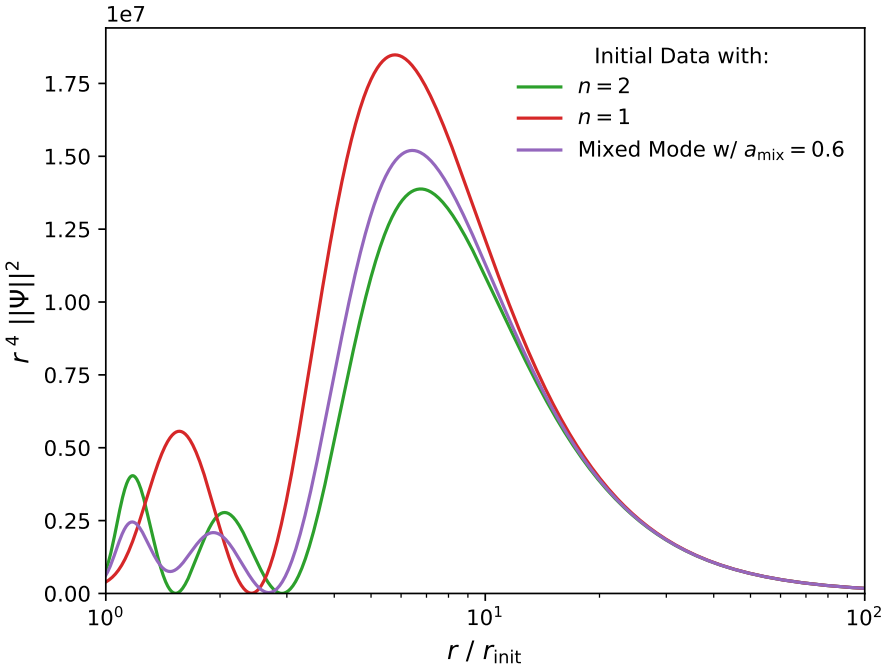

Figure 4.9: Radial profiles of initial data for initial values $r_+ = 100$, $\alpha = 0.9$, and $q = 11$. Two curves correspond to single-mode data, and the third to mixed-mode data.

Using the growth rates from the linear analysis we know that

$$\log\left(\frac{A_1}{A_0}\right) = t_0 \mathrm{Im}\omega_0 - t_1 \mathrm{Im}\omega_1 \,, \tag{4.18}$$

where A_1 and A_0 are the initial amplitudes respectively. We used this formula to calculate the amplitude A_0, given A_1 and the measured t_0, t_1.

For sufficiently small A_1, the calculated A_0 has only a mild dependence on A_1 indicating the zero mode is sourced primarily by truncation. (This was confirmed by noting the onset of this behavior depends on the resolution, with finer resolutions showing such behavior at smaller values of A_1.) However, for $A_1 \gtrsim 5 \times 10^{-3}$, we found that

$$A_0 \sim {A_1}^{2.75 \pm 0.07}, \tag{4.19}$$

This value is consistent with the seed arising from the self-gravitating contribution of the scalar field ($A_0 \propto {A_1}^3$).

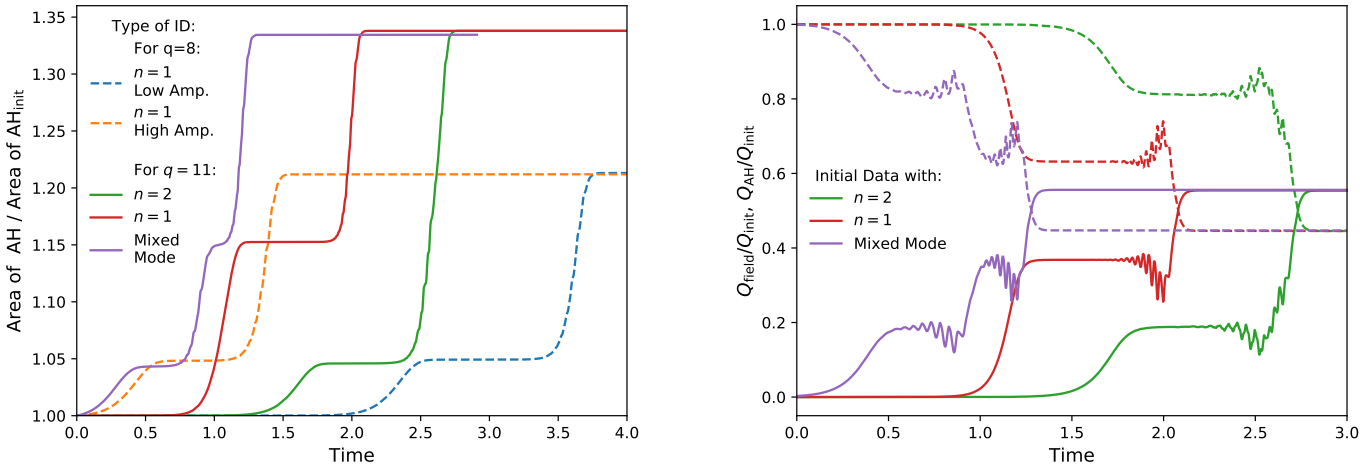

Figure 4.10: (Left:) Normalized area of the apparent horizon for initial $r_+ = 100$ and $\alpha = 0.9$. Dashed curves correspond to $q = 8$, solid to $q = 11$. Excited hairy black hole solutions occur at the temporary plateaus. (Right:) Charge transfer as a function of time for initial data with $r_+ = 100$, $\alpha = 0.9$, and $q = 11$. Solid curves are the (normalized) charge of the scalar field, dashed curves the charge of the black hole, that is the charge within the apparent horizon.

Evolutions with "low" and "high" initial perturbation amplitudes are depicted in Fig. 4.10. Notice that although the saturation times differ between the two cases, the areas of the hairy black holes are largely independent of the amplitude of the initial data, as long as the amplitude is low.

q=11: For $q = 11$, modes $n = 0, 1, 2$ are unstable, with frequencies $\omega_0 = 1174.13 + 9.94i$, $\omega_1 = 1448.56 + 8.06i$, and $\omega_2 = 1615.34 + 5.20i$. We therefore consider three types of initial data, data with modes $n = 1$ and $n = 2$ individually excited, and the mixed-mode initial data (4.17). Simulation results for the apparent horizon area are shown as solid curves in Fig. 4.10.

The behavior for single-mode initial data is qualitatively similar to $q = 8$. We find, however, that the area of the $n = 1$ excited hairy black hole is larger than the $n = 2$ black hole, consistent with the discussion above and $\mathrm{Re}\omega_1 < \mathrm{Re}\omega_2$. The final black hole is the same in both single-mode cases. In Fig. 4.10, right panel, we plot the electric charge of the black hole and the scalar field. This shows that at the end of the excited hairy black hole life, significant amounts of charge are deposited back into the hole. This corresponds to the

rapid decay of overtone hair as the superradiant bound frequency drops below the overtone frequency (cf. Fig. 4.4, where quasinormal mode decay time scales are much shorter than growth time scales).

For mixed-mode initial data, we take mixing ratio $a_{\rm mix} = 0.999$, i.e., the data are 99.9% $n = 2$ and 0.1% $n = 1$. This allows the $n = 2$ mode to dominate the dynamics for early times. The length of time the $n = 2$ will dominate can be estimated, using a similar calculation to (4.18), to be $\Delta t = (\log(a_{\rm mix}/(1 - a_{\rm mix})) + t_{\rm s}({\rm Im}\omega_2 - {\rm Im}\omega_1))/{\rm Im}\omega_1 \sim 0.66$, where $t_{\rm s}$ is the time at which the $n = 2$ mode saturates. Indeed, we observe (purple solid curve in Fig. 4.10) that the system cascades through *two* transient excited hairy black hole states, first $n = 2$, then $n = 1$, before settling in the ground state. The hairy black hole states match those seen in the single-mode evolutions.

We present a spectrogram for the mixed-mode evolution in Fig. 4.11. This shows a clear progression through the three unstable modes. Notice again that the final $n = 0$ oscillation frequency is slightly lower than the frequency of the initial $n = 0$ quasinormal mode. This shift arises because the final black hole is different from the initial one, and the superradiant bound frequency has shifted.

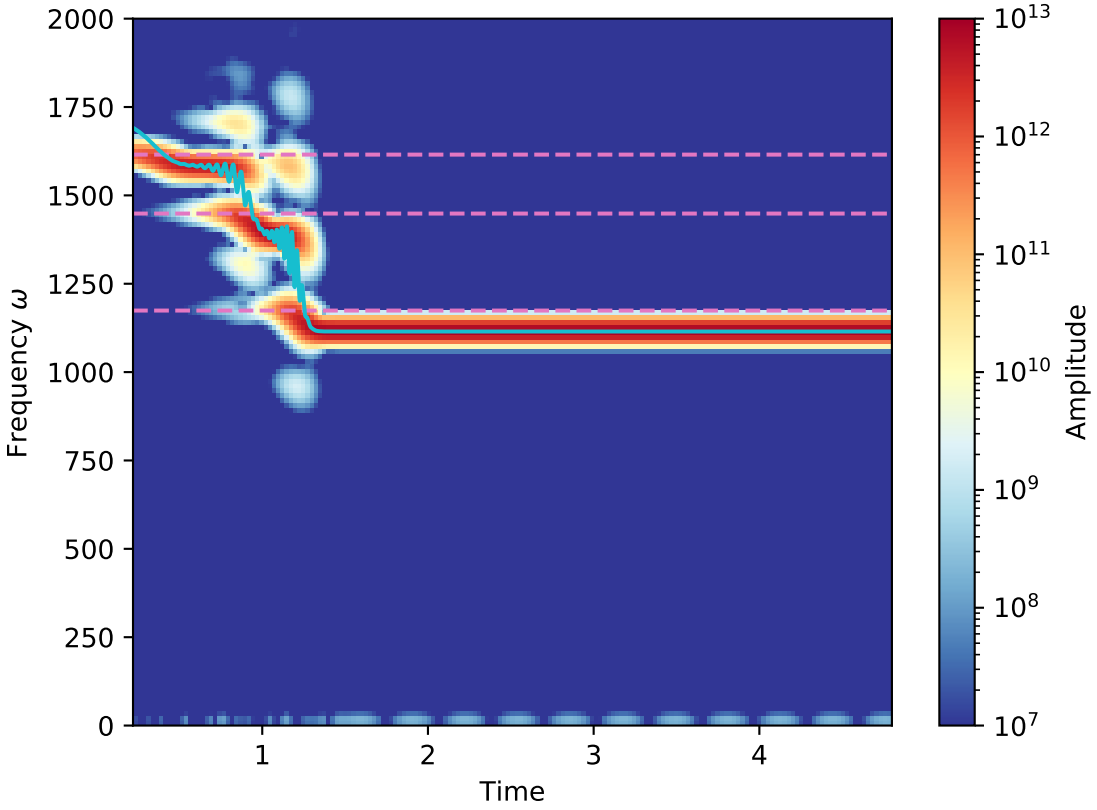

Figure 4.11: Spectrogram of $\mathrm{Re}\,(\varphi_3(v))$ for mixed mode initial data, with $r_+ = 100$, $\alpha = 0.9$, $L = 1$, $q = 11$, and $a_{\mathrm{Mix}} = 0.999$. Dashed lines indicate values of the initial mode frequencies (calculated using the linear analysis), solid corresponds to the superradiant bound $q\Phi_{\mathrm{AH}}(v)$. This shows a cascade through hairy black holes with $n = 2 \to 1 \to 0$. At early times the dominant mode is the $n = 2$. Eventually, the $n = 1$ mode grows exponentially. During the short coexistence period between the $n = 2$ and $n = 1$ mode the superradiant bound displays some oscillations, until the $n = 1$ is the dominanting mode. Later, a similar process takes places during the coexistence of the $n = 1$ and $n = 0$ modes. Finally, after the two transitions the spacetimes settles to a hairy black hole in its ground state, that is with the scalar field containing the $n = 0$ mode.

4.5 Summary

In this chapter we computed the $l = 0$ charged scalar quasinormal mode spectrum for RNAdS, and in cases of unstable modes, we numerically simulated the full nonlinear development.

The quasinormal mode analysis used the continued fraction method, which enabled us to study regions of parameter space that were not previously examined due to a lack of small parameter needed for analytic studies. We showed in particular that for large black holes, the zero-damped mode family can become superradiantly unstable, and exhibits behavior similar to the small black hole AdS mode family. Furthermore, the leading unstable mode is identified with the near-horizon condensation instability.

At the nonlinear level, we studied the evolution of these large-RN-AdS unstable modes. We showed that the generic end point is a static black hole with a (harmonically-oscillating) scalar condensate, similar to earlier results for small RN-AdS black holes in Chap. 3 [1], and planar [31] RN-AdS. We also showed that for black holes with multiple unstable modes, special initial data can be chosen that evolve to a transient excited hairy black hole solution before decaying to the generic end state.

It is tempting to draw an analogy between classical hairy black hole energy levels and quantum energy levels of atoms. In this picture (in AdS) the scalar field can only exchange energy (and charge and angular momentum) with the black hole, so the horizon plays the role of the atomic environment. In the black hole case, however, level transitions can only occur in the direction of decreasing overtone number. Transitions in the reverse direction are forbidden by the area theorem.

The reason that the final hairy black hole is always in the $n = 0$ configuration is because out of all quasinormal modes, the $n = 0$ mode has lowest $\mathrm{Re}\omega > 0$. The superradiance condition is $0 < \mathrm{Re}\omega < q\Phi_{\mathrm{H}}$, and as mass and charge extraction cause the upper bound to decrease, the $n = 0$ mode is the last to remain unstable. We were nevertheless able to obtain the transient excited hairy black holes because the instability growth rates of the overtones are comparable and we were free to choose special overtone initial data.

Had the growth rate of overtone modes been *higher* than the fundamental mode, the situation would be somewhat different. Although the final configuration would be unchanged (because of the ordering of the real parts of the frequencies), the excited hairy black hole states would occur transiently for *generic* initial data. This reverse ordering of overtone growth rates occurs for superradiantly-unstable angular harmonics of Proca fields in Kerr [96], which is relevant to searches for ultralight dark matter [97]. It would

be interesting to study any observational consequences of transient overtone equilibria in this context.

Another context where the interplay between instability criteria and growth rates leads to transient states in generic evolutions is the superradiant instability of Kerr-AdS. These states, however, involve different angular harmonics rather than radial overtones. Indeed recent simulations [98] of the Kerr-AdS superradiant instability show an evolution dominated by a series of epochs consisting of black resonators [62], which are themselves unstable [23].

Instability of RN-AdS and subsequent hairy black hole formation has been proposed as a holographic dual to a superconducting phase transition [29, 99]. It is intriguing to seek also a holographic interpretation of the transient hairy black hole equilibria that we uncovered.

More generally, our work underscores the importance of overtone modes and nonlinear effects in black hole perturbations. For perturbed black holes arising from a binary merger, recent works [100, 101, 102, 103] have argued for the need to include overtones to describe the early post-merger behavior as a combination of overtones evolving linearly in a Kerr background. Other works, however, have demonstrated the presence of additional nonlinear mode excitation [104, 105], sometimes through parametric instabilities [77, 106]. For weakly perturbed black holes, we measured a natural scaling (4.19) that describes nonlinear mode excitation in RN-AdS. Further work and numerical simulations will be needed to build intuition and understand the validity of linear analyses in strongly perturbed regimes and how linear results can be best combined to describe the regime of interest.

Chapter 5

Runaway Instabilities: "Unstable" Horizons

In this chapter we explore the linear and nonlinear behavior of a planar Schwarzschild-AdS black hole and two massive scalar fields. We show that above a critical energy density the system is stable, settling down to a hairy Schwarzschild-AdS black hole with one of the fields vanishing. Below the critical energy, however, the linear analysis reveals an unstable mode with postive imaginar frequency. We present the full nonlinear evolution of the stable and unstable cases. In the latter, the system develops arbitrarily large curvature close to the horizon, and the system does not reach a stationary end point.

5.1 General Motivation

The string theory/gauge theory correspondence [107, 108] is by now a mature framework exploited to address interesting questions in strongly coupled gauge theories that are often inaccessible with other theoretical tools. In a nutshell, this duality establishes a *holographic correspondence* (a dictionary) between two objects: a non-abelian gauge theory and a higher-dimensional gravitational theory/string theory in asymptotically anti de-Sitter space-time. One particularly appealing consequence of this correspondence is the fact that questions about the gauge theory in strongly coupled regimes are mapped onto questions in classical gravity. Likewise, a dual gauge theory perspective allows for different, and often intuitive, understanding of instabilities in black hole/black brane spacetimes.

Indeed, lets recall the physics of *holographic superconductors* [40, 29]. Consider the

four-dimensional effective gravitational action[1] in asymptotically AdS_4 (dual to a three-dimensional conformal field theory CFT_3),

$$S_4 = \frac{1}{2\kappa^2}\int_{\mathcal{M}_4} dx^4 \left[R + 6 - \frac{1}{4}F^{\mu\nu}F_{\mu\nu} - \frac{1}{2}\left(\nabla\phi\right)^2 + \phi^2\right] . \tag{5.1}$$

The four dimensional gravitational constant κ is related to a central charge c of the CFT_3 as

$$c = \frac{192}{\kappa^2} , \tag{5.2}$$

$F_{\mu\nu}$ is a field strength of a global $U(1)$ symmetry of the CFT, and ϕ is a (neutral) gravitational bulk scalar with

$$L^2 m_\phi^2 = -2 , \tag{5.3}$$

which is dual to a dimension $\Delta_\phi = 2$ operator $\mathcal{O}_\phi$ of a boundary theory[2]. Note that there is $\mathbb{Z}_2$ symmetry in the model, associated with this scalar, $\phi \leftrightarrow -\phi$. As it is well-known, there are two phases of equilibrium states of this CFT_3 at a finite temperature T and a $U(1)$ global symmetry chemical potential μ, distinguished whether $\langle\mathcal{O}_\phi\rangle = 0$ or $\langle\mathcal{O}_\phi\rangle \neq 0$. The $\langle\mathcal{O}_\phi\rangle = 0$ phase exists for arbitrary temperature $T \geq 0$ and it is gravitationally described by Reissner-Nordstrom AdS_4 black brane with unbroken $\mathbb{Z}_2$ symmetry, correspondingly $\phi \equiv 0$. For sufficiently small T/μ this $\mathbb{Z}_2$ symmetric phase becomes unstable [29]: on the gauge theory side of the correspondence the instability is a generic instability of the order parameter in the mean-field theory of thermal second-order phase transitions; on the gravity side, this is a Gregory-Laflamme (GL) type instability [84] (in the sense of being unstable to long-wavelength perturbations) due to scalarization of the Reissner-Nordstrom AdS_4 black brane horizon. To understand the gravitational origin of the instability the authors of [29] noted that even though the scalar ϕ is above the AdS_4 Breitenlohner-Freedman (BF) bound

$$m_\phi^2 = -2 \qquad > \qquad m^2_{BF[AdS_4]} = -\frac{(4-1)^2}{4L^2} = -\frac{9}{4} , \tag{5.4}$$

as the Reissner-Nordstrom AdS_4 black brane becomes extremal ($T/\mu \to 0$), it develops $AdS_2 \times R^2$ near horizon geometry with the curvature radius $L_2^2 = \frac{L^2}{6}$. In this limit

$$m_\phi^2 = -2 \qquad < \qquad m^2_{BF[AdS_2]} = -\frac{(2-1)^2}{4L_2^2} = -\frac{3}{2} , \tag{5.5}$$

[1] We set the radius L of an asymptotic AdS_4 geometry to unity.

[2] ϕ has two alternative quantizations in AdS_4 [109]; our results do not depend on this choice.

and the bulk scalar ϕ becomes unstable (the quasinormal frequency of its linearized fluctuations has $\mathrm{Im}[\omega] > 0$). The condensation of the gravitational scalar ϕ at low temperatures is dynamically saturated by nonlinear effects, spontaneously breaking $\mathbb{Z}_2$ symmetry and leading to a new equilibrium phase of the CFT with $\langle \mathcal{O}_\phi \rangle \neq 0$.

There exist many studies and generalizations of the described phenomena in holography[3]. In this chapter we focus on a less-known, exotic property of certain black brane/black hole horizons. As in the example of the holographic superconductor above, imagine a holographic[4] horizon with a discrete (or continuous) symmetry. Suppose that there is a critical energy[5] or energy density (for gauge theory states with translational invariance) below which the horizon becomes unstable with respect to symmetry breaking (GL) fluctuations. There is an equilibrium phase with spontaneously broken symmetry, branching off the GL onset of the instability, yet, this phase does not exist below the critical energy; moreover, it has lower entropy above the criticality than the symmetric phase. Thus, the horizon representing the symmetric thermal state is unstable, but it is unknown what the end point of its instability is.

To our knowledge, the first realization of the above exotic scenario appeared in [39] which was later found in a top-down holographic model in [111]. Finally, the same exotic physics is behind the leading instability of small black holes in $AdS_5 \times S^5$ (dual to $SO(6)$-symmetric states of strongly coupled $\mathcal{N} = 4$ SYM plasma) [112, 113, 114, 115]. Here, we study the endpoint of this exotic horizon instability.

In the next section we briefly review the bottom-up model of [39]. We discuss the equilibrium states of the system, and the linearized instability of symmetric phase states at low energy densities. We construct the symmetry-broken phase of the system and demonstrate that it is never preferred dynamically. In Sec. 5.3 we employ a characteristic formulation of the gravitational dynamics [55] in our exotic model. We confirm the onset of the GL instability dynamically, and compare the linear growth (below the criticality) and decay (above the criticality) rates of the symmetry breaking fluctuations with the corresponding quasinormal mode (QNM) computations of Sec. 5.2. Next, we present results for the full-nonlinear evolutions of unstable horizons. Details of the numerical implementation as well as the convergence and the validation of the code are delegated to Appendix C.1. We conclude and discuss open questions in Sec. 5.4.

[3] See [110] and references therein.

[4] We point out this feature occurs in top down holographic models, and thus is of importance to issues of equilibration and thermalization in strongly coupled gauge theories.

[5] As we study dynamical phenomena, we work in a microcanonical ensemble.

5.2 Exotic hairy black holes at equilibrium

In this section we review the bottom-up holographic model of the exotic black holes presented in [39].

The effective four-dimensional gravitational bulk action, dual to a field-theoretic setup discussed in the introduction, takes the form

$$S_4 = S_{CFT} + S_r + S_i = \frac{1}{2\kappa^2}\int dx^4\sqrt{-\gamma}\left[\mathcal{L}_{CFT} + \mathcal{L}_r + \mathcal{L}_i\right] , \tag{5.6}$$

$$\mathcal{L}_{CFT} = R + 6\,, \qquad \mathcal{L}_r = -\frac{1}{2}\left(\nabla\phi\right)^2 + \phi^2\,, \qquad \mathcal{L}_i = -\frac{1}{2}\left(\nabla\chi\right)^2 - 2\chi^2 - g\phi^2\chi^2\,; \tag{5.7}$$

where we split the action into (a holographic dual to) a CFT part S_{CFT}; its deformation by a relevant operator $\mathcal{O}_r$; and a sector S_i involving an irrelevant operator $\mathcal{O}_i$ along with its mixing with $\mathcal{O}_r$ under the renormalization-group dynamics. We take bulk quantization so that the scaling dimension of $\mathcal{O}_r$ is $\Delta_r = 2$; the scaling dimension of $\mathcal{O}_i$ is $\Delta_i = 4$. In order to have asymptotically AdS_4 solutions, we assume that only the normalizable mode of $\mathcal{O}_i$ is nonzero near the boundary.

The gravitational action (5.6) has $\mathbb{Z}_2 \times \mathbb{Z}_2$ discrete symmetry that acts as a parity transformation on the scalar fields ϕ and χ. The discrete symmetry $\phi \leftrightarrow -\phi$ is explicitly broken by the relevant deformation of the CFT,

$$\mathcal{H}_{CFT} \;\rightarrow \mathcal{H}_{CFT} + \Lambda\;\mathcal{O}_r\;, \tag{5.8}$$

with Λ being the deformation mass scale, while the $\chi \leftrightarrow -\chi$ symmetry is broken spontaneously. The mechanism for the long-wavelength instability at play in (5.6) was identified by Gubser [38] through the following observations:

- consider the linearized dynamics of the χ-sector in the mass-deformed CFT dual to $S_{CFT} + S_r$ in (5.6);
- for the quartic coupling $g < 0$, the scalar χ has an effective mass

$$m_\chi^2 = 4 - 2\;|g|\;\phi^2\,; \tag{5.9}$$

- homogeneous and isotropic thermal equilibrium states of $S_{CFT} + S_r$ at low temperature (energy densities) would result in large values of ϕ at the horizon of the dual gravitational description, thus driving m_χ^2 below the effective BF bound.

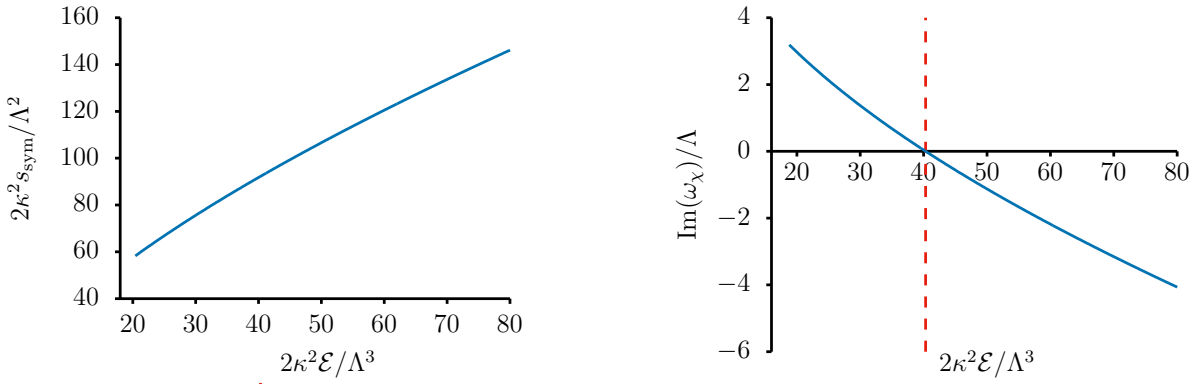

Figure 5.1: (Left:) Entropy density s_{sym} of the $\mathbb{Z}_2$-symmetric phase, *i.e.*, with $\langle\mathcal{O}_i\rangle = 0$, of exotic black holes as a function of energy density $\mathcal{E}$. (Right:) As the energy density is decreased below the critical one $\mathcal{E}_{crit}$, denoted by a vertical (red) dashed line, and given that the symmetric phase is perturbatively unstable with respect to linearized $\mathbb{Z}_2$-symmetry breaking fluctuations, the imaginary part of the frequency ω_χ of these fluctuations at zero spatial momenta is positive.

A detailed analysis of the homogeneous and equilibrium states of the holographic model (5.6) in the canonical ensemble were presented in [39]. Here, we present results in the microcanonical ensemble. We omit all the technical details as the following discussion is a special case of the dynamical setup of Sec. 5.3.

- There are two equilibrium phases of the holographic model (5.6), distinguished by the symmetry property under $\chi \leftrightarrow -\chi$: the symmetric phase with $\langle\mathcal{O}_i\rangle = 0$, and the symmetry broken phase with $\langle\mathcal{O}_i\rangle \neq 0$.

- The entropy density of the symmetric phase s_{sym} as a function of the energy density $\mathcal{E}$ is presented in figure 5.1. While this phase is thermodynamically stable $\frac{\partial^2\mathcal{E}}{\partial s_{sym}^2} > 0$, it is perturbatively unstable with respect to a linearized symmetry breaking fluctuations [116]: for $\mathcal{E} < \mathcal{E}_{crit}$, with
$$\frac{2\kappa^2\mathcal{E}_{crit}}{\Lambda^3} = 40.320(4)\,, \tag{5.10}$$
the quasinormal modes of the symmetry breaking linearized χ-fluctuations develop a positive imaginary part, $\mathrm{Im}\,(\omega_\chi) > 0$. As emphasized in [116], this model is one of the explicit counterexamples of the Gubser-Mitra "correlated stability conjecture" [117, 118].

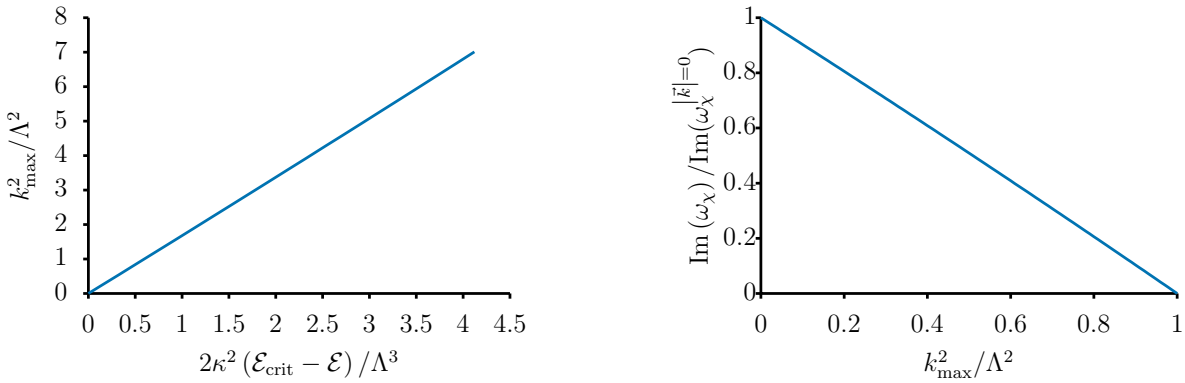

Figure 5.2: (Left:) When $\mathcal{E} < \mathcal{E}_{crit}$, $\mathbb{Z}_2$-symmetry breaking fluctuations in the symmetric phase of the exotic black holes are unstable; the instability persists for the range of the spatial momenta (along the translationally invariant directions of the horizon) $\vec{k}$ of the fluctuations, $|\vec{k}| \in [0, k_{max}]$. (Right:) Characteristic dependence of $\mathrm{Im}(\omega_\chi)$ on $|\vec{k}|$ (here $\mathcal{E}/\mathcal{E}_{crit} = 0.89780(8)$).

- Notice that there is a relation between the behavior of the unstable χ-mode and the 'GL' instability, in that the χ-instability requires long wavelength modes, *i.e.,* the instability is cut-off at
$$|\vec{k}| \leq k_{max} \propto (\mathcal{E}_{crit} - \mathcal{E})^{1/2} \,. \tag{5.11}$$
See figure 5.2 for further details.

However, there is a clear distinction: in the GL instability [84] the unstable mode is hydrodynamic, while the χ-QNM behaves non-hydrodynamically away from the critical point, *i.e.,* $\mathrm{Im}(\omega_\chi) \neq 0$ as the spatial momentum (along the translationally invariant directions of the horizon) vanishes, $|\vec{k}| = 0$.

- The expectation value of $\langle \mathcal{O}_i \rangle \neq 0$ in the symmetry broken phase of the model as a function of the equilibrium energy density is presented in figure 5.3. This phase exists only for $\mathcal{E} > \mathcal{E}_{crit}$, with
$$\lim_{\mathcal{E}\to\mathcal{E}_{crit}+}\left(\langle \mathcal{O}_i \rangle \;\propto -\left(\mathcal{E}-\mathcal{E}_{crit}\right)^{1/2}\right) = 0 \,. \tag{5.12}$$
The equilibrium symmetry broken phase is never realized in a microcanonical ensemble as it has smaller entropy density compared to the symmetric phase for the same energy density.

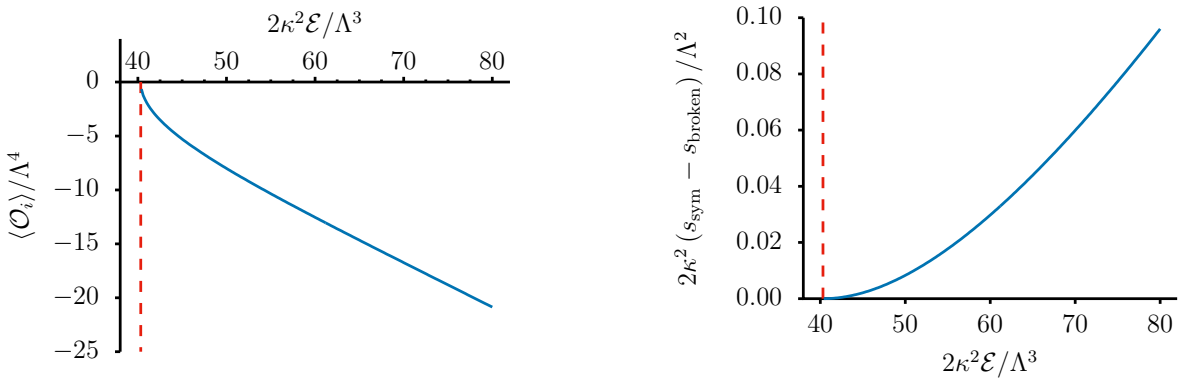

Figure 5.3: (Left:) Exotic black holes have a new equilibrium phase with spontaneously broken $\mathbb{Z}_2$-symmetry at energy densities exceeding the critical one, denoted by a vertical (red) dashed line. This phase is characterized by $\langle\mathcal{O}_i\rangle \neq 0$, with the expectation value vanishing precisely at $\mathcal{E} = \mathcal{E}_{crit}$. (Right:) The equilibrium symmetry breaking phase $\langle\mathcal{O}_i\rangle \neq 0$ is never realized in a microcanonical ensemble as its entropy density is always below the corresponding entropy density of the symmetric phase.

- Figure 5.1 exhibits the leading instability at low-energies of the symmetric phase in the holographic model (5.6). In fact, there is a tower of unstable modes (overtones) with critical energies $\mathcal{E}^{(n)}_{crit}$,

$$\mathcal{E}^{(n)}_{crit} < \mathcal{E}^{(n-1)}_{crit}\,, \qquad \mathcal{E}^{(0)}_{crit} \equiv \mathcal{E}_{crit}\,, \qquad \mathcal{E}^{(1)}_{crit} \approx 0.26380(6)\ \mathcal{E}_{crit}\,, \tag{5.13}$$

  parameterized by the number of nodes (n) in the radial profile of the linearized gravitation fluctuations χ. Each subleading instability of the symmetric phase identifies a branch point of a new unstable phase with $\langle\mathcal{O}_i\rangle \neq 0$. Properties of these new phases are analogous to the broken phase in figure 5.3, see also [39].

- The analysis reported above was performed with the nonlinear coupling in the effective action (5.6) set to $g = -100$. The phase diagram of the model does not change as g changes, as long as $g < 0$, see figure 5.4. The (red) dashed line in the right panel represents the estimate for the vacuum energy of the symmetric phase:

$$\frac{2\kappa^2\mathcal{E}^{vacuum}}{\Lambda^3} = 0.1233(2)\,. \tag{5.14}$$

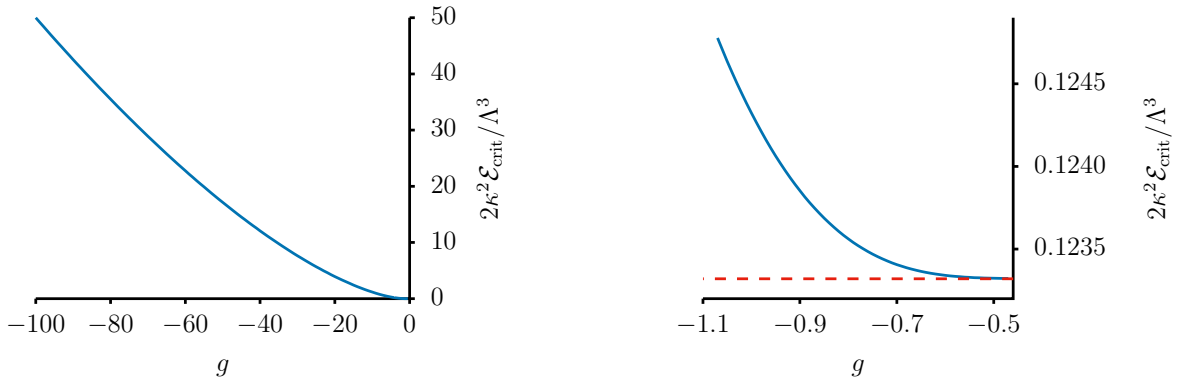

Figure 5.4: (Left:) Critical energy density of the leading instability of the symmetric phase as a function of the nonlinear coupling g. (Right:) It appears that the instability persists in the limit $g \to 0_-$. The (red) dashed line identifies the vacuum energy of the symmetric phase, see (5.14).

Notice that $\mathcal{E}^{vacuum}_{sym} \to 0$ in the conformal limit $\Lambda \to 0$; to obtain the better estimate for $\mathcal{E}^{vacuum}$ we extended the analysis of the symmetric phase to the low-entropy region, as shown in figure 5.5, and extrapolated the energy-entropy data to zero entropy density (indicated by the (red) dashed line). The right panel shows the dependence of the temperature T_{sym} of the symmetric phase black hole — the limit $\mathcal{E} \to \mathcal{E}^{vacuum}$ appears to correspond to an extremal limit.

In this section we focused on the static phase diagram, along with the linearized (in)stabilities of these phases, of the holographic action (5.6), dual to non-conformal QFT_3 in Minkowski space-time $R^{1,2}$. In what follows we will discuss the dynamical case. In Sec. 5.4, we comment on properties of the model with QFT_3 residing in $R \times S^2$. Additionally, we comment on the extension of the model (5.6) with the gravitational potential for the scalar χ bounded from below.

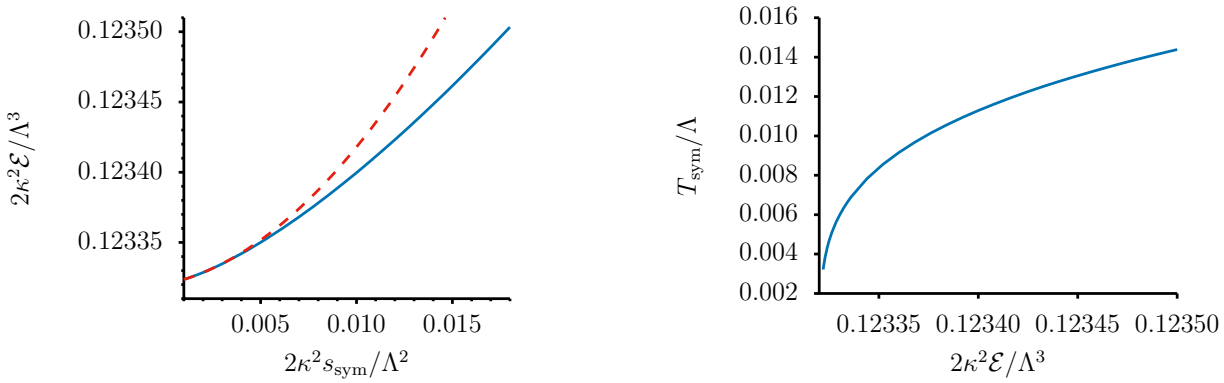

Figure 5.5: (Left:) Energy density of the symmetric phase as a function of the entropy density. The (red) dashed line is the extrapolation of the energy-entropy data (solid blue line) in the limit $s_{sym} \to 0$. The extrapolation is used to estimate the vacuum energy of the symmetric phase (5.14). (Right:) The dependence of the symmetric phase black hole temperature as a function of the energy density.

5.3 Dynamics of the exotic unstable horizons

In this section we discuss dynamical properties of the holographic model (5.6), with the boundary QFT_3 formulated in $R^{1,2}$. We follow closely the holographic numerical framework in the characteristic formulation as described in, *e.g.,* [55].

5.3.1 Dynamical setup

We assume translational invariance along the spatial directions of the boundary. The relevant fields are described by

$$\begin{aligned} ds_4^2 &= 2dt\,(dr - A(t,r)\,dt) + \Sigma(t,r)^2\,\left[dx_1^2 + dx_2^2\right]\,, \\ \phi &= \phi(t,r)\,, \qquad \chi = \chi(t,r)\,. \end{aligned} \tag{5.15}$$

Einstein equations define the following evolution equations of motion:

$$
\begin{aligned}
0 &= d'_+\Sigma + d_+\Sigma\ (\ln\Sigma)' - \frac{3}{2}\Sigma - \frac{1}{4}\Sigma\left(\phi^2 - 2\chi^2 - g\phi^2\chi^2\right)\ , \\
0 &= d'_+\phi + d_+\phi\ (\ln\Sigma)' + \frac{d_+\Sigma}{\Sigma}\ \phi' + \phi\left(1 - g\chi^2\right)\ , \\
0 &= d'_+\chi + d_+\chi\ (\ln\Sigma)' + \frac{d_+\Sigma}{\Sigma}\ \chi' - \chi\left(2 + g\phi^2\right)\ , \\
0 &= A'' - 2\frac{d_+\Sigma}{\Sigma^2}\ \Sigma' + \frac{1}{2}d_+\phi\ \phi' + \frac{1}{2}d_+\chi\ \chi'\ ,
\end{aligned}
\tag{5.16}
$$

together with the constraint equations:

$$
0 = \Sigma'' + \frac{1}{4}\Sigma\left((\phi')^2 + (\chi')^2\right)\ , \tag{5.17}
$$

$$
\begin{aligned}
0 &= d_+^2\Sigma - 2Ad'_+\Sigma - \frac{d_+\Sigma}{\Sigma^2}\ \left(A\Sigma^2\right)' \\
&\quad + \frac{1}{4}\Sigma\left((d_+\phi)^2 + (d_+\chi)^2 + 2A\left(6 + \phi^2 - 2\chi^2 - g\phi^2\chi^2\right)\right)\ ,
\end{aligned}
\tag{5.18}
$$

where $' \equiv \partial_r$ and $d_+ \equiv \partial_t + A\ \partial_r$. The constraint equations are preserved by the evolution equations provided they are satisfied at a given timelike surface (*e.g.,* [119, 120, 54]) — which in our case is the AdS boundary.

The general asymptotic boundary ($r \to \infty$) solution of the equations of motion, given by

$$
\begin{aligned}
\Sigma &= r + \lambda(t) - \frac{1}{8}p_1^2\ \frac{1}{r} + \mathcal{O}\left(\frac{1}{r^2}\right)\ , \\
A &= \frac{r^2}{2} + \lambda(t)\ r - \frac{1}{8}p_1^2 + \frac{1}{2}\lambda(t)^2 - \dot{\lambda}(t) \\
&\quad + \left(\mu - \frac{1}{4}p_1p_2(t) - \frac{1}{4}p_1^2\lambda(t)\right)\frac{1}{r} + \mathcal{O}\left(\frac{1}{r^2}\right)\ , \\
\phi &= \frac{p_1}{r} + \frac{p_2(t)}{r^2} + \mathcal{O}\left(\frac{1}{r^3}\right)\ , \\
\chi &= \frac{q_4(t)}{r^4} + \mathcal{O}\left(\frac{1}{r^5}\right)\ ,
\end{aligned}
\tag{5.19}
$$

is characterized by two constants $\{p_1, \mu\}$, and three dynamical variables $\{p_2(t), q_4(t), \lambda(t)\}$. These parameters have the following interpretation:

- p_1 and $p_2(t)$ are correspondingly the non-normalizable and normalizable coefficients of the bulk scalar ϕ, identified with the deformation mass scale Λ and the expectation value of the relevant operator $\mathcal{O}_r$ of the dual QFT_3,

$$p_1 = \Lambda\,, \qquad p_2(t) = \langle \mathcal{O}_r(t) \rangle\,; \tag{5.20}$$

- $q_4(t)$ is the normalizable coefficient of the bulk scalar χ, identified with the expectation value of the $\mathbb{Z}_2$-symmetry breaking irrelevant operator $\mathcal{O}_i$ of the dual QFT_3,

$$q_4(t) = \langle \mathcal{O}_i(t) \rangle\,; \tag{5.21}$$

- μ is related to the conserved energy density $\mathcal{E}$ of the boundary QFT_3 as follows

$$\frac{2\kappa^2 \mathcal{E}}{\Lambda^3} = \frac{-4\mu}{\Lambda^3}\,; \tag{5.22}$$

- $\lambda(t)$ is the residual radial coordinate diffeomorphisms parameter

$$r \to r + \lambda(t)\,, \tag{5.23}$$

  which can adjusted to keep the apparent horizon at a fixed location, which in our case will be $r = 1$:

$$\Big(\partial_t + A(t,r)\,\partial_r\Big)\Sigma(t,r) \;\equiv\; d_+\Sigma(t,r)\Big|_{r=1} = 0\,. \tag{5.24}$$

To initialize evolution at $t = 0$, we provide the bulk scalar profiles,

$$\phi(t=0,r) = \frac{p_1}{r} + \mathcal{O}\left(\frac{1}{r^2}\right)\,, \qquad \chi(t=0,r) = \mathcal{O}\left(\frac{1}{r^4}\right)\,, \tag{5.25}$$

along with the values of $\{p_1, \mu\}$, specifying the dual QFT_3 mass scale Λ (5.20) and the initial state energy density $\mathcal{E}$ (5.22). The constraint equation (5.17) is then used to determine an initial profile $\Sigma(t=0,r)$. Eqs. (5.16) are then employed to evolve such data (5.25) in time. The second constraint (5.18), representing the conservation of the energy density, is enforced requiring that a parameter μ in the asymptotic expansion of A, see (5.19), is time-independent.

Details of the numerical implementation, specific choices of the initial conditions (5.25) used, and code convergence tests can be found in Appendix C.1.

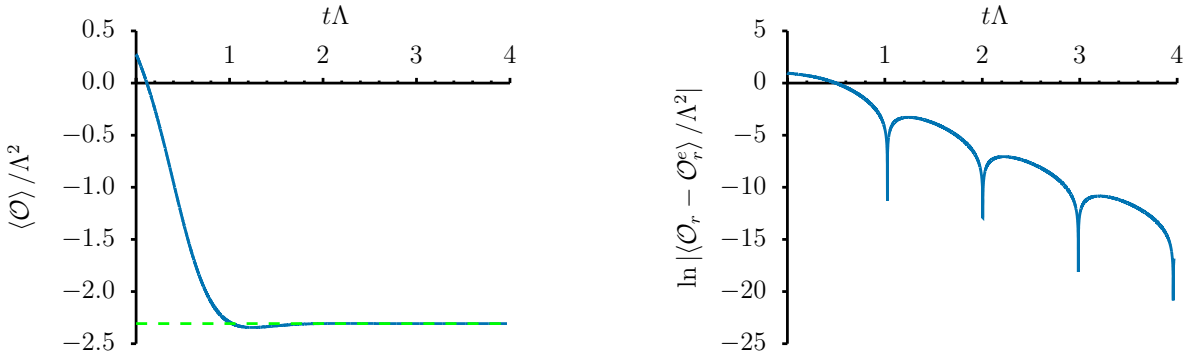

Figure 5.6: (Left:) Time evolution of a typical state in $\mathbb{Z}_2$-symmetric phase of exotic black holes. The (green) dashed line is the equilibrium value $\langle\mathcal{O}_r^e\rangle$ of the operator $\mathcal{O}_r$. (Right:) The approach towards equilibrium occurs in characteristic quasinormal mode ringing of the black hole horizon.

5.3.2 Dynamics of the symmetric sector

To study dynamics in the *symmetric sector*, we adopt initial conditions as described in Appendix C.1.3 with $\mathcal{A}_p \neq 0$ and $\mathcal{A}_q = 0$, implying that (in $\lambda_0 \equiv 0$ gauge)

$$\phi\Big|_{t=0} = \frac{p_1}{r} + \mathcal{A}_p \, \frac{\exp\left(-\frac{1}{r}\right)}{r^2} \,, \qquad \chi(t,x) \equiv 0 \,. \tag{5.26}$$

Results of a typical evolution are presented in figures 5.6 and 5.7. Here, the energy density is below the critical one (5.10),

$$\mathcal{E} = 0.793642 \; \mathcal{E}_{crit} \qquad \Longleftrightarrow \qquad \mu = -4\Lambda^3 \,. \tag{5.27}$$

The left panel of figure 5.6 shows time evolution of the expectation value of $\mathcal{O}_r$. Within a time scale $t \sim \Lambda^{-1}$ the system equilibrates. The equilibrium expectation value, defined as

$$\langle\mathcal{O}_r^e\rangle = \lim_{t\Lambda\to\infty} \langle\mathcal{O}_r(t)\rangle \,, \tag{5.28}$$

is represented by a (green) dashed line. We used the value of $\langle\mathcal{O}_r^e\rangle$ obtained from the independent analysis of the static configurations, reported in Sec. 5.2, evaluated at the energy density (5.27). Consistency of (5.28) is an important check of our evolution. The

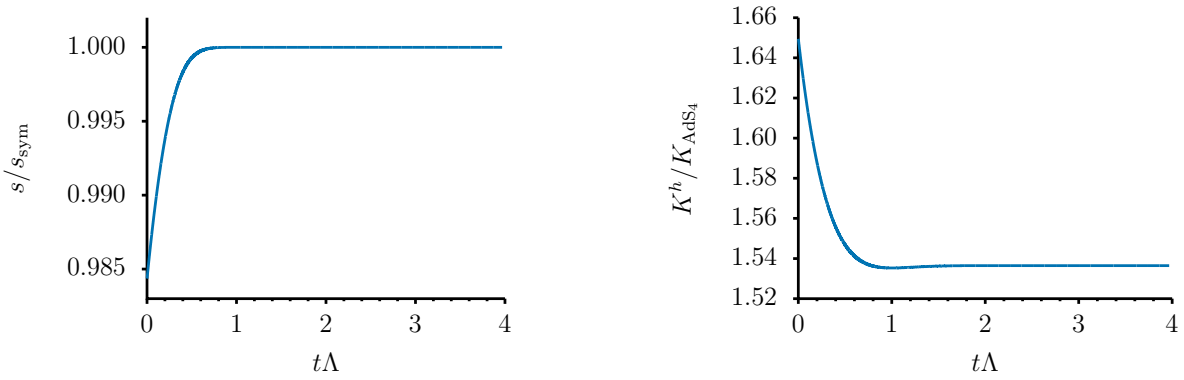

Figure 5.7: (Left:) Dynamical entropy density s relative to the equilibrium entropy density s_{sym} in $\mathbb{Z}_2$-symmetric sector of exotic black holes. (Right:) Corresponding evolution of the bulk Kretschmann scalar.

right panel of figure 5.6 illustrates the system's approach to equilibrium, which displays a typical ϕ quasinormal mode ring-down of the exotic black hole horizon.

The entropy density is an intrinsically equilibrium concept in QFTs. One benefit of the holographic framework is that it provides a well-motivated notion of the non-equilibrium (even far from equilibrium) entropy. Following [121, 122] we identify nonequilibrium entropy density s with the Bekenstein-Hawking entropy corresponding to the apparent horizon (see (5.24)) area density

$$s(t) = \frac{2\pi}{\kappa^2}\,\Sigma(t,r)^2\Big|_{r=1}\,. \tag{5.29}$$

The right panel of figure 5.7 shows the evolution of thus defined dynamical entropy density. Notice that in line with the second law of thermodynamics, $\dot{s}(t) \geq 0$ and approaches at late times the equilibrium value s_{sym}, computed independently for the static configuration with the energy density (5.27).

While we can study the non-equilibrium dynamics in $\mathbb{Z}_2$-symmetric sector of the holographic model (5.6), completely suppressing the χ-scalar fluctuations as in (5.26), at $\mathcal{E} < \mathcal{E}_{crit}$, and in particular in the discussed example (5.27), this is an unphysical approximation — in realistic settings the fluctuations of the χ scalar will always be present, and would destabilize this $\mathbb{Z}_2$-symmetric dynamics. In the right panel of figure 5.7 we show

the time dependence of the bulk Kretschmann scalar K evaluated at the apparent horizon,

$$K(t) = R_{abcd}R^{abcd}\Big|_{(t,r=1)} , \tag{5.30}$$

relative to the AdS_4 Kretschmann scalar K_{AdS_4} (recall $K_{AdS_4} = \text{const} = 24$), to emphasize the fact that even if the symmetric sector is unstable, its bulk dynamics is weakly curved. Thus, higher derivative supergravity and string corrections are arguably irrelevant for the onset of the $\mathbb{Z}_2$ symmetry breaking instability of the exotic black hole horizons.

5.3.3 Instability of the symmetric sector

In this section we study *linearized fluctuations* of the $\mathbb{Z}_2$ symmetry breaking operator $\mathcal{O}_i$ in the symmetric phase of the holographic model (5.6). We initialize the symmetric sector of the model as explained in Sec. 5.3.2 for energy densities above/below the critical one. The bulk scalar χ, dual to an irrelevant operator $\mathcal{O}_i$, is initialized as (in $\lambda_0 = 0$ gauge, see Appendix C.1.3)

$$\chi\Big|_{t=0} = \mathcal{A}_q \, \frac{\exp\left(-\frac{1}{r}\right)}{r^4} . \tag{5.31}$$

To treat symmetry breaking in a linear approximation, we set $\chi(t,x) \equiv 0$ in all dynamical equations, except for the third equation in (5.16) — the only one linear in the field χ and which determines its dynamics — which is kept unchanged.

Figure 5.8 presents the linearized fluctuations of the symmetry breaking operator $\mathcal{O}_i$ during evolution of the symmetric sector with

$$\mathcal{E} = 0.793642 \; \mathcal{E}_{crit} \qquad \Longleftrightarrow \qquad \mu = -4\Lambda^3 . \tag{5.32}$$

After a time $t \sim \Lambda^{-1}$ the symmetric sector equilibrates, and $\langle \mathcal{O}_i \rangle$ exhibits an exponential growth with time as it evolves over such state. The growth rate can be extracted at late times [(red) dashed line, right panel]:

$$\begin{aligned} \ln|\langle \mathcal{O}_i \rangle/\Lambda^4|\Big|_{red\ line\ fit} &= -0.66414(3) + 1.0869(7)\ t\Lambda , \\ \text{Im}\,(\omega_\chi)/\Lambda\Big|_{fit} &= 1.0869(7) . \end{aligned} \tag{5.33}$$

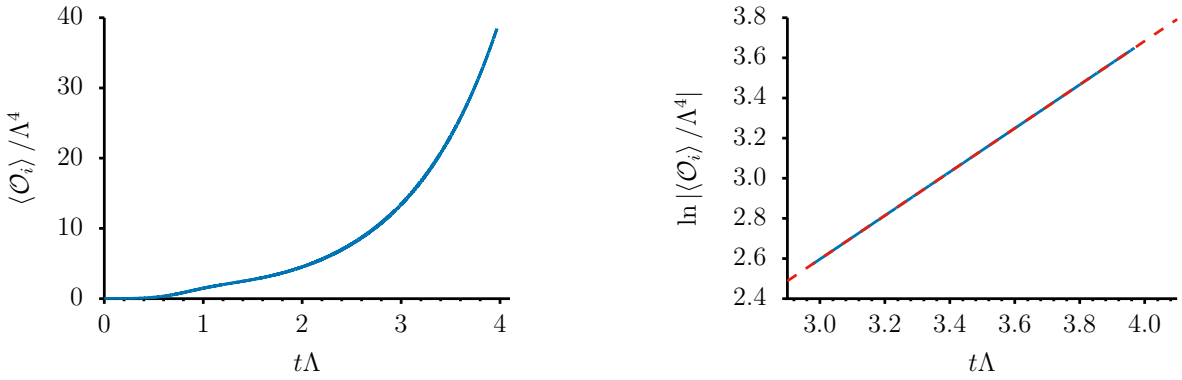

Figure 5.8: (Left:) Linearized fluctuations of the symmetry breaking operator $\mathcal{O}_i$ during the dynamical evolution of the $\mathbb{Z}_2$-symmetric sector of exotic black holes with $\mathcal{E} < \mathcal{E}_{crit}$. (Right:) The dashed red line is the linearized fit to the exponential growth of $\langle \mathcal{O}_i \rangle$ at late times.

This is in excellent agreement with the independent computation of the χ-scalar QNM frequencies reported in figure 5.1 at energy density (5.32):

$$\frac{\text{Im}\,(\omega_\chi)\Big|_{fit}}{\text{Im}\,(\omega_\chi)\Big|_{QNM}} = 0.99997(3)\ . \tag{5.34}$$

Figure 5.9 presents the linearized fluctuations of the symmetry breaking operator $\mathcal{O}_i$ during evolution of the symmetric sector with

$$\mathcal{E} = 1.1904(6)\ \mathcal{E}_{crit} \qquad \Longleftrightarrow \qquad \mu = -6\Lambda^3\ . \tag{5.35}$$

Again, after a time $t \sim \Lambda^{-1}$ the symmetric sector equilibrates, and the evolution of $\langle \mathcal{O}_i \rangle$ over such state exhibits an exponential decay with time. The decay rate can be extracted at late times [(red) dashed line, right panel]:

$$\begin{aligned} \ln |\langle \mathcal{O}_i \rangle / \Lambda^4| \Big|_{red\ line\ fit} &= -0.28139(8) - 0.90347(9)\ t\Lambda\ , \\ \text{Im}\,(\omega_\chi)/\Lambda \Big|_{fit} &= -0.90347(9)\ . \end{aligned} \tag{5.36}$$

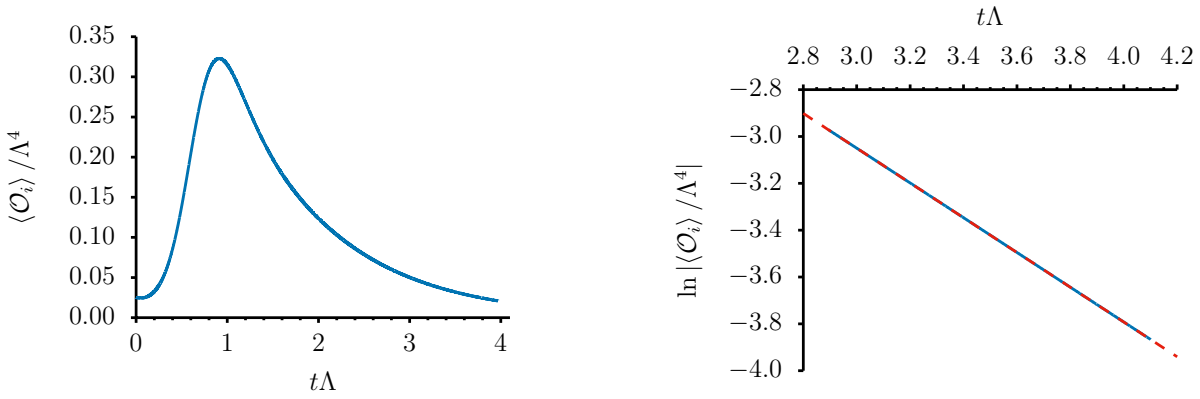

Figure 5.9: (Left:) Linearized fluctuations of the symmetry breaking operator $\mathcal{O}_i$ during dynamical evolution of the $\mathbb{Z}_2$-symmetric sector of exotic black holes with $\mathcal{E} > \mathcal{E}_{crit}$. (Right:) The (red) dashed line is the linearized fit to the exponential decay of $\langle \mathcal{O}_i \rangle$ at late times.

This also agrees with the independent computation of the χ-scalar QNM frequencies reported in figure 5.1 at energy density (5.35):

$$\frac{\mathrm{Im}\,(\omega_\chi)\Big|_{fit}}{\mathrm{Im}\,(\omega_\chi)\Big|_{QNM}} = 1.0000(2)\ . \tag{5.37}$$

Notice that the fluctuations of χ do not oscillate (both in the stable, *i.e.*, those that give rise to equilibrium, and unstable scenarios), *i.e.*,

$$\mathrm{Re}\,(\omega_\chi)\Big|_{QNM} = 0\ . \tag{5.38}$$

We believe this is a reflection of the spontaneous character of the symmetry breaking due to these fluctuations at the horizon[6] together with the boundary conditions adopted.

[6]Similar phenomena were observed in [123].

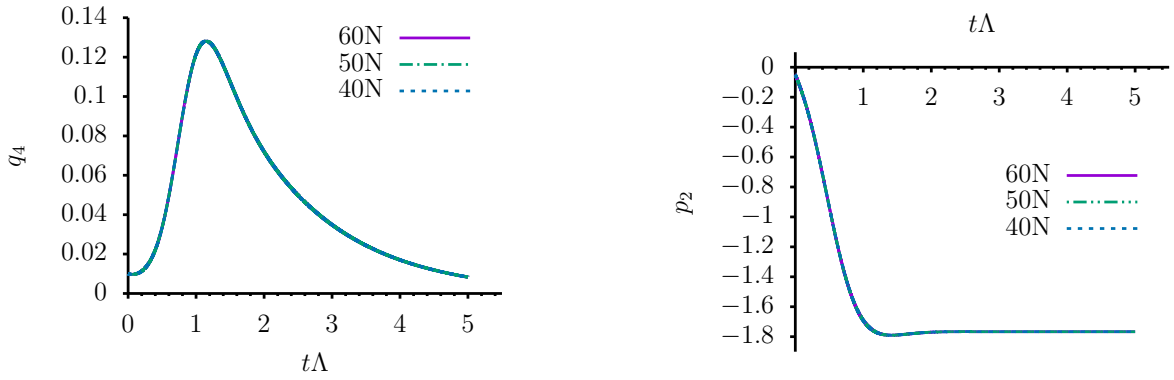

Figure 5.10: p_2 and q_4 vs. time for the stable case.

5.3.4 Fully non-linear evolutions of stable and unstable black holes

We now turn our attention to the fully non-linear behavior. Thanks to the simulations' ability to account for the backreaction of the field χ a rich phenomenology is uncovered. To aid in the interpretation of the results, we monitor several quantities:

- The dynamical behavior of p_2 and q_4.
- The area of the apparent and event horizons (see Appendix C.1.5).
- The behavior of the Kretschmann curvature scalar $K = R_{abcd}R^{abcd}$ (normalized by the value of K for pure AdS).

As a first case of study, we confirm that for $\mathcal{E} > \mathcal{E}_{crit}$ the behavior observed is consistent with that captured by the linearized analysis described in Sec. 5.3.3. For this case, the system asymptotically approaches a stationary hairy black hole which is evidenced by a non-zero asymptotic value of p_2 as illustrated in figure 5.10 as well as the behavior of the normalized curvature scalar K shown in figure 5.11. This figure, also shows that at late times the event and apparent horizon coincide and remain stationary.

On the other hand, the case where $\mathcal{E} < \mathcal{E}_{crit}$ –identified in the previous section as unstable– leads to a markedly different behavior. For concreteness, we concentrate on the

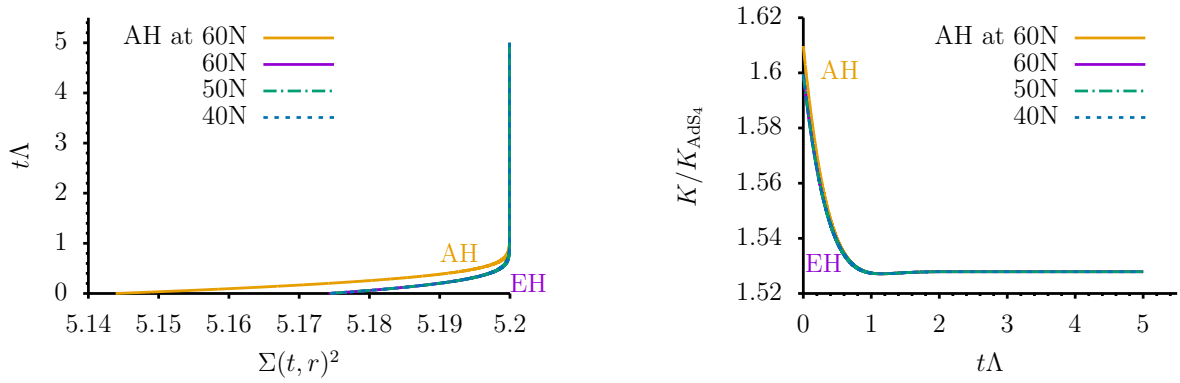

Figure 5.11: Area and Kretschmann for stable case.

particular case defined by the following configuration.

- Energy density (with $\Lambda = 1$)

$$\mathcal{E} = 0.793642\ \mathcal{E}_{crit} \qquad \Longleftrightarrow \qquad \mu = -4\Lambda^3\ .$$

- Initial conditions are chosen describing a perturbed black hole with both non-zero ϕ and χ (as detailed in Appendix C.1.3) with

$$\mathcal{A}_p = 1.0\,, \qquad \mathcal{A}_q = 0.01\,.$$

Under these conditions, the system gives rise to a rich –and very rapidly evolving dynamics– which we have confirmed through extensive convergent studies. For instance, by inspection of results obtained with different number of collocation points ($N = 20, 30, 40, 50, 60$ points), use of adaptive time-stepping to capture the increasing faster dynamics observed, and employing a different coordinate condition (setting $\lambda(t) = 0$) which does not keep the apparent horizon at a fixed location as done in [1]. All these studies confirm the observed behavior that we describe next.

As the field ϕ "rolls down" the unbounded potential, the energy gained impacts the dynamics of its normalizable coefficient (p_2) as well as the normalizable coefficient of χ which grows without bounds as shown in figure 5.12. This behavior is evidenced in the black hole, which grows fast and eventually reaches the AdS boundary in *finite asymptotic time* as illustrated in figure 5.13. The figure shows both the apparent horizon (AH), and the event horizon (EH) as well as the curvature scalar evaluated on them. Clearly, as

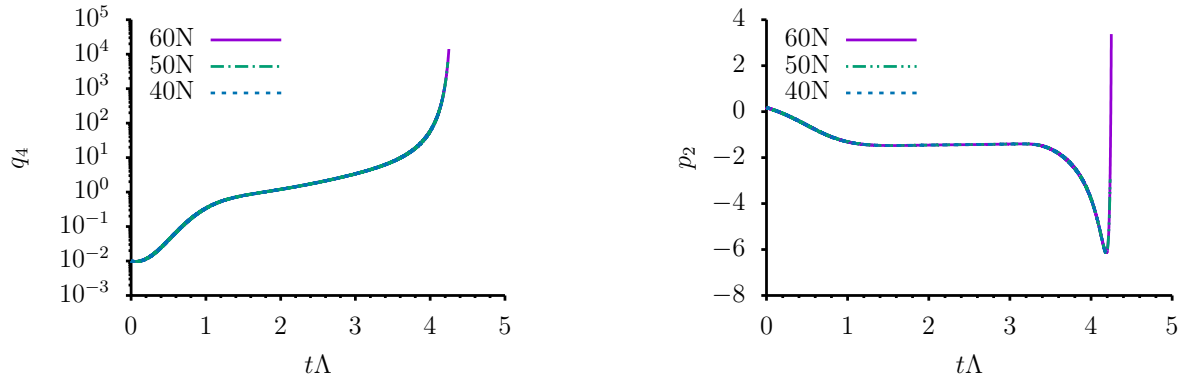

Figure 5.12: p_2 and q_4 vs. time for the unstable case.

time progresses, the AH approaches the EH and both asymptote to infinite size in a finite amount of time. This asymptotic behavior can be fit by the expression

$$\Sigma^2_{\rm EH} \propto 1/(a + bt + ct^2) \ , \tag{5.39}$$

with the following coefficients $\{a = 3.934(5),\ b = -1.811(5)$ and $c = 0.2084(5)\}$. This fit indicates a finite time divergence at $t \approx 4.30$. We find a similar asymptotic behaviour for the Kretschmann scalar evaluated at the horizon with $K \simeq \Sigma^3_{\rm EH}$, as seen in figure 5.14. Thus, at late times,

$$K_{\rm EH} \propto \Sigma^3_{\rm EH} \propto \left(\frac{1}{a + bt + ct^2}\right)^{\frac{3}{2}} \ ; \tag{5.40}$$

consequently, $K_{\rm EH}$ diverges in finite time at the boundary of AdS. Additionally, the (normalized) scalar curvatures on the AH and EH diverge with $K_{\rm EH} \leq K_{\rm AH}$. Naturally, the code is eventually unable to keep up with the radically rapid dynamics which requires ever smaller timesteps to capture the following behavior. Nevertheless, we have been able to extract convergent solutions up to a sufficiently late stage to understand the behavior and fate of the spacetime. The picture that arises is that the spacetime explores arbitrarily large curvatures in finite time, and outgoing null geodesics emanating from such regions reach the boundary of AdS in finite asymptotic time as indicated in figure 5.15. This behavior would violate the spirit of the weak cosmic censorship conjecture, in that far observers can be reached by signals emanating from arbitrarily curved spacetime regions, and is similar to that recently reported in [124].

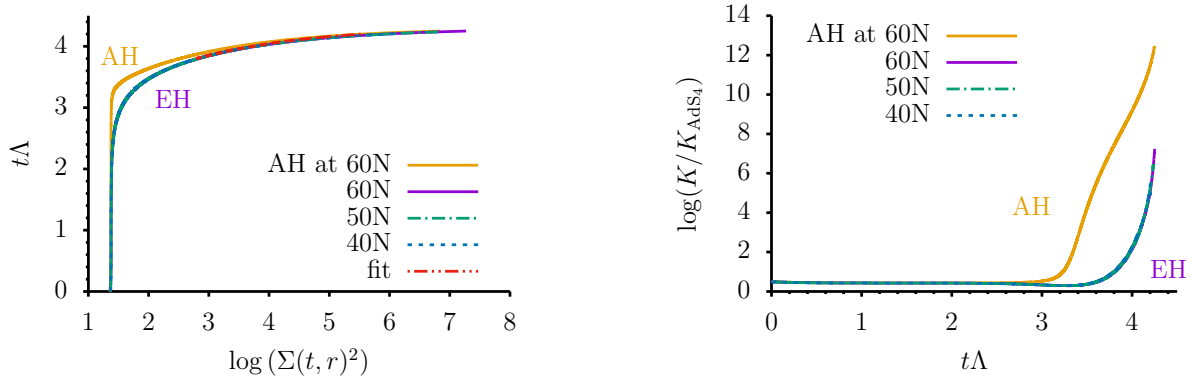

Figure 5.13: Area and Kretschmann for unstable case.

5.4 Summary

In this chapter we studied an interesting instability of the black hole horizons, observed first in [39]: below some critical energy density the horizon is unstable with respect to fluctuations spontaneously breaking a discrete symmetry. However, there is no static endpoint associated with the nonlinear build-up of the symmetry breaking condensate (scalar hair at the horizon), as opposed to typical constructions of holographic superconductors [40]. The instability is perturbative in nature (*i.e.,* describing a second order phase transition), and is triggered by an arbitrary small amplitude of the symmetry breaking mode, provided the conserved energy density of the state $\mathcal{E}$ is below a critical energy density. As a result, the onset of the instability, and dynamics close to it, can not be affected by higher-order nonlinearities in the gravitational scalar potential as long as the amplitude of unstable modes remain small. Additionally, the instability initiates in the long wavelength regime, *i.e.,* at small bulk curvature, and thus can not be removed by higher derivative corrections to the gravitational effective action.

We studied the future development of the instability, using a characteristic formulation of asymptotically anti-de Sitter gravitational dynamics [55], and argued that, at the classical level, the end point of the instability induces a curvature singularity at finite asymptotic time. Specifically, we demonstrated an apparently unbounded growth of the Kretschmann scalar in the bulk (*e.g.,* evaluated at the location of the apparent horizon). Thus, our model (5.6) provides a simple example of arbitrarily large curvatures arising in asymptotically anti-de Sitter space times at sufficiently late times.

While the analysis of this work is focused on a specific phenomenological model of gauge

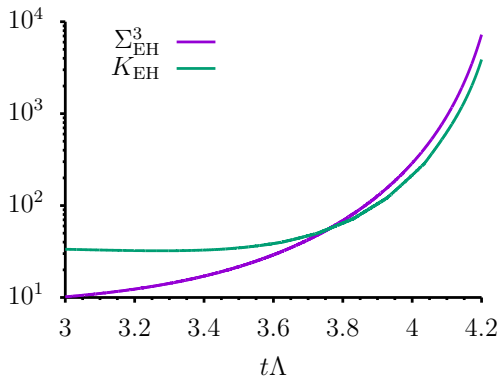

Figure 5.14: Similar asymptotic behaviour of the Kretschmann scalar and Σ^3 at the event horizon.

theory/gravity correspondence, represented by the effective gravitational action (5.6), the phenomena described, *i.e.,* horizon instability without the static end point, is realized within bona fide holographic correspondence scenarios (*e.g.,* [111, 115]). We expect that curvature singularities arise in those models as well[7]. The observation that curvature singularities might arise dynamically implies that consistent truncations of string theory and supergravity, while suitable to address static states in the theory, may fail in dynamical settings — when the evolution enters the regime of highly curved geometry; and in such cases stringy corrections will be important.

What are the holographic implications of a singularity developing evolution for the boundary gauge theory? A standard lore is that states of a closed non-integrable interacting system with large number of degrees of freedom should dynamically equilibrate. In the context of holography, early indications supported this for generic far-from-equilibrium, arbitrary low-energy states of strongly coupled conformal gauge theories, even when the dynamical evolution of these states was artificially restricted to symmetric submanifolds of the full phase space of the theory[8] [64, 125]. Shortly thereafter it was argued [126, 65, 127] that in fact symmetric phase space of holographic conformal field theories has islands of stability that never equilibrate. In this study we identified yet another possibility: initial states of holographic strongly coupled gauge theories, well described classically in the

[7]It is a straightforward exercise to examine this in a holographic model [111]; dynamics of small black hole localization in $AdS_5 \times S^5$ is much more difficult.

[8]The states in question were spatially isotropic, and invariant under all global symmetries, *i.e.,* the R-symmetry.

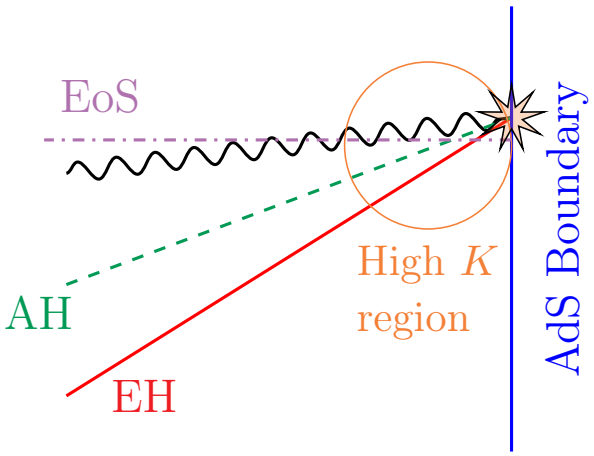

Figure 5.15: Schematic spacetime diagram. As time progresses, the apparent horizon approaches the event horizon in finite time. The scalar curvature diverges and arbitrarily high curvature regions can be identified by asymptotic observers at finite times. In the diagram, "EoS" refers to the "End of the Simulation" while the star refers to the blow up of the Kretschmann at the boundary in finite time.

gravitational frame, evolve to a singularity in finite time. Singularity is a signature for a breakdown of an approximation, and we see two possible reasons. First, it is possible the singularity is an artifact of our restriction of the state evolution to symmetric submanifolds of the full phase space of the theory and that symmetry breaking modes would allow for a smooth evolution. As we discuss below, hydrodynamic modes in the system can be gapped, leading to the same qualitative behaviour. It is more difficult to argue for the absence of light modes spontaneously breaking internal symmetries — the singularity observed might be an indication that some of these symmetries must be dynamically broken during the evolution (similar ideas were proposed in [128]). Second, the state evolution in the gravitational frame of the holography might not be always semiclassical.

We find it important to discuss another possible limitation of the study carried out here and its conclusions. We restricted the dynamics in our model to preserve boundary homogeneity and isotropy. One might argue that the physical phenomena discussed here arise as a consequence of such a restriction, and that a sufficiently generic initial state would smoothly evolve to an end point where these symmetries are spontaneously broken. We do not have a full answer to this question — gravitational simulations in the presence of spatial inhomogeneities are beyond the scope of this chapter. At the very least, in the holographic model studies in [129] there is an exotic instability discussed, without the

spatially modulated endpoint as well[9]. Since the instability and the evolution towards the singularity in our model can be triggered by arbitrarily small amplitude fluctuations of the χ-mode, *i.e.,* energetically arbitrary close to the critical point, the potentially physics-modifying hydrodynamics modes can be gapped, rendering them irrelevant to the question as to whether or not the singularity observed is physical. To demonstrate this, we modified our model with a boundary with topology $R^2 \to S^2$. All the main features described in the former case remain in the latter, in particular: there is a horizon instability, there is no static end point below some critical energy density associated with the onset of the perturbative instability, the low-energy $SO(3)$-invariant states evolve to a singular solution. It would be interesting to explore in details the role of additional massless fields at the threshold of instability, and their effect on the singularity development.

A feature of the bulk scalar potential of our holographic model (5.6) is that it is unbounded in the χ-direction (recall that the nonlinear coupling $g < 0$). We study in Appendix C.2 a modification of the model which "bounds" the χ-potential with higher order, nonlinear in χ, interactions[10]. Of course, the linearized instability is unaffected; likewise, the unstable phase with $\langle \mathcal{O}_i \rangle \neq 0$ for $\mathcal{E} > \mathcal{E}_{crit}$ is unchanged qualitatively (close to $\mathcal{E}_{crit}$ the higher-order nonlinear terms in the gravitational potential are suppressed). However, we find a new static black hole phase with $\langle \mathcal{O}_i \rangle \neq 0$, that exists both for $\mathcal{E} < \mathcal{E}_{crit}$ and $\mathcal{E} > \mathcal{E}_{crit}$ for the bounded potentials and, at least in the vicinity of perturbative instability, has higher entropy density than the symmetric phase. Unlike the exotic branch of the black holes, this new phase does not bifurcate from the onset of long-wavelength instability of the symmetric phase. For $\mathcal{E} < \mathcal{E}_{crit}$ this new static phase is always the end point of the evolution; for $\mathcal{E} > \mathcal{E}_{crit}$ the new symmetry broken phase can only be reached if the initial amplitude of the symmetry breaking fluctuations is sufficiently large — the symmetry broken phase is a potential barrier separated from the symmetric phase whenever $\mathcal{E} > \mathcal{E}_{crit}$. Our model (5.6) is a phenomenological example of the holographic correspondence, thus one might worry whether curvature diverging scenarios described here is realized in genuine (top-down) holographic dualities. We believe the answer to the question is in the affirmative:

- First, the unbounded potentials are ubiquitous in holography — a typical example is a well-studied $\mathcal{N} = 2^*$ holography [130, 131, 132], where the bulk gravitational scalars $\{\alpha, \chi\}$

[9]We would like to thank Ben Withers for bringing the reference to our attention.

[10]We would like to thank Jorge Santos for raising the issue of the unboundedness of the scalar potential in our model with its potential effect on the singular evolution that prompted this analysis.

effective action takes the form,

$$
\begin{aligned}
S^{scalar}_{\mathcal{N}=2^*} &\sim \frac{1}{16\pi G_5}\int \mathrm{d}^5x\sqrt{-g}\Big(-12(\partial\alpha)^2-4(\partial\chi)^2-V\Big)\,,\\
V(\alpha,\chi) &= -e^{-4\alpha}-2e^{2\alpha}\cosh 2\chi+\frac{1}{4}e^{8\alpha}\sinh^2 2\chi\,.
\end{aligned}
\tag{5.41}
$$

The reason why the scalar potentials in supergravity constructions can be unbounded comes from the fact that they arise from the superpotential as (for the $\mathcal{N}=2^*$ example (5.41))

$$
\begin{aligned}
V &= \frac{1}{16}\left[\frac{1}{3}\left(\frac{\partial W}{\partial\alpha}\right)^2+\left(\frac{\partial W}{\partial\chi}\right)^2\right]-\frac{1}{3}W^2\,,\\
W &= -e^{-2\alpha}-\frac{1}{2}e^{4\alpha}\cosh(2\chi)\,.
\end{aligned}
\tag{5.42}
$$

It is the $-\frac{1}{3}W^2$ contribution to V in (5.42) that is responsible for the unboundedness of V.

- Second, the scalar potential in the top-down embedding of the exotic black hole phenomena [39] constructed in [111] (see eq.(2.32) there) is unbounded from below:

$$
V(\varphi) = -2\ \big(2+\cosh(2\varphi)\big)\ . \tag{5.43}
$$

There are lots of open questions left for the future. It would be interesting to understand whether the divergent curvature scenario proposed here is universal. Is it possible to understand analytically the approach towards the singularity as in explorations of the BKL conjecture? (e.g. [133]). The link between the boundedness of the gravitational potential and the singular evolution should be studied in more detail. It is certainly important to understand the consequences of the diverging curvature for the boundary gauge theory. Is there a QFT-solvable holographic example that captures the proposed singular behavior?

Chapter 6

Final Remarks

6.1 Summary and Future Directions

In this thesis, we studied the linear and nonlinear behavior of unstable black holes in AdS spacetimes. In Chap. 2, we gave an overview of the model, the linearized equation for RN-AdS and Leaver's method to compute the QNM, as well as the characteristic formulation used for the full nonlinear problem. We discussed the numerical methods used to solve the full nonlinear set of equations Eqs. (2.6)–(2.10), and the asymptotic boundary conditions for the fields.

In Chap. 3, we used these methods to nonlinearly study the superradiant instability that results from perturbing a small RN-AdS black hole with a charged scalar perturbation. These numerical tools allowed us to study the system well into the nonlinear regime where backreaction of the field onto the spacetime is significant. Indeed, the low amplitude perturbation grows exponentially at early times, and as it grows larger it interacts nonlinearly with the black hole, extracting charge and mass. Eventually, the energy extraction reaches a saturation point, superradiance ceases, and the system settles into a stationary configuration. We connect, thus, the linear behavior of the superradiant instability, through nonlinear dynamics, to its final state which is a charged black hole with a non-trivial profile of the scalar field[1]. Decomposing the scalar field into modes and analyzing their dynamics reveals a rich and non-trivial behavior. Initially, many unstable modes can be present in the initial perturbation. All of these modes interact superradiantly with the black holes, and grow exponentially. As the superradiant bound is modified, because of

[1]The scalar field only contains the fundamental mode which saturates the superradiant bound.

the backreaction, the higher overtones cease to be unstable, falling back into the black hole and returning charge and energy. Eventually this process saturates, and the fundamental mode with a zero-growth rate is the only remaining mode. The ultimate fate of the charge superradiant instability in AdS is, thus, a stable (charged) black hole with a non-trivial scalar field configuration.

In Chap. 4, we extended the results from the previous chapter to the large RN-AdS black hole regime. Through linear and nonlinear studies we have identified the near-horizon instability, as well as the superradiant instability. With the linear analysis we provide a comprehensive picture of the mode spectrum of large RN-AdS, and show the connection between the mode spectra of the small and the large RN-AdS black holes. We show that, although different in nature, the near-horizon and the superradiant instabilities coexist in a region of the parameter space for large near-extremal RN-AdS black holes. Through the full nonlinear dynamics we elucidate the final state of the instabilities, and show they settle into stationary black holes with non-trivial scalar condensates. Additionally, we construct initial data consisting of various superradiant modes, that does not contain the fundamental mode, such that the solution cascades through a series of unstable excited hairy black hole equilibria. Indeed, we show the transition for the first overtone $n = 1$ onto the fundamental mode $n = 0$, as well as a triple cascade, $n = 2 \to n = 1 \to n = 0$. Furthermore, we use the single transition study, $n = 1 \to n = 0$, to analyze the nonlinear excitation of the modes. Indeed, the higher overtone sources the fundamental mode in a way consistent with the self-gravitating contribution of the scalar field ($A_0 \propto A_1^3$), underscoring the importance of overtone modes and nonlinear effects.

In Chap. 5, we studied two interacting massive scalar fields in the presence of a planar Schwarzschild-AdS black hole. The negative mass squared of the scalar field is chosen to be negative, but still satisfying the BF bound, whereas the other is chosen positive. A nonlinear coupling between the fields, however, introduces an effective mass for the "non-tachyonic" scalar field which is subject to a long-wavelength type of instability. Above a certain critical energy density the system displays a stable behavior settling into a hairy black hole with the tachyon field forming the scalar field condensate and the other scalar field vanishing. As we probe energy densities below the critical one, the "non-tachyonic" field displays an exponential growth at the linear level. At the nonlinear level the exponential growth of the field does not saturate leading to a runaway instability. We show the divergence, in finite asymptotic time, of the Kretschmann scalar and the areal radius of the apparent and event horizons. The instability triggered by an arbitrary small perturbation, thus, induces a curvature singularity in finite asymptotic time and does not lead to a static or stationary end state.

The instability of RN-AdS and its hairy black hole formation has been proposed as a

holographic dual to a superconducting phase transition. It would be interesting to seek a holographic interpretation of either the transient hairy black hole equilibria that we uncovered in Chap. 4, or the singularity development presented in Chap. 5.

The results presented in this thesis motivate the need for further investigation on the astrophysical, the holographic, and the classical GR fronts. In particular, in the astrophysical context, the outer potential barrier is no longer infinite as in AdS, and is usually provided by the mass term of the field. This, in fact, provides a cutoff in the mode energy and on the efficiency of the energy extraction. It would be interesting to extend the model to a more astrophysically relevant scenario like the scattering of a massive scalar field with general self-interactions off of a (rotating) Kerr black hole in asymptotically flat spacetime. Recently, in [134], the authors have proposed that if the scalar field has an axionic coupling to the EM field [2], it gives rise to a stimulated emission of photons when the number of axions is large enough, this in turn would quench the superradiant instability. It would, certainly, be interesting to explore this possibility within the full nonlinear context, however, the small growth timescale of the bosonic superradiant instability in Kerr-AF call for a very long evolution, $t_{\rm evolution} \sim 10^6 M_{\rm BH}$. On the other hand, small Kerr-AdS black holes are unstable under scalar perturbations [135, 22], and the relevant timescale seems to be much more reasonable for a full nonlinear dynamical evolution.

After studying the full nonlinear dynamics of RN-AdS the natural question that arises is whether the same would happen in asymptotically de Sitter (dS) spacetimes. It was established that RN-dS is prone to an instability in [136], however, only the monopole $l = 0$ suffers from this instability. Indeed, the real frequency of the mode is within the superradiant bound for RN-dS, which suggests that the instability is superradiant in nature. They show, as well, that for $l = 1$ and higher angular numbers the instability does not occur. Satisfying the superradiant bound, then, seems to be a *necessary* condition as opposed to a *sufficient* condition. In Chap. 4 we showed that different instabilities can coexist in the same region of parameter space, and their modes can be parametrically deformed into each other. Certainly, a similar analysis of the mode spectrum of RN-dS could help elucidate the real nature of the instability, and the full nonlinear development would determine the end-state of the instability which is still an open problem.

Lastly, the comprehensive picture given by the linear and nonlinear studies provides us with a deeper understanding of the black hole dynamics. In particular, we are investigating the nonlinear coupling between decaying quasinormal modes in (spherical) Schwarzschild-AdS. We find evidence that decaying overtone modes excite nonlinearly lower ovetone modes, with the same cubic relation we expected before. This simplified system can help

[2] A coupling of the form $\mathcal{L} \supset \frac{k_{\rm axion}}{2}\phi {}^*F^{\mu\nu}F_{\mu\nu}$, where ${}^*F^{\mu\nu} \equiv \frac{1}{2}\epsilon^{\mu\nu\rho\sigma}F_{\rho\sigma}$ is the dual of $F^{\mu\nu}$.

us shed some light into the nonlinear regime of binary black holes; specifically, to the post-merger and ringdown of the process. Recent studies have used mutliple quasinormal mode overtones to fit the ringdown part of a binary black hole gravitational wave signal. After merger, however, the system is still in the nonlinear regime, and thus our suggestion that nonlinearities might still be relevant. In our ongoing work, we show that, upon perturbation of the black hole, nonlinear mode excitation takes place between decaying quasinormal modes. These results can be used, then, to understand the post-merger nonlinear regime of binary black holes. Further work, however, is needed to have a thorough understanding of the regime of applicability of the linear results in the strongly perturbed regimes.

References

[1] Pablo Bosch, Stephen R. Green, and Luis Lehner. Nonlinear Evolution and Final Fate of Charged Anti–de Sitter Black Hole Superradiant Instability. *Phys. Rev. Lett.*, 116(14):141102, 2016.

[2] Pablo Bosch, Stephen R. Green, Luis Lehner, and Hugo Roussille. Excited hairy black holes: Dynamical construction and level transitions. *Phys. Rev. D*, 102:044014, Aug 2020.

[3] Pablo Bosch, Alex Buchel, and Luis Lehner. Unstable horizons and singularity development in holography. *JHEP*, 07:135, 2017.

[4] Nami Uchikata and Shijun Yoshida. Quasinormal modes of a massless charged scalar field on a small Reissner-Nordstrom-anti-de Sitter black hole. *Phys. Rev.*, D83:064020, 2011.

[5] Gary T. Horowitz and Veronika E. Hubeny. Quasinormal modes of AdS black holes and the approach to thermal equilibrium. *Phys. Rev.*, D62:024027, 2000.

[6] N. Uchikata and S. Yoshida. Quasinormal modes of a massless charged scalar field on a small Reissner-Nordström-anti-de Sitter black hole. *PRD*, 83(6):064020, March 2011.

[7] Vera C. Rubin and Jr. Ford, W. Kent. Rotation of the Andromeda Nebula from a Spectroscopic Survey of Emission Regions. *APJ*, 159:379, February 1970.

[8] V. C. Rubin, Jr. Ford, W. K., and N. Thonnard. Rotational properties of 21 SC galaxies with a large range of luminosities and radii, from NGC 4605 (R=4kpc) to UGC 2885 (R=122kpc). *APJ*, 238:471–487, June 1980.

[9] Gianfranco Bertone, Dan Hooper, and Joseph Silk. Particle dark matter: evidence, candidates and constraints. *Physics Reports*, 405(5-6):279390, Jan 2005.

[10] Adam G. Riess et al. Observational evidence from supernovae for an accelerating universe and a cosmological constant. *Astron. J.*, 116:1009–1038, 1998.

[11] Planck Collaboration *et. al.* Planck 2018 results. i. overview and the cosmological legacy of planck, 2018.

[12] Planck Collaboration *et. al.* Planck 2018 results. vi. cosmological parameters, 2018.

[13] Sean M. Carroll. The cosmological constant. *Living Reviews in Relativity*, 4(1), Feb 2001.

[14] Malcolm Fairbairn, Robert Hogan, and David J.E. Marsh. Unifying inflation and dark matter with the peccei-quinn field: Observable axions and observable tensors. *Physical Review D*, 91(2), Jan 2015.

[15] David J.E. Marsh, Daniel Grin, Rene Hlozek, and Pedro G. Ferreira. Tensor interpretation of bicep2 results severely constrains axion dark matter. *Physical Review Letters*, 113(1), Jul 2014.

[16] David J. E. Marsh and Ana-Roxana Pop. Axion dark matter, solitons and the cusp-core problem. *Monthly Notices of the Royal Astronomical Society*, 451(3):24792492, Jun 2015.

[17] Ya. B. Zel'dovich. Amplification of cylindrical electromagnetic waves reflected from a rotating body. *Soviet Physics-JETP*, 35:1085–1087, 1972.

[18] A. A. Starobinskij. Amplification of waves reflected from a rotating "black hole". *Zhurnal Eksperimentalnoi i Teoreticheskoi Fiziki*, 64:48–57, 1973.

[19] Asimina Arvanitaki and Sergei Dubovsky. Exploring the String Axiverse with Precision Black Hole Physics. *Phys. Rev.*, D83:044026, 2011.

[20] Asimina Arvanitaki, Masha Baryakhtar, and Xinlu Huang. Discovering the qcd axion with black holes and gravitational waves. *Physical Review D*, 91(8), Apr 2015.

[21] S.W. Hawking and H.S. Reall. Charged and rotating AdS black holes and their CFT duals. *Phys. Rev.*, D61:024014, 2000.

[22] Vitor Cardoso and Oscar J.C. Dias. Small Kerr-anti-de Sitter black holes are unstable. *Phys. Rev.*, D70:084011, 2004.

[23] Stephen R. Green, Stefan Hollands, Akihiro Ishibashi, and Robert M. Wald. Superradiant instabilities of asymptotically anti-de Sitter black holes. 2015.

[24] D. Christodoulou and R. Ruffini. Reversible transformations of a charged black hole. *Phys. Rev.*, D4:3552–3555, 1971.

[25] G. Denardo and R. Ruffini. On the energetics of Reissner Nordstrøm geometries. *Phys. Lett. B*, 45:259–262, July 1973.

[26] Jacob D. Bekenstein. Extraction of energy and charge from a black hole. *Phys. Rev. D*, 7:949–953, Feb 1973.

[27] Vitor Cardoso, Óscar J. C. Dias, Gavin S. Hartnett, Luis Lehner, and Jorge E. Santos. Holographic thermalization, quasinormal modes and superradiance in Kerr-AdS. *JHEP*, 04:183, 2014.

[28] E. Berti and K. D. Kokkotas. Quasinormal modes of Reissner-Nordstrom-anti-de Sitter black holes: Scalar, electromagnetic and gravitational perturbations. *Phys. Rev.*, D67:064020, 2003.

[29] Sean A. Hartnoll, Christopher P. Herzog, and Gary T. Horowitz. Holographic Superconductors. *JHEP*, 12:015, 2008.

[30] Steven S. Gubser. Breaking an Abelian gauge symmetry near a black hole horizon. *Phys. Rev.*, D78:065034, 2008.

[31] Keiju Murata, Shunichiro Kinoshita, and Norihiro Tanahashi. Non-equilibrium Condensation Process in a Holographic Superconductor. *JHEP*, 07:050, 2010.

[32] Jacob D. Bekenstein. Black hole hair: 25 - years after. In *2nd International Sakharov Conference on Physics*, pages 216–219, 5 1996.

[33] B. Carter. Has the black hole equilibrium problem been solved? In *8th Marcel Grossmann Meeting on Recent Developments in Theoretical and Experimental General Relativity, Gravitation and Relativistic Field Theories (MG 8)*, pages 136–155, 12 1997.

[34] Piotr T. Chrusciel, Joao Lopes Costa, and Markus Heusler. Stationary Black Holes: Uniqueness and Beyond. *Living Rev. Rel.*, 15:7, 2012.

[35] R. D. Blandford and R. L. Znajek. Electromagnetic extraction of energy from Kerr black holes. *Monthly Notices of the Royal Astronomical Society*, 179:433–456, May 1977.

[36] Roy P. Kerr. Gravitational field of a spinning mass as an example of algebraically special metrics. *Phys. Rev. Lett.*, 11:237–238, Sep 1963.

[37] Óscar J. C. Dias and Ramon Masachs. Hairy black holes and the endpoint of AdS_4 charged superradiance. *JHEP*, 02:128, 2017.

[38] Steven S. Gubser. Phase transitions near black hole horizons. *Class. Quant. Grav.*, 22:5121–5144, 2005.

[39] Alex Buchel and Chris Pagnutti. Exotic Hairy Black Holes. *Nucl. Phys. B*, 824:85–94, 2010.

[40] Sean A. Hartnoll, Christopher P. Herzog, and Gary T. Horowitz. Building a Holographic Superconductor. *Phys. Rev. Lett.*, 101:031601, 2008.

[41] Dieter R. Brill, Paul L. Chrzanowski, C. Martin Pereira, Edward D. Fackerell, and James R. Ipser. Solution of the scalar wave equation in a kerr background by separation of variables. *Phys. Rev. D*, 5:1913–1915, Apr 1972.

[42] S.A. Teukolsky. Rotating black holes - separable wave equations for gravitational and electromagnetic perturbations. *Phys. Rev. Lett.*, 29:1114–1118, 1972.

[43] Ezra Newman and Roger Penrose. An Approach to gravitational radiation by a method of spin coefficients. *J. Math. Phys.*, 3:566–578, 1962.

[44] E. W. Leaver. An analytic representation for the quasi-normal modes of kerr black holes. *Proceedings of the Royal Society A: Mathematical, Physical and Engineering Sciences*, 402(1823):285–298, December 1985.

[45] Edward W. Leaver. Spectral decomposition of the perturbation response of the schwarzschild geometry. *Phys. Rev. D*, 34:384–408, Jul 1986.

[46] E. W. Leaver. Solutions to a generalized spheroidal wave equation: Teukolskys equations in general relativity, and the twocenter problem in molecular quantum mechanics. *Journal of Mathematical Physics*, 27(5):1238–1265, 1986.

[47] Maurício Richartz and Davi Giugno. Quasinormal modes of charged fields around a reissner-nordström black hole. *Physical Review D*, 90(12), dec 2014.

[48] Emanuele Berti, Vitor Cardoso, and Andrei O. Starinets. Quasinormal modes of black holes and black branes. *Class. Quant. Grav.*, 26:163001, 2009.

[49] Masaru Shibata and Takashi Nakamura. Evolution of three-dimensional gravitational waves: Harmonic slicing case. *Phys. Rev. D*, 52:5428–5444, Nov 1995.

[50] Thomas W. Baumgarte and Stuart L. Shapiro. On the numerical integration of Einstein's field equations. *Phys. Rev. D*, 59:024007, 1999.

[51] Frans Pretorius. Numerical relativity using a generalized harmonic decomposition. *Class. Quant. Grav.*, 22:425–452, 2005.

[52] Frans Pretorius. Evolution of binary black hole spacetimes. *Phys. Rev. Lett.*, 95:121101, 2005.

[53] Frans Pretorius. Simulation of binary black hole spacetimes with a harmonic evolution scheme. *Class. Quant. Grav.*, 23:S529–S552, 2006.

[54] Jeffrey Winicour. Characteristic Evolution and Matching. *Living Rev. Rel.*, 12:3, 2009.

[55] Paul M. Chesler and Laurence G. Yaffe. Numerical solution of gravitational dynamics in asymptotically anti-de Sitter spacetimes. *JHEP*, 07:086, 2014.

[56] L. F. Abbott and Stanley Deser. Stability of Gravity with a Cosmological Constant. *Nucl. Phys.*, B195:76–96, 1982.

[57] Gioel Calabrese, Luis Lehner, Oscar Reula, Olivier Sarbach, and Manuel Tiglio. Summation by parts and dissipation for domains with excised regions. *Class. Quant. Grav.*, 21:5735–5758, 2004.

[58] Gioel Calabrese, Luis Lehner, David Neilsen, Jorge Pullin, Oscar Reula, Olivier Sarbach, and Manuel Tiglio. Novel finite differencing techniques for numerical relativity: Application to black hole excision. *Class. Quant. Grav.*, 20:L245–L252, 2003.

[59] J. D. Bekenstein. Extraction of energy and charge from a black hole. *Phys. Rev.*, D7:949–953, 1973.

[60] Pallab Basu, Jyotirmoy Bhattacharya, Sayantani Bhattacharyya, R. Loganayagam, Shiraz Minwalla, and V. Umesh. Small Hairy Black Holes in Global AdS Spacetime. *JHEP*, 10:045, 2010.

[61] Oscar J. C. Dias, Pau Figueras, Shiraz Minwalla, Prahar Mitra, Ricardo Monteiro, and Jorge E. Santos. Hairy black holes and solitons in global AdS_5. *JHEP*, 08:117, 2012.

[62] Oscar J. C. Dias, Jorge E. Santos, and Benson Way. Black holes with a single Killing vector field: black resonators. 2015.

[63] Benjamin E. Niehoff, Jorge E. Santos, and Benson Way. Towards a violation of cosmic censorship. 2015.

[64] Piotr Bizon and Andrzej Rostworowski. On weakly turbulent instability of anti-de Sitter space. *Phys. Rev. Lett.*, 107:031102, 2011.

[65] Venkat Balasubramanian, Alex Buchel, Stephen R. Green, Luis Lehner, and Steven L. Liebling. Holographic Thermalization, stability of AdS, and the Fermi-Pasta-Ulam-Tsingou paradox. *Phys. Rev. Lett.*, 113:071601, 2014.

[66] Hideki Maeda. Exact dynamical AdS black holes and wormholes with a Klein-Gordon field. *Phys. Rev.*, D86:044016, 2012.

[67] R. Brito, V. Cardoso, and P. Pani, editors. *Superradiance*, volume 906 of *Lecture Notes in Physics, Berlin Springer Verlag*, 2015.

[68] Nicolas Sanchis-Gual, Juan Carlos Degollado, Pedro J. Montero, Jos A. Font, and Carlos Herdeiro. Explosion and final state of the charged black hole bomb. 2015.

[69] A. Arvanitaki and S. Dubovsky. Exploring the string axiverse with precision black hole physics. *PRD*, 83(4):044026, February 2011.

[70] Hirotaka Yoshino and Hideo Kodama. Bosenova collapse of axion cloud around a rotating black hole. *Prog. Theor. Phys.*, 128:153–190, 2012.

[71] T. Damour, N. Deruelle, and R. Ruffini. On Quantum Resonances in Stationary Geometries. *Lett. Nuovo Cim.*, 15:257–262, 1976.

[72] Steven L. Detweiler. KLEIN-GORDON EQUATION AND ROTATING BLACK HOLES. *Phys. Rev.*, D22:2323–2326, 1980.

[73] Sayantani Bhattacharyya, Shiraz Minwalla, and Kyriakos Papadodimas. Small Hairy Black Holes in $AdS_5 x S^5$. *JHEP*, 11:035, 2011.

[74] Matthew W. Choptuik. Universality and scaling in gravitational collapse of a massless scalar field. *Phys. Rev. Lett.*, 70:9–12, 1993.

[75] Carsten Gundlach. Critical phenomena in gravitational collapse. *Living Rev. Rel.*, 2:4, 1999.

[76] Federico Carrasco, Luis Lehner, Robert C. Myers, Oscar Reula, and Ajay Singh. Turbulent flows for relativistic conformal fluids in 2+1 dimensions. *Phys. Rev.*, D86:126006, 2012.

[77] Huan Yang, Aaron Zimmerman, and Luis Lehner. Turbulent Black Holes. 2014.

[78] Allan Adams, Paul M. Chesler, and Hong Liu. Holographic turbulence. *Phys. Rev. Lett.*, 112:151602, 2014.

[79] William H. Press and Saul A. Teukolsky. Floating Orbits, Superradiant Scattering and the Black-hole Bomb. *Nature*, 238:211–212, 1972.

[80] William E. East. Superradiant instability of massive vector fields around spinning black holes in the relativistic regime. *Phys. Rev.*, D96(2):024004, 2017.

[81] Jacob D. Bekenstein. Novel "no-scalar-hair" theorem for black holes. *Phys. Rev. D*, 51:R6608–R6611, Jun 1995.

[82] Carlos A. R. Herdeiro and Eugen Radu. Asymptotically flat black holes with scalar hair: a review. *Int. J. Mod. Phys.*, D24(09):1542014, 2015.

[83] Stefan Hollands and Robert M. Wald. Stability of Black Holes and Black Branes. *Commun. Math. Phys.*, 321:629–680, 2013.

[84] R. Gregory and R. Laflamme. Black strings and p-branes are unstable. *Phys. Rev. Lett.*, 70:2837–2840, 1993.

[85] Luis Lehner and Frans Pretorius. Black Strings, Low Viscosity Fluids, and Violation of Cosmic Censorship. *Phys. Rev. Lett.*, 105:101102, 2010.

[86] James M. Bardeen and Gary T. Horowitz. The Extreme Kerr throat geometry: A Vacuum analog of $AdS_2 \times S^2$. *Phys. Rev.*, D60:104030, 1999.

[87] Peter Breitenlohner and Daniel Z. Freedman. Positive Energy in anti-De Sitter Backgrounds and Gauged Extended Supergravity. *Phys. Lett.*, 115B:197–201, 1982.

[88] E. Abdalla, C. E. Pellicer, Jeferson de Oliveira, and A. B. Pavan. Phase transitions and regions of stability in reissner-nordström holographic superconductors. *Phys. Rev. D*, 82:124033, Dec 2010.

[89] Kengo Maeda, Shunsuke Fujii, and Jun-ichirou Koga. Final fate of instability of reissner-nordström-anti-de sitter black holes by charged complex scalar fields. *Phys. Rev. D*, 81:124020, Jun 2010.

[90] Stefan Hollands and Akihiro Ishibashi. Instabilities of extremal rotating black holes in higher dimensions. *Commun. Math. Phys.*, 339(3):949–1002, 2015.

[91] Peter Zimmerman. Horizon instability of extremal Reissner-Nordström black holes to charged perturbations. *Phys. Rev.*, D95(12):124032, 2017.

[92] Stefanos Aretakis. Horizon Instability of Extremal Black Holes. *Adv. Theor. Math. Phys.*, 19:507–530, 2015.

[93] Oscar J. C. Dias, Pau Figueras, Ricardo Monteiro, Harvey S. Reall, and Jorge E. Santos. An instability of higher-dimensional rotating black holes. *JHEP*, 05:076, 2010.

[94] Huan Yang, Fan Zhang, Aaron Zimmerman, David A. Nichols, Emanuele Berti, and Yanbei Chen. Branching of quasinormal modes for nearly extremal Kerr black holes. *Phys. Rev.*, D87(4):041502, 2013.

[95] Aaron Zimmerman and Zachary Mark. Damped and zero-damped quasinormal modes of charged, nearly extremal black holes. *Phys. Rev.*, D93(4):044033, 2016. [Erratum: Phys. Rev.D93,no.8,089905(2016)].

[96] Nils Siemonsen and William E. East. Gravitational wave signatures of ultralight vector bosons from black hole superradiance. 2019.

[97] Asimina Arvanitaki, Masha Baryakhtar, and Xinlu Huang. Discovering the QCD Axion with Black Holes and Gravitational Waves. *Phys. Rev.*, D91(8):084011, 2015.

[98] Paul M. Chesler and David A. Lowe. Nonlinear Evolution of the AdS_4 Superradiant Instability. *Phys. Rev. Lett.*, 122(18):181101, 2019.

[99] Gary T. Horowitz, Jorge E. Santos, and Benson Way. A Holographic Josephson Junction. *Phys. Rev. Lett.*, 106:221601, 2011.

[100] Vishal Baibhav, Emanuele Berti, Vitor Cardoso, and Gaurav Khanna. Black Hole Spectroscopy: Systematic Errors and Ringdown Energy Estimates. *Phys. Rev.*, D97(4):044048, 2018.

[101] Matthew Giesler, Maximiliano Isi, Mark Scheel, and Saul Teukolsky. Black hole ringdown: the importance of overtones. 2019.

[102] Maximiliano Isi, Matthew Giesler, Will M. Farr, Mark A. Scheel, and Saul A. Teukolsky. Testing the no-hair theorem with GW150914. *Phys. Rev. Lett.*, 123(11):111102, 2019.

[103] Iara Ota and Cecilia Chirenti. Overtones or higher harmonics? Prospects for testing the no-hair theorem with gravitational wave detections. 2019.

[104] Yosef Zlochower, Roberto Gomez, Sascha Husa, Luis Lehner, and Jeffrey Winicour. Mode coupling in the nonlinear response of black holes. *Phys. Rev.*, D68:084014, 2003.

[105] William E. East, Fethi M. Ramazanolu, and Frans Pretorius. Black Hole Superradiance in Dynamical Spacetime. *Phys. Rev.*, D89(6):061503, 2014.

[106] Huan Yang, Fan Zhang, Stephen R. Green, and Luis Lehner. Coupled Oscillator Model for Nonlinear Gravitational Perturbations. *Phys. Rev.*, D91(8):084007, 2015.

[107] Juan Martin Maldacena. The Large N limit of superconformal field theories and supergravity. *Int. J. Theor. Phys.*, 38:1113–1133, 1999. [Adv. Theor. Math. Phys.2,231(1998)].

[108] Ofer Aharony, Steven S. Gubser, Juan Martin Maldacena, Hirosi Ooguri, and Yaron Oz. Large N field theories, string theory and gravity. *Phys. Rept.*, 323:183–386, 2000.

[109] Igor R. Klebanov and Edward Witten. AdS / CFT correspondence and symmetry breaking. *Nucl. Phys. B*, 556:89–114, 1999.

[110] Sean A. Hartnoll. Lectures on holographic methods for condensed matter physics. *Class. Quant. Grav.*, 26:224002, 2009.

[111] Aristomenis Donos and Jerome P. Gauntlett. Superfluid black branes in AdS_4 $\times S^7$. *JHEP*, 06:053, 2011.

[112] Veronika E. Hubeny and Mukund Rangamani. Unstable horizons. *JHEP*, 05:027, 2002.

[113] Alex Buchel and Luis Lehner. Small black holes in $AdS_5 \times S^5$. *Class. Quant. Grav.*, 32(14):145003, 2015.

[114] Alex Buchel. Universality of small black hole instability in AdS/CFT. *Int. J. Mod. Phys. D*, 26(13):1750140, 2017.

[115] scar J.C. Dias, Jorge E. Santos, and Benson Way. Lumpy AdS_5 S^5 black holes and black belts. *JHEP*, 04:060, 2015.

[116] Alex Buchel and Chris Pagnutti. Correlated stability conjecture revisited. *Phys. Lett. B*, 697:168–172, 2011.

[117] Steven S. Gubser and Indrajit Mitra. Instability of charged black holes in Anti-de Sitter space. 2000.

[118] Steven S. Gubser and Indrajit Mitra. The Evolution of unstable black holes in anti-de Sitter space. *JHEP*, 08:018, 2001.

[119] H. Bondi, M. G. J. van der Burg, and A. W. K. Metzner. Gravitational Waves in General Relativity. VII. Waves from Axi-Symmetric Isolated Systems. *Proceedings of the Royal Society of London Series A*, 269(1336):21–52, August 1962.

[120] Nigel T. Bishop, Roberto Gomez, Luis Lehner, Manoj Maharaj, and Jeffrey Winicour. High powered gravitational news. *Phys. Rev. D*, 56:6298–6309, 1997.

[121] Ivan Booth. Black hole boundaries. *Can. J. Phys.*, 83:1073–1099, 2005.

[122] Pau Figueras, Veronika E. Hubeny, Mukund Rangamani, and Simon F. Ross. Dynamical black holes and expanding plasmas. *JHEP*, 04:137, 2009.

[123] Alex Buchel. Chiral symmetry breaking in cascading gauge theory plasma. *Nucl. Phys. B*, 847:297–324, 2011.

[124] Toby Crisford and Jorge E. Santos. Violating the Weak Cosmic Censorship Conjecture in Four-Dimensional Anti–de Sitter Space. *Phys. Rev. Lett.*, 118(18):181101, 2017.

[125] Alex Buchel, Luis Lehner, and Steven L. Liebling. Scalar Collapse in AdS. *Phys. Rev. D*, 86:123011, 2012.

[126] Alex Buchel, Steven L. Liebling, and Luis Lehner. Boson stars in AdS spacetime. *Phys. Rev. D*, 87(12):123006, 2013.

[127] Stephen R. Green, Antoine Maillard, Luis Lehner, and Steven L. Liebling. Islands of stability and recurrence times in AdS. *Phys. Rev.*, D92(8):084001, 2015.

[128] scar J.C. Dias, Jorge E. Santos, and Benson Way. Localised $AdS_5 \times S^5$ Black Holes. *Phys. Rev. Lett.*, 117(15):151101, 2016.

[129] Benjamin Withers. Black branes dual to striped phases. *Class. Quant. Grav.*, 30:155025, 2013.

[130] Krzysztof Pilch and Nicholas P. Warner. N=2 supersymmetric RG flows and the IIB dilaton. *Nucl. Phys. B*, 594:209–228, 2001.

[131] Alex Buchel, Amanda W. Peet, and Joseph Polchinski. Gauge dual and noncommutative extension of an N=2 supergravity solution. *Phys. Rev. D*, 63:044009, 2001.

[132] Alex Buchel, Jorge G. Russo, and Konstantin Zarembo. Rigorous Test of Non-conformal Holography: Wilson Loops in N=2* Theory. *JHEP*, 03:062, 2013.

[133] David Garfinkle. Numerical simulations of generic singuarities. *Phys. Rev. Lett.*, 93:161101, 2004.

[134] Taishi Ikeda, Richard Brito, and Vitor Cardoso. Blasts of light from axions. *Physical Review Letters*, 122(8), Feb 2019.

[135] Nami Uchikata, Shijun Yoshida, and Toshifumi Futamase. Scalar perturbations of kerr-ads black holes. *Physical review. D, Particles, fields, gravitation, and cosmology*, 80(8), 2009.

[136] Zhiying Zhu, Shao-Jun Zhang, C.E. Pellicer, Bin Wang, and Elcio Abdalla. Stability of reissner-nordstrm black hole in de sitter background under charged scalar perturbation. *Physical Review D*, 90(4), Aug 2014.

[137] Alex Buchel, Robert C. Myers, and Anton van Niekerk. Nonlocal probes of thermalization in holographic quenches with spectral methods. *JHEP*, 02:017, 2015. [Erratum: JHEP 07, 137 (2015)].

APPENDICES

Appendix A

Quasi-Normal Frequencies from Linear Theory

A.1 Background quantities in terms of the horizon radii

In this section we show the explicit expressions for the metric function Eq. (2.12), the mass Eq. (2.14), and the charge Eq. (2.16), in terms of the inner and outer horizon radii r_- and r_+. This is useful, in particular, for the implementation of Leaver's method to compute the QNM frequencies. The metric function becomes

$$f(r) = \frac{(r-r_-)(r-r_+)}{L^2 r^2}\left[r^2 + r(r_- + r_+) + \left(L^2 + r_-^2 + r_+^2 + r_- r_+\right)\right], \tag{A.1}$$

from which we can read off the mass and the charge of the black hole,

$$M = \frac{(r_- + r_+)}{2L^2}\left(L^2 + r_-^2 + r_+^2\right), \tag{A.2}$$

$$Q^2 = \frac{r_-\, r_+}{L^2}\left(L^2 + r_-^2 + r_+^2 + r_-\, r_+\right). \tag{A.3}$$

Thus, at extramality, the inner and outer horizons coincide $r_+ = r_-$, and

$$M_{\rm ext} = r_+ + \frac{2r_+^3}{L^2}, \tag{A.4}$$

$$Q^2_{\rm ext} = r_+^2\left(1 + \frac{3r_+^2}{L^2}\right). \tag{A.5}$$

A.2 QNM frequency comparison

We use the full nonlinear code in the "linear regime", that is with small amplitudes of the scalar field, and evolve the scalar perturbation. We use a time domain analysis to fit for the fundamental mode, and obtain the real and imaginary frequencies. We compare these values with linear studies performed in [4], where the QNM are obtained for a charged scalar perturbation in an RN-AdS background.

q	e	$\frac{Q_{\rm AD}}{Q_{\rm Ext}}$	$M_{\rm AD}$	$Q_{\rm AD}$	Re(ω)	Im(ω)	RE to Re(ω)$_{[4]}$	RE to Im(ω)$_{[4]}$
0	0	0.4	0.12192	−0.16932808	2.3909	−0.44312	0.003 %	0.007%
		0.6	0.14432	−0.25399212	2.2888	−0.53427	0.005%	0.012 %
		0.8	0.17568	−0.33865616	2.1922	−0.69804	0.009 %	0.012 %
1	2	0.4	0.12192	−0.16932808	2.6707	−0.27173	0.0002%	0.011%
		0.6	0.14432	−0.25399212	2.7050	−0.24032	0.001%	0.029%
		0.8	0.17568	−0.33865616	2.6809	−0.23659	0 %	0.03 %
2	4	0.4	0.12192	−0.16932808	2.9647	−0.14131	0.003%	0.015%
		0.6	0.14432	−0.25399212	3.1708	−0.058363	0.004 %	0.089%
		0.8	0.17568	−0.33865616	3.3620	0.0015557	0.011 %	0.007 %

Table A.1: Recovering the quasi-normal frequencies obtain through linear theory by Uchikata & Yoshida [4].

Appendix B

Continued Fraction convergence and accuracy

B.1 Code validation

We have confirmed the validity of both codes used extensively in this work through self-convergence tests as well as comparison with available results in suitable regimes. With regards to self-convergence tests, we have verified that as the number of terms employed in the continued fraction method is increased, our results asymptote to consistent results and, that typically this takes place when $N \gtrapprox 3000$ (see figure B.1). Convergence of the non-linear code has been recently demonstrated in [1]. As mentioned, we also compare with specific results; in particular: our QNM frequencies obtained in our linear analysis agree with those obtained in [5] in the Schwarzschild-AdS limit ($Q = 0$,$q = 0$) to better than 1.2% for the real part of ω and better than 0.5% for the imaginary part of ω. In the charged, small black hole case, our results agree with those presented in [4] to better than 0.1%. An example of these comparisons is given in Tables B.1,B.2. In the large black hole, small charge regime, our results agree with those in [28]. to better than 7.5% and 4% for the real and imaginary parts of ω respectively. We have also confirmed solutions obtained with our full non-linear simulations illustrate initial growth rates –in the unstable regime– and black hole QNMs consistent with the expected results from our linear studies.

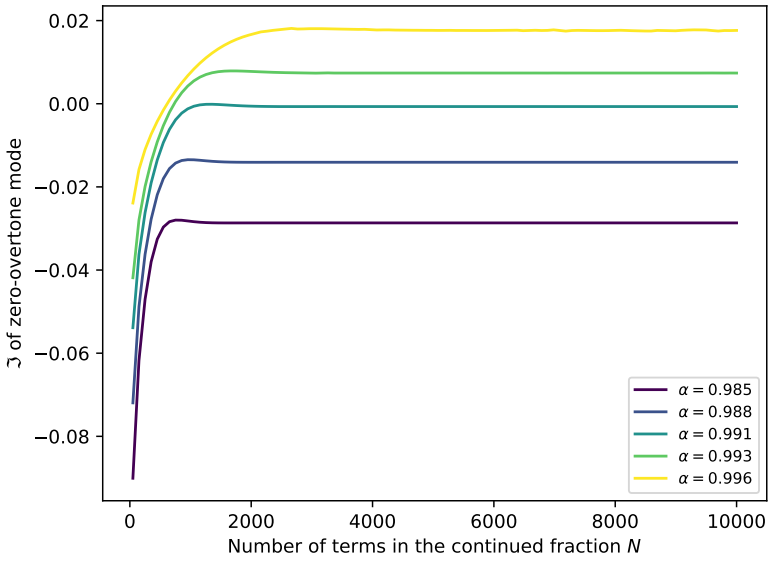

Figure B.1: Imaginary part of the NH mode as a function of the number of terms used in the continued fraction N, for different values of the extremality parameter a. We can observe that convergence is more difficult when a gets closer to 1, as the equations used break down.

	Values of [5]		Our values	
r_+	$\mathrm{Re}(\omega)$	$\mathrm{Im}(\omega)$	$\mathrm{Re}(\omega)$	$\mathrm{Im}(\omega)$
0.4	2.3629	−1.0064	2.3629	−1.0065
0.6	2.4316	−1.5797	2.4316	−1.5797
0.8	2.5878	−2.1304	2.5878	−2.1304
1	2.7982	−2.6712	2.7982	−2.6712
5	9.4711	−13.3255	9.4711	−13.3255
10	18.6070	−26.6418	18.6070	−26.6418
50	92.4937	−133.1933	92.4937	−133.1933
100	184.9534	−266.3856	184.9534	−266.3856

Table B.1: QNMs found by the linear analysis for a Schwarzschild black hole ($a = 0$, $q = 0$) and comparison with the results of [5] (Table 1). We can see our values agree completely with the previous results.

		Values of [4]		Our values	
q	a	$\mathrm{Re}(\omega)$	$\mathrm{Im}(\omega)$	$\mathrm{Re}(\omega)$	$\mathrm{Im}(\omega)$
0	0	2.6928	-1.0095×10^{-1}	2.6928	-1.0096×10^{-1}
	0.2	2.6801	-1.0434×10^{-1}	2.6801	-1.0434×10^{-1}
	0.4	2.6410	-1.1625×10^{-1}	2.6411	-1.1626×10^{-1}
	0.6	2.5723	-1.4417×10^{-1}	2.5723	-1.4417×10^{-1}
	0.8	2.4787	-2.0756×10^{-1}	2.4788	-2.0757×10^{-1}
	0.9	2.4332	-2.5493×10^{-1}	2.4332	-2.5493×10^{-1}
2	0.2	2.7614	-8.1233×10^{-2}	2.7615	-8.1233×10^{-2}
	0.4	2.8058	-6.7765×10^{-2}	2.8059	-6.7765×10^{-2}
	0.6	2.8256	-5.8950×10^{-2}	2.8257	-5.8950×10^{-2}
	0.8	2.8161	-5.6894×10^{-2}	2.8161	-5.6894×10^{-2}
	0.9	2.7977	-6.3772×10^{-2}	2.7978	-6.3773×10^{-2}
4	0.2	2.8414	-6.1698×10^{-2}	2.8415	-6.1698×10^{-2}
	0.4	2.9650	-3.4408×10^{-2}	2.9650	-3.4408×10^{-2}
	0.6	3.0672	-1.3945×10^{-2}	3.0672	-1.3946×10^{-2}
	0.8	3.1515	1.7314×10^{-3}	3.1515	1.7314×10^{-3}
	0.9	3.1878	6.5742×10^{-3}	3.1879	6.5744×10^{-3}

Table B.2: QNMs found by the linear analysis for a small black hole ($r_+ = 0.1$) and comparison with the results of [4] (Table 2). We can see our values agree completely with the previous results.

Appendix C

Appendix for Chapter 5

C.1 Numerical setup

We adapt the characteristic formulation of [55] for the numerical solution of (5.16)-(5.18).

C.1.1 Field redefinitions and the code equations

We introduce a new radial coordinate

$$x \equiv \frac{1}{r} \in [0,1]\,, \qquad d_+ = \partial_t + A(t,r)\;\partial_r \;\to\; \partial_t - x^2 A(t,x)\;\partial_x\,, \tag{C.1}$$

maintaining $' \equiv \partial_x$ and $\dot{} \equiv \partial_t$, and redefine the fields

$$\{\,\phi\,,\,\chi\,,\,\Sigma\,,\,A\,,\,d_+\phi\,,\,d_+\chi\,,\,d_+\Sigma\,\} \;\to\; \{\,p\,,\,q\,,\,\sigma\,,\,a\,,\,dp\,,\,dq\,,\,d\sigma\,\} \tag{C.2}$$

as follows

$$
\begin{aligned}
&\phi(t,x) = x\ p_1 + x\ p(t,x)\ ,\\
&\chi(t,x) = x^3\ q(t,x)\ ,\\
&\Sigma(t,x) = \frac{1}{x} + \sigma(t,x)\ ,\\
&A = a(t,x) + \frac{1}{2}\ \Sigma(t,x)^2\ ,\\
&d_+\phi(t,x) = -\frac{p_1}{2} + x\ dp(t,x)\ ,\\
&d_+\chi(t,x) = x^3\ dq(t,x)\ ,\\
&d_+\Sigma(t,x) = x\ d\sigma(t,x) + \frac{1}{2}\ \Sigma(t,x)^2 - \frac{p_1}{12}\ d_+\phi(t,x) + \frac{p_1^2}{48}\ .
\end{aligned}
\tag{C.3}
$$

Using (5.19), we find the asymptotic boundary expansion $x \to 0_+$ for the new fields:

$$
\begin{aligned}
&p = p_2(t)\ x + \mathcal{O}(x^2)\,, \qquad q = q_4(t)\ x + \mathcal{O}(x^2)\ ,\\
&dp = -p_2(t) - p_1\lambda(t) + \mathcal{O}(x)\,, \qquad dq = -2q_4(t) + \mathcal{O}(x)\ ,\\
&\sigma = \lambda(t) - \frac{p_1^2}{8}\ x + \mathcal{O}(x^2)\,, \qquad d\sigma = \mu + \mathcal{O}(x)\ ,\\
&a = -\dot{\lambda}(t) + \left(\mu - \frac{p_1^2}{12}\ \lambda(t) - \frac{p_1}{12}\ p_2(t)\right)\ x + \mathcal{O}(x^2)\ .
\end{aligned}
\tag{C.4}
$$

In new variables (C.3), the equations of motion used to evolve the system take form:

$$
\begin{aligned}
&\left[\partial_{xx}^2 + \frac{2}{x}\ \partial_x + \frac{x^4}{4}(3q + xq')^2 + \frac{1}{4}(p_1 + p + xp')^2\right]\sigma = J_\sigma\ ,\\
&J_\sigma\{p,p',q,q'\} = -\frac{x^3}{4}\ (3q + xq')^2 - \frac{p'}{4}(xp' + 2p + 2p_1) - \frac{1}{4x}(p + p_1)^2\ ,
\end{aligned}
\tag{C.5}
$$

$$\left[\partial_x + \frac{12\sigma + 12x\sigma' - xp_1(p_1+p+xp')}{12(1+x\sigma)}\right]\ dp + \left[\frac{x(p_1+p+xp')}{1+x\sigma}\right]\ d\sigma = J_2\ ,$$

$$\left[\partial_x + \frac{12\sigma + 12x\sigma' + xp_1(p_1+p+xp')}{12(1+x\sigma)}\right]\ d\sigma + \left[-\frac{xp_1^2(p_1+p+xp')}{144(1+x\sigma)}\right]\ dp = J_3\ ,$$

$$J_2\{p,p',q,\sigma,\sigma'\} = \frac{1}{1+x\sigma}\bigg(-\frac{1}{16}p'(p_1^2+8\sigma^2)x - \frac{1}{16}(p_1^2+8\sigma^2)(p+p_1) + \frac{1}{2}p_1\sigma'$$
$$- p'\sigma - \frac{p'}{2x} + \frac{p}{2x^2}\bigg) - (p+p_1)q^2gx^4\ ,$$

$$J_3\{p,p',q,\sigma,\sigma'\} = \frac{1}{1+x\sigma}\bigg(-\frac{p'p_1}{192}(p_1^2+8\sigma^2)x - \frac{p+p_1}{192}(48p\sigma^2+p_1^3+56p_1\sigma^2) - \frac{\sigma'}{48}(p_1^2$$
$$+ 72\sigma^2) - \frac{p_1p'\sigma}{12} + \frac{1}{x}\left(-\frac{\sigma}{2}(p+p_1)^2 - 3\sigma\sigma' - \frac{p'p_1}{24}\right) + \frac{1}{x^2}\bigg(-\frac{p^2}{4} - \frac{11}{24}pp_1 - \frac{3}{16}p_1^2$$
$$- \frac{3}{2}\sigma'\bigg)\bigg) + \frac{g}{4}\sigma(p+p_1)^2q^2x^5 + \frac{g}{12}(p+p_1)(3p+2p_1)q^2x^4 + \frac{1}{2}\sigma q^2x^3 + \frac{1}{2}q^2x^2\ , \tag{C.6}$$

$$\left[\partial_x + \frac{2+3x\sigma+x^2\sigma'}{x(1+x\sigma)}\right]dq + \left[-\frac{x^2p_1q' + 3xp_1q}{12(1+x\sigma)}\right]dp + \left[\frac{x^2q'+3xq}{1+x\sigma}\right]d\sigma = J_4\ ,$$

$$J_4\{p,q,q',\sigma\} = \frac{1}{1+x\sigma}\bigg(-\left(q\sigma g(p+p_1)^2 + \frac{1}{2}\sigma^2q' + \frac{1}{16}p_1^2q'\right)x - \frac{q}{16}\bigg(16g(p+p_1)^2 \tag{C.7}$$
$$+ 3p_1^2 + 24\sigma^2\bigg) - \sigma q' + \frac{1}{x}\left(-5\sigma q - \frac{1}{2}q'\right) - \frac{7q}{2x^2}\bigg)\ ,$$

$$\left[\partial^2_{xx}+\frac{2}{x}\,\partial_x\right]a+\left[\frac{1}{(1+xs)^2}\left(-\frac{1}{2}p'\sigma^2x^2+\left(-\frac{1}{2}\sigma^2(p+p_1)-p'\sigma-\frac{1}{6}p_1\sigma'\right)x\right.\right.$$
$$\left.\left.-\sigma(p+p_1)-\frac{p'}{2}-\frac{3p+2p_1}{6x}\right)\right]dp+\left[\frac{2(x^2\sigma'-1)}{x(1+xs)^2}\right]d\sigma+\left[-\frac{x^3(xq'+3q)}{2}\right]dq=J_5\ ,$$
$$J_5\{p,p',q,q',\sigma,\sigma'\}=\frac{1}{(1+xs)^2}\left(\frac{\sigma^4}{4}(p')^2x^4+\frac{\sigma^3}{2}p'(p\sigma+p_1\sigma+2p')x^3+\left(\frac{1}{4}\sigma^4(p+p_1)^2\right.\right.$$
$$+2p'\sigma^3(p+p_1)+\frac{3}{2}(p')^2\sigma^2-(\sigma')^2\sigma^2\Big)x^2+\left(\sigma^3(p+p_1)^2+\frac{1}{4}p'\sigma^2(12p+11p_1)+(p')^2\sigma\right.$$
$$\left.-2(\sigma')^2\sigma\right)x+\frac{1}{4}\sigma^2(p+p_1)(6p+5p_1)+\frac{\sigma}{2}p'(4p+3p_1)+\frac{1}{8}\sigma'(-p_1^2+8\sigma^2)+\frac{1}{4}(p')^2$$
$$-(\sigma')^2+\frac{1}{x}\left(\frac{\sigma}{2}(p+p_1)(2p+p_1)+\frac{1}{4}p'(2p+p_1)+2\sigma\sigma'\right)$$
$$\left.+\frac{1}{x^2}\left(\frac{p^2}{4}+\frac{pp_1}{4}+\frac{p_1^2}{8}+\sigma'\right)\right)+\frac{1}{4}x^2(q'x+3q)^2(\sigma x+1)^2\ , \tag{C.8}$$

$$\dot{p}=dp+\frac{1}{2}p'(\sigma^2+2a)x^2+\left(\frac{1}{2}(p+p_1)(\sigma^2+2a)+p'\sigma\right)x+(p+p_1)\sigma+\frac{p'}{2}+\frac{p}{2x}\ ,$$
$$\dot{q}=dq+\frac{1}{2}q'(\sigma^2+2a)x^2+\left(\frac{3}{2}(\sigma^2+2a)q+\sigma q'\right)x+3\sigma q+\frac{q'}{2}+\frac{3q}{2x}\ . \tag{C.9}$$

Numerical code is organized as follows.

- **[Step 1]:** assume that at a time step t we have profiles

$$\{p(t,x)\,,\,q(t,x)\,,\,p'(t,x)\,,\,q'(t,x)\}\qquad\text{and}\qquad\lambda(t)\ . \tag{C.10}$$

- **[Step 2]:** we solve linear in σ equation (C.5), subject to boundary conditions

$$\sigma(t,x=0)=\lambda(t)\,,\qquad\sigma'(t,x=0)=-\frac{p_1^2}{8}\ . \tag{C.11}$$

- **[Step 3]:** we solve linear in $\{dp,d\sigma\}$ system (C.6), subject to the boundary conditions

$$dp(t,x=0)=-p'(t,x=0)-\lambda(t)\ p_1\,,\qquad d\sigma(t,x=0)=\mu\ . \tag{C.12}$$

- **[Step 4]:** we solve linear in dq equation (C.7), subject to the boundary conditions

$$dq(t,x=0)=-2q'(t,x=0)\ . \tag{C.13}$$

- **[Step 5]:** we solve linear in a equation (C.8), subject to the boundary conditions

$$a'(t, x = 0) = \mu - \frac{p_1^2}{12}\,\lambda(t) - \frac{p_1}{12}\,p'(t, x = 0)\,, \qquad a(t, x = 1) = a^h\,. \tag{C.14}$$

  The value a^h is determined from the stationarity of the apparent horizon at $x = 1$ as explained in the following subsection.

- **[Step 6]:** we use evolution equations (C.9), along with (see (C.4))

$$\dot{\lambda}(t) = -a(t, x = 0)\,, \tag{C.15}$$

  to compute

$$\{p(t + dt, x)\,,\, q(t + dt, x)\,,\, \lambda(t + dt)\,. \tag{C.16}$$

  After computing the radial coordinate derivatives $\{p'(t + dt, x)\,,\, q'(t + dt, x)\}$, we repeat **[Step 1]**.

Notice that the first equation in (5.16) is redundant in our numerical procedure: rather than propagating in time Σ, we compute it from the constraint (5.17) at each time step; nonetheless, we monitor the consistency of that equation during the evolution.

Implementing the code[1], we use spectral methods for the radial coordinate integration, **[Step 2]**- **[Step 5]**. Singularities of the equations at the boundary collocation point $x = 0$ are resolved using the corresponding boundary conditions instead. We use fourth-order Runge-Kutta method for the time evolution, **[Step 6]**.

C.1.2 Apparent horizon and the boundary condition for a

Our numerical implementation requires an independent computation of $a^h \equiv a(t, x = 1)$ (see (C.14)), given radial profiles $\{p, p', q, q', s, s', dp, ds, dq\}$ and the diffeomorphisms parameter λ at time t. Following [55], this is done by enforcing the time-independent location of the horizon. Apparent horizon is located as $x = x_h$ such that

$$d_+\Sigma(t, x)\Big|_{x=x_h} = 0\,. \tag{C.17}$$

Assuming $x_h = 1$, $\frac{dx_h}{dt} = 0$, and using equations of motion (C.5)-(C.9) we compute a^h from

$$\partial_t d_+\Sigma(t, x_h)\Big|_{x_h=1} = 0\,. \tag{C.18}$$

[1] Code implementation is similar to the one used in [137].

Denoting

$$\left\{\, p^h\,,\, dp^h\,,\, q^h\,,\, dq^h\,,\, \sigma^h\,\right\} \equiv \left\{\, p\,,\, dp\,,\, q\,,\, dq\,,\, \sigma\,\right\}\Big|_{(t,x=1)} \tag{C.19}$$

we find

$$\begin{aligned} a^h =& \frac{1}{4}\Bigg(\Big(g\left(q^h\right)^2-1\Big)\left(p_1+p^h\right)^2+2\left(q^h\right)^2-6\Bigg)^{-1}\Bigg(\left(2dp^h-p_1\right)^2+4\left(dq^h\right)^2 \\ &+2\Big(\left(p^h+p_1\right)^2-2\left(q^h\right)^2+6\Big)\left(\sigma^h+1\right)^2-2\left(q^h\right)^2\left(\sigma^h+1\right)^2\left(p_1+p^h\right)^2 g\Bigg)\,. \end{aligned} \tag{C.20}$$

C.1.3 Initial conditions

To evolve (C.5)-(C.9) one has to provide data, at $t=0$ as required by **[Step 1]**, see (C.10). In particular, we need to specify $\lambda_0 \equiv \lambda(t=0)$. Once again, we follow [55].

Recall that both ϕ and χ are left invariant under the reparametrization transformations:

$$\frac{1}{x} \;\to \frac{1}{x}+\lambda_0\,. \tag{C.21}$$

To maintain this invariance we specify initial conditions for $\{p,q\}$ (in λ_0-invariant way) in terms of two amplitudes $\{\mathcal{A}_p,\mathcal{A}_q\}$:

$$\begin{aligned} p\Big|_{t=0} &= \mathcal{A}_p\,\frac{x}{(1+x\lambda_0)^2}\;\exp\left[-\frac{x}{1+x\lambda_0}\right]-\frac{p_1\lambda_0 x}{1+x\lambda_0}\,, \\ q\Big|_{t=0} &= \mathcal{A}_q\,\frac{x}{(1+x\lambda_0)^4}\;\exp\left[-\frac{x}{1+x\lambda_0}\right]\,. \end{aligned} \tag{C.22}$$

We then proceed as follows[2]:

- given $\{\mathcal{A}_p,\mathcal{A}_q\}$ we set $\lambda_0=0$ and perform **[Step 2]** (C.11) and **[Step 3]** (C.12);
- having enough data, we follow (C.3) to compute the profile $d_+\Sigma(t=0,x)$;
- we find numerically the root $x=x_0$ of the equation

$$d_+\Sigma(t=0,x)\Big|_{x=x_0}=0\,; \tag{C.23}$$

[2]For this procedure the integration range over the radial coordinate x might exceed unity.

- we set the trial value of λ_0 as
$$\lambda_0 = \frac{1}{x_0} - 1 \,, \tag{C.24}$$
which (apart from the numerical errors) would guarantee that the corresponding location of the apparent horizon is now at $x = 1$;

- the trial value (C.24) is further adjusted repeatedly performing **[Step 2]** and **[Step 3]** to achieve
$$d_+\Sigma(t=0,x)\Big|_{x=1} = 0 \tag{C.25}$$
at a high accuracy.

C.1.4 Convergence tests

We performed self-convergence tests to verify the validity of the obtained numerical solutions. In particular, we study each configuration numerically under different number of collocation points $N = 20, 30, 40, 50, 60, 80$. We monitored the convergence of the residuals of the constraint equations to zero as well as each evolved field (and computing self-convergence test by a suitable interpolation onto a finite difference grid). Additionally, we confirmed convergence of the location of the event horizon and the Kretschmann scalar at both the apparent and event horizons. As an illustration, figure C.1 displays $K_{\rm AH}$ for both the stable and unstable configurations. For the former case, all resolutions show an excellent agreement. In contrast, the unstable case illustrates a convergence to a divergent behavior which requires increasingly finer resolutions to be captured. Such more finely resolved studies provide enough information to understand the late time behaviour, in particular, up to a time $t \simeq 4.2\Lambda$.

C.1.5 Event Horizon Finder

To find the event horizon we trace null geodesics at late times back in time and determine the surface $R(t)$ where they converge. To do so, we start from
$$g_{ab} n^a n^b = 0 \,, \tag{C.26}$$
where n^a denotes the null tangent vector to the geodesics. Using (5.15) and the field redefinition (C.1) and (C.2) this relation implies
$$\frac{\mathrm{d}x}{\mathrm{d}t} = -x^2 \left(a(t,x) + \frac{1}{2}\sigma(t,x)^2 \right) - x\sigma(t,x) - \frac{1}{2} \,, \tag{C.27}$$

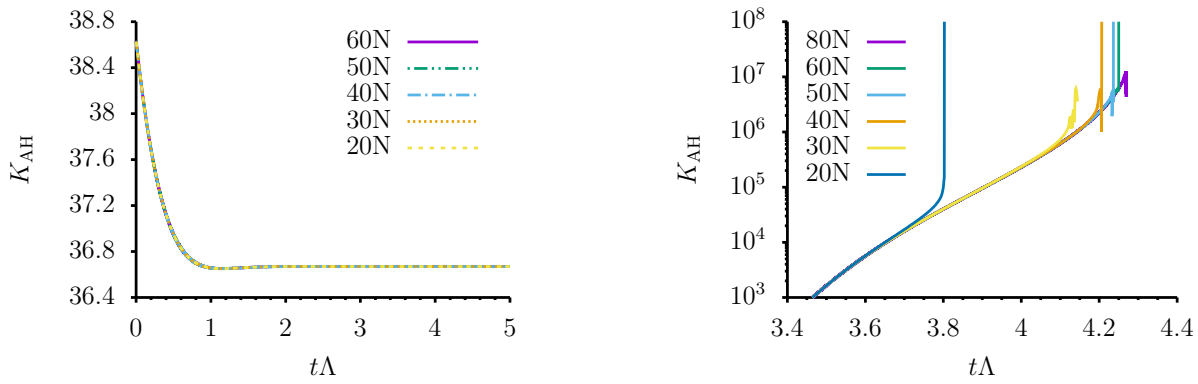

Figure C.1: Kretschmann scalar at apparent horizon. Left panel stable case. Right panel unstable case.

which we solve numerically using either a RK4 integrator or an second order implicit integrator. The results obtained with both methods converge and are in excellent agreement. As described briefly above, we consider a collection of starting points at different radii and bisect the resulting behavior to home-in on $R(t)$. Figure C.2 displays eight representative initial conditions and illustrate the convergent behavior towards the event horizon.

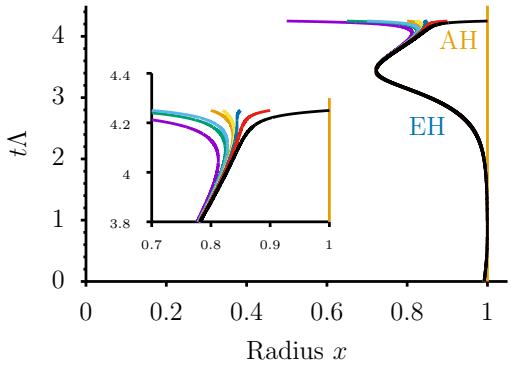

Figure C.2: Illustration of representative null rays traced to find the event horizon. The inset shows a zoom-in at late times which aids to visualize how null rays starting at different locations converge as they are traced backwards in time.

C.2 Bounded scalar potentials in exotic holographic model

In this section we explore modification of the model (5.6) where the potential for the gravitational scalar χ is bounded; specifically we modify the nonlinear interactions between ϕ and χ as follows

$$-g\phi^2\chi^2 \qquad \rightarrow \qquad -g\phi^2\chi^2\left(1-f\ \chi^2\right)\ , \tag{C.28}$$

where $f = \text{const} > 0$ is a new parameter. It is straightforward to modify the numerical code to reflect the change (C.28). We performed various tests and verified convergence of the new numerical code. In what follows we report the results of the analysis.

Because modification (C.28) is a higher-order χ-nonlinear interaction, the linearized stability analyses are not affected — there is a linearized instability for $\mathcal{E} < \mathcal{E}_{crit}$ with $\mathcal{E}_{crit}$ given by (5.10). Likewise, the static exotic branch bifurcating from the symmetric phase at the onset of the instability is qualitatively unchanged, see figure 5.3. However, for a wide range of $f > 0$ we found a new phase of the model with $\langle \mathcal{O}_i \rangle \neq 0$. This new phase exists for $\mathcal{E} \lesseqgtr \mathcal{E}_{crit}$, though it is numerically challenging to find it as f decreases and $\mathcal{E} \to \mathcal{E}_{crit}$. The new branch enters a full phase diagram of the model in a fairly complicated fashion. For the results in figure C.3 we choose $f = 55$. The left panel shows the entropy density difference between the symmetric phase s_{sym} and a new symmetry broken phase s_{broken}. The (red) dashed vertical line identifies the onset of the linearized instability at $\mathcal{E} = \mathcal{E}_{crit}$.

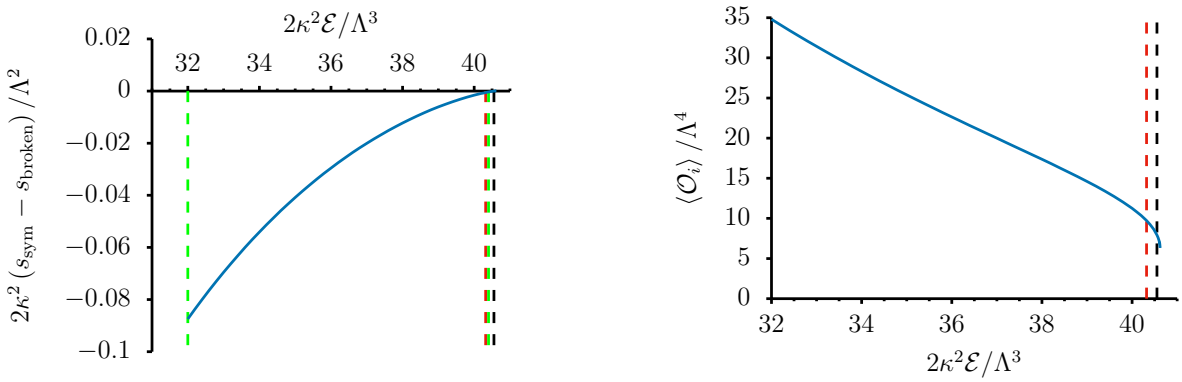

Figure C.3: There is a new symmetry broken phase of the model (5.6) for the modified nonlinear interaction (C.28); here, $f = 55$. The left panel shows the difference in the entropy densities between symmetric and broken phases as a function of energy density. The (red) vertical dashed line is the onset of the linearized instability of the symmetric phase at $\mathcal{E} = \mathcal{E}_{crit}$, see (5.10). The (black) vertical dashed line denotes a new first-order phase transition at $\mathcal{E} = \mathcal{E}_{black}$, see (C.29). The vertical (green) dashed lines indicate energy densities used in numerical evolutions, $\mathcal{E}_{green,left} < \mathcal{E}_{crit} < \mathcal{E}_{green,right} < \mathcal{E}_{black}$. The right panel represents the order parameter of the broken phase as a function of the energy density.

This new phase dominates the microcanonical ensemble all the way to $\mathcal{E}_{black}$, denoted by the (black) vertical dashed line,

$$s_{broken}(\mathcal{E}) > s_{sym}(\mathcal{E})\,, \qquad \text{for} \qquad \mathcal{E} < \mathcal{E}_{black} = 1.0057(3)\ \mathcal{E}_{crit}\ . \tag{C.29}$$

At $\mathcal{E} = \mathcal{E}_{black}$ there is a first-order phase transition, and since the symmetric phase at this energy density is perturbatively stable, the transition would occur dynamically only if the amplitude of the symmetry breaking fluctuations is large enough — we explore this below for the energy density represented by the right (green) vertical dashed line

$$\mathcal{E}_{crit} \quad < \quad \mathcal{E}_{green,right} = 1.0019(7)\ \mathcal{E}_{crit} \quad < \quad \mathcal{E}_{black}\ . \tag{C.30}$$

The left (green) vertical dashed line corresponds to the energy density (5.32), $\mathcal{E}_{green,left} < \mathcal{E}_{crit}$. The right panel in figure C.3 shows the order parameter, $\langle\mathcal{O}_i\rangle$, for the new symmetry breaking phase as a function of the energy density $\mathcal{E}$.

As figure C.4 shows, the new symmetry broken phase dominates the microcanonical ensemble at $\mathcal{E} = \mathcal{E}_{crit}$ for all values of the f in (C.28) we studied. Notice that as f decreases

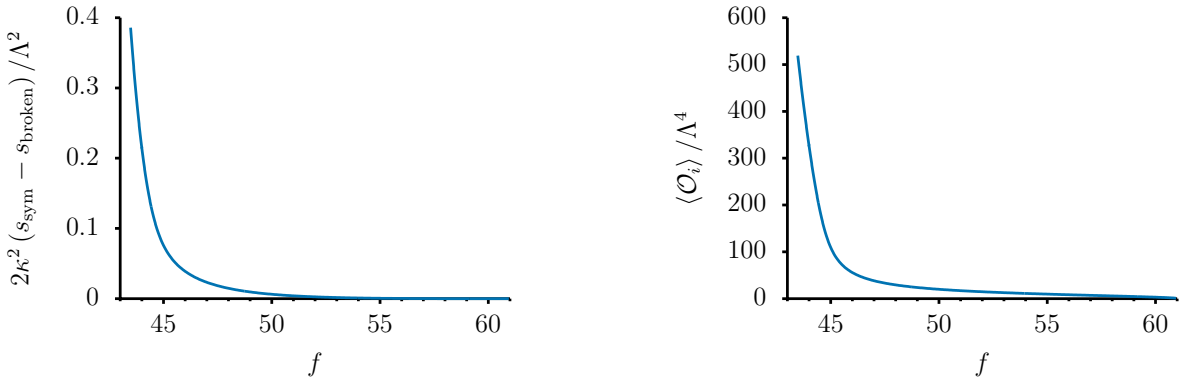

Figure C.4: New symmetry broken phase dominates the microcanonical ensemble at $\mathcal{E} = \mathcal{E}_{crit}$ for a wide range of the nonlinear parameter f, "bounding" the scalar potential in (C.28). Right panel shows the corresponding dependence of the order parameter $\langle \mathcal{O}_i \rangle$ in the broken phase.

the new phase becomes very different from the symmetric phase: it is much strongly favored entropically, and the symmetry breaking order parameter $\langle \mathcal{O}_i \rangle$ (right panel) exhibits a rapid growth. All this is suggests that the limit $f \to 0_+$ is a singular one, as expected from the main text analysis of the $f = 0$ model (5.6).

Figure C.5 represents the time evolution of model with $f = 55$, $\mathcal{E} = \mathcal{E}_{green,left} = 0.793642\ \mathcal{E}_{crit}$, and the initial conditions chosen following Appendix C.1.3 with values of $\mathcal{A}_p$ and $\mathcal{A}_q$ as in the simulations reported in section 5.3.4. The symmetry preserving $\langle \mathcal{O}_r \rangle$ (left panel) and the symmetry breaking $\langle \mathcal{O}_i \rangle$ (right panel) condensates equilibrate to static values [(red) dashed lines] corresponding to the new symmetry broken phase discussed here. This should be contrasted with the $f = 0$ results reported in section 5.3.4, where the system evolves to a naked singularity. We initiate evolution with small amplitude of the symmetry breaking fluctuation

$$\langle \mathcal{O}_i \rangle \Big|_{t=0} = 0.0252\ \Lambda^4\ ; \tag{C.31}$$

hence, they do not have enough time to become nonlinear at $t\Lambda \sim 1$, and the symmetric condensate $\langle \mathcal{O}_r \rangle$ is close to its value in symmetry preserving phase at the corresponding energy density (represented by (green) dashed line). For $t\Lambda > 1$ the symmetry breaking fluctuations continue to grow, ultimately capping off at the new equilibrium value.

As shown in figure C.3, the new symmetry broken phase has an interesting feature in

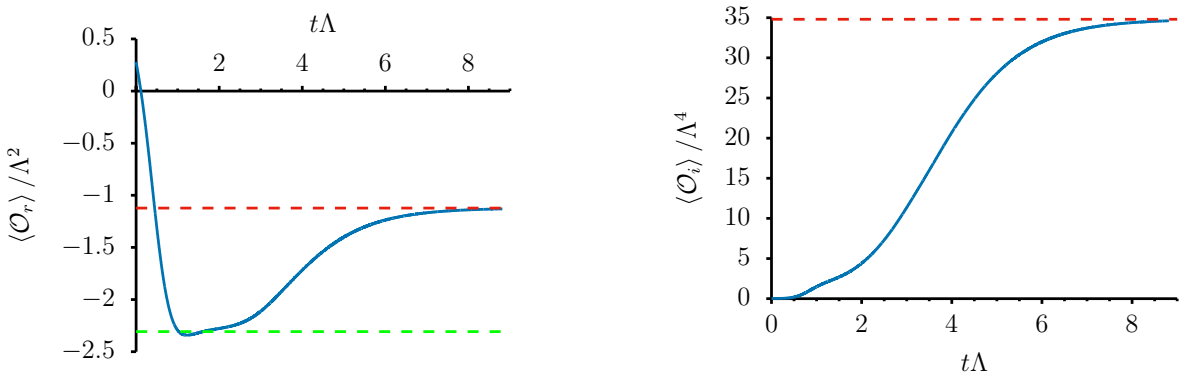

Figure C.5: Time evolution of the symmetric preserving order parameter $\langle \mathcal{O}_r \rangle$ (left panel) and the symmetry breaking order parameter $\langle \mathcal{O}_i \rangle$ (right panel) for $\mathcal{E} < \mathcal{E}_{crit}$, see (5.32), and $f = 55$. The system equilibrates to appropriate static values of the condensates, represented by (red) dashed lines. The (green) dashed line is the expectation value of $\mathcal{O}_r$ in the symmetric phase at the corresponding energy density.

the narrow energy range:

$$\mathcal{E}_{\text{crit}} < \mathcal{E} < \mathcal{E}_{\text{black}} \, . \tag{C.32}$$

Here, the symmetric phase is perturbatively stable, but the new symmetry broken phase is nonetheless entropically favorable; thus one expects that the broken phase can be reached dynamically only if the amplitude of the initial symmetry breaking fluctuations is sufficiently large. We find that this is indeed the case. For the results presented in figure C.6, $\langle \mathcal{O}_i \rangle \Big|_{t=0} = 0.0252 \ \Lambda^4$ and the system equilibrates to a (metastable) symmetric phase. Figure C.7 represents results of the simulation for the initial condition with $\langle \mathcal{O}_i \rangle \Big|_{t=0} = 2.52 \ \Lambda^4$ — here the amplitude is large enough to reach the entropically dominant symmetry broken phase. The approach to equilibrium in both cases is very slow as the energy density of the simulations is close to the critical one, see (C.30).

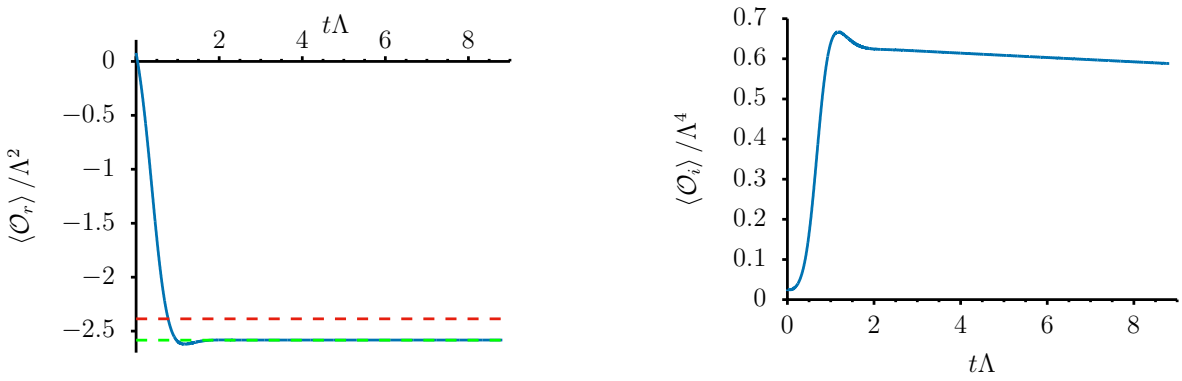

Figure C.6: Dynamics of the model with $f = 55$ and $\mathcal{E} = \mathcal{E}_{green,right}$, see (C.30) with initially small amplitude of the symmetry breaking fluctuations (right panel). Symmetry preserving condensate $\langle \mathcal{O}_r \rangle$ equilibrates to the value in the symmetric phase [(green) dashed line]. The (red) dashed line is the value of this condensate at the same energy in the symmetry broken phase.

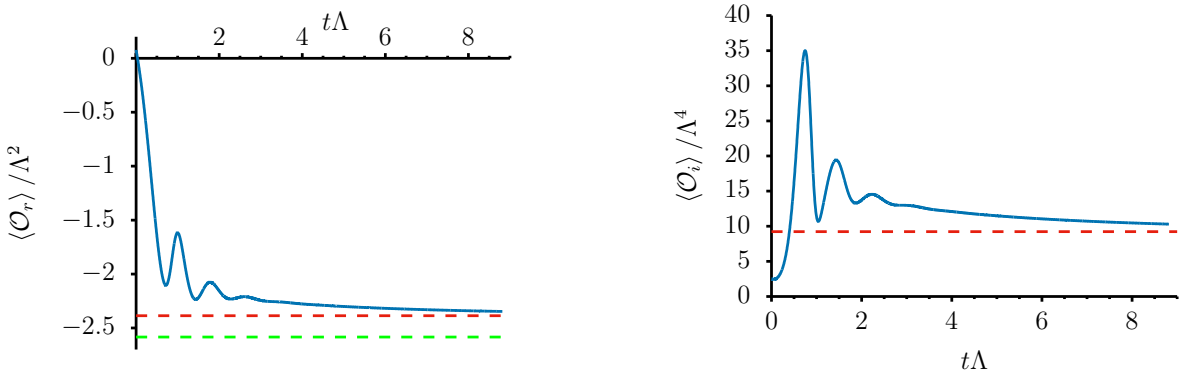

Figure C.7: Dynamics of the model with $f = 55$ and $\mathcal{E} = \mathcal{E}_{green,right}$, see (C.30) with initially large amplitude of the symmetry breaking fluctuations (right panel). Symmetry preserving condensate $\langle \mathcal{O}_r \rangle$ approaches the equilibrium value in the symmetry broken phase [(red) dashed line]. The (green) dashed line is the value of this condensate at the same energy in the symmetric phase.